SLAC-R-1014

Measurement of Time-Dependent CP Asymmetry in the Decay of a Neutral B Meson to a J/Psi and a Long-Lived Neutral Kaon at BaBar

By Emilie Claire Mutsumi Martin

SLAC National Accelerator Laboratory, Stanford University, Stanford CA 94309

Work funded in part by DOE Contract DE-AC02-76SF00515

UNIVERSITY OF CALIFORNIA,
IRVINE

Measurement of Time-Dependent CP Asymmetry in the Decay of a Neutral B Meson to a J/Psi and a Long-lived Neutral Kaon at BABAR.

DISSERTATION

submitted in partial satisfaction of the requirements
for the degree of

DOCTOR OF PHILOSOPHY

in Physics

by

Emilie Claire Mutsumi Martin

Dissertation Committee:
Professor David Kirkby, Chair
Professor Arvind Rajaraman
Professor Jonas Schultz

2009

The dissertation of Emilie Claire Mutsumi Martin
is approved and is acceptable in quality and form for
publication on microfilm and in digital formats:

Committee Chair

University of California, Irvine
2009

DEDICATION

To my father who gave me the Physics bug many years ago on the trails surrounding Grenoble and to my mother who made sure we never got lost.

TABLE OF CONTENTS

LIST OF FIGURES

LIST OF TABLES

ACKNOWLEDGMENTS

The work presented here would not have been possible without the help and support of many friends and colleagues.

I would like to thank my advisor David Kirkby and the UCI group for all their support, advice and encouragment. David is a great teacher and he introduced me to High Energy Physics during a class I took while studying abroad from France at UCI. He continued to provide me with great opportunities as I became a graduate student. The other members of the UCI group have been a tremendous help throughout my years of graduate school as well. Jonas Schultz is a terrific teacher, who is always there to lend a helping hand. Mario Bondioli and Mark Mandelkern always provided great insight and support. They have all given me countless pieces of advice at the group meetings over the years, including the other members of the group: Ivo Eschrich, Andy Lankford, Will Roethel and Dave Stocker.

Many thanks to my defense committee, David Kirkby, Arvind Rajaraman and Jonas Schultz for helping me improve my dissertation.

I had a great time working with Ray Cowan on the various *BABAR* web tools. Being completely new to web development, I was able to learn so much. He has such great patience and his passion for learning is very contagious.

Riccardo Faccini also had a great influence by proposing that I join the $\sin 2\beta$ task force. He first presented me with the opportunity of the DOE-INFN exchange, through which I spent two months in Rome, where he acted as my advisor. I would like to thank the INFN Roma staff and students for welcoming me, especially Sonia and Mauro. I had a lot of fun discovering Rome with Mahsa and we had a great time sharing the office with Paul Jackson.

Working on $\sin 2\beta$ has been a wonderful experience, thanks to the people I got to meet and work with in the process. In 2006: Chunhui Chen, Giuseppe Finocchiaro, Katherine George, Elisa Manoni and Cecilia Voena. What a productive year for the analysis and on a personal level for all of us (weddings and babies!), but we made it! For the second round, in 2008: Adrian Bevan, Chunhui Chen (another brave one who decided to sign up again) and Chih-hsiang Cheng. What a fantastic crew to be working with!

Of course, where would I be today if it was not for the help of my fellow graduate students Shane Curry and Parker Lund. It has been a lot of fun to share an office with you at SLAC, as well as *off-site* with Jo. You can still tolerate me even after calling you in the middle of the night for help on how to handle some problems with SVTRAD. That is true friendship! Brian Petersen was also a big help during the SVTRAD days. More generally, I would like to thank the members of the Stanford group, who became our office mates later on: Pat Burchat, Matt Bellis and Tomo

Miyashita.

I have made many friends along the way at UCI or SLAC in particular, who I have not mentioned here, but I hope they will recognize themselves.

Je remercie tous mes amis en France et ailleurs. Merci d'avoir toujours été là malgré la distance.

Un grand merci à toute ma famille et en particulier à mes parents, Jeanne et Jean-Seb. Vous m'avez soutenue depuis le début et vous avez toujours cru en moi, même quand je n'y croyais plus.

Brian, thank you for sticking with me in this long journey. I know it was not easy everyday, but you made it so much more enjoyable. I am so grateful for the infinite support - to the moon and back - and for not making fun of my poor coding practices. Your family has also always been supportive and I am so happy we are all one big family now.

CURRICULUM VITAE

Emilie Claire Mutsumi Martin

EDUCATION

Doctor of Philosophy in Physics **2009**
University of California, Irvine *Irvine, California*

Master of Science in Physics **2005**
University of California, Irvine *Irvine, California*

Diplôme d'Etudes Approfondies(Master of Science in Physics) **2003**
Université Joseph Fourier *Grenoble, France*

Maîtrise de Physique (Bachelor of Science in Physics) **2002**
Université Joseph Fourier *Grenoble, France*
Education Abroad Program with the University of California, Irvine

RESEARCH EXPERIENCE

Graduate Research Assistant **2005–2008**
University of California, Irvine *Irvine, California*

DoE/INFN Exchange Program **Sep.2006– Nov.2006**
Università di Roma La Sapienza and INFN *Rome, Italy*

Intern *Quark-antiquark correlation and hadrons form factors* **Mar.–Jul. 2003**
Laboratory for Subatomic Physics and Cosmology (LPSC) *Grenoble, France*

Intern *E.P.R. Paradox and Quantum Probabilities* **Jul.–Aug. 2001**
Joseph Fourier Institute *Grenoble, France*

Intern *Cryogenics and magnetization measurements* **Jun. 2001**
High Magnetic Field Laboratory (LCMI), C.N.R.S. *Grenoble, France*

SELECTED PUBLICATIONS

Update of Time-Dependent CP Asymmetry Measurements in $b \to c\bar{c}s$ Decays, B. Aubert et al. [BABAR Collaboration], arXiv:0808.1903[hep-ex].
Contributed to the 34^{th} International Conference on High-Energy Physics, ICHEP 08.

Improved Measurement of CP Violation in Neutral B Decays to $c\bar{c}s$, B. Aubert et al. [BABAR Collaboration], Phys. Rev. Lett. 99, 171803 (2007).

Measurement of the $B^0 \to \bar{\Lambda} p \pi$ Branching Fraction and Study of the Decay Dynamics, B. Aubert et al. [BABAR Collaboration], arXiv:hep-ex/0608020v1. Contributed to the 33^{rd} International Conference on High-Energy Physics, ICHEP 06

TALKS

Measurement of $\sin(2\beta)$ **in Charmonium** **Sep. 2008**
CKM 2008 5^{th} Workshop on the Unitarity Triangle *Rome, Italy*

Aspects of the $\sin 2\beta$ **measurement specific to the decay mode** $B^0 \to J/\psi K_L^0$ **Apr. 2007**
2007 American Physical Society April Meeting *Jacksonville, Florida*

ABSTRACT OF THE DISSERTATION

Measurement of Time-Dependent CP Asymmetry in the Decay of a Neutral B Meson to a J/Psi and a Long-lived Neutral Kaon at *BABAR*.

By

Emilie Claire Mutsumi Martin

Doctor of Philosophy in Physics

University of California, Irvine, 2009

Professor David Kirkby, Chair

The *BABAR* experiment at the SLAC National Accelerator Laboratory provides an excellent environment to study CP violation in B decays. A measurement of time-dependent CP-violating asymmetry in neutral B decays to charmonium states, in particular $B^0, \overline{B}^0 \rightarrow J/\psi K_L^0$, is presented here. $J/\psi K_L^0$ is the most compelling CP-even final state used to measure the Unitarity Triangle parameter sin2β at *BABAR*. The measurements reported here use a data sample of (465 ± 5) million $\Upsilon(4S) \rightarrow B\overline{B}$ decays collected with the *BABAR* detector at the PEP-II asymmetric energy e^+e^- storage operating at the SLAC National Accelerator Laboratory. The time-dependent CP asymmetry parameters measured for the $B^0 \rightarrow J/\psi K_L^0$ decay are: $C = -0.033 \pm 0.050(\text{stat}) \pm 0.027(\text{syst})$ and $S = -0.694 \pm 0.061(\text{stat}) \pm 0.031(\text{syst})$. These results are in good agreement with the Standard Model predictions.

Introduction

Our current understanding of the interactions between the elementary constituents of matter is described in the so-called *Standard Model* (SM) of elementary particles. The SM is a very well-established theory and has successfully predicted the outcomes of a large number of experiments. Some parameters remain unconstrained or are not derived from fundamental considerations and hint to the existence of *physics beyond the SM*. CP symmetry violation (CPV) has been thought to be a good place to look for such new effects not described in the model and is the subject of this thesis.

CP symmetry is the product of two symmetries : C for charge conjugation, which changes a particle to its antiparticle, and P for parity, which transforms a physical system into its mirror image. The first experimental evidence for CPV was discovered in 1964 by Christenson, Cronin, Fitch and Turlay [1] in an experiment involving neutral kaons. This observation had many important consequences and CPV has been playing a central role in particle physics ever since. In 1967, Sakharov showed that CPV is needed to explain the matter-antimatter asymmetry of the Universe [2]. In 1973, Kobayashi and Maskawa [3] proposed a generalization of the quark mixing matrix, introduced by Cabibbo [4], assuming a model with three families of quarks and leptons to explain CPV in quark decays. The quarks of the third family, called the b for bottom (or beauty) and t for top were discovered in 1977 [5] and 1994 [6], respectively. More recently, the description of CPV in quark decays given by Kobayashi and Maskawa was confirmed by precision experiments at *BABAR* and Belle and they were awarded the 2008 Nobel Prize in Physics.

Putting empirical constraints on the so-called *CKM matrix* (for Cabibbo, Kobayashi and Maskawa) is the primary goal of the *BABAR* scientific program. *BABAR* was designed to study the decays of B mesons, which is a good place to measure the parameters of the CKM matrix since CPV is expected to be two orders of magnitude greater in the B meson sector than in the kaon sector.

The main focus of this thesis is the study of CPV in the decay $B^0 \to J/\psi K^0_L$ [1]. This decay mode is part of a more general analysis that looks for CPV in decays involving a $b \to c\bar{c}s$ transition, which are the so-called *golden modes* for the measurement of CPV at B factories. Besides $B^0 \to J/\psi K^0_L$, the analysis includes decays of B^0 to $J/\psi K^0_S$, $\psi(2S)K^0_S$, $\chi_{c1}K^0_S$, $\eta_c K^0_S$, and $J/\psi K^{*0}$. $B^0 \to J/\psi K^0_L$ is the only CP even-mode in this set of decay modes which makes it the most experimentally accessible CP even mode at *BABAR*. The measurement of the parameter sin2β, which can be extracted with these modes without any theoretical uncertainty, was the object of the first *BABAR* publication [7], which used the first year of data taking. The Belle experiment - *BABAR*'s direct competitor located in Japan - published their result simultaneously [7]. A few months later, both experiments were able to establish CPV in the neutral B meson system [9].

In this thesis, I will present the results of this analysis obtained using the final *BABAR* dataset, emphasizing the measurement of the CPV parameters using the $B^0 \to J/\psi K^0_L$ decay mode. To do so, I will first give an overview of the theory behind CPV in the SM. Then I will describe the *BABAR* detector and what makes it an optimal tool in the search for CPV. Special attention will be given to some of the subsystems that are the most important in our analysis. The Silicon Vertex

[1] Charge conjugation is implied throughout this document.

Tracker and its radiation protection system in particular, will be emphasized since I was "SVTRAD" commissioner from July 2007 to the end of the running period of Babar in April 2008. This was part of the service work that I participated in when moving to SLAC in August 2005. I have also been responsible for the development and maintenance of some of the *BABAR* web tools used to facilitate the organization and review of the important number of analyses performed at *BABAR*. The analysis procedure will be discussed in details in the third chapter and the final results will be presented and interpreted in the fourth chapter. A fifth chapter presents results of the measurement of the branching fraction of $B^0 \to \bar{\Lambda} p \pi^-$ based on data accumulated from 1999 to 2004.

It is important to point out that the *BABAR* experiment is an international collaboration of more than 550 physicists and engineers, and the work presented here has received contributions from many of them. All the results presented here have been reviewed by the *BABAR* community and been presented at international conferences [11]. The results of the time-dependent CP asymmetry measurement have been the object of a publication in Physical Review Letters (PRL) [10] for the data recorded up to August 2006 and have been submitted to Physics Review D (PRD) [12] for the complete dataset. The results related to the measurement of the branching fraction of the decay $B^0 \to \bar{\Lambda} p \pi^-$, presented in Chapter 5 have been presented at the 33^{rd} International Conference on High Energy Physics in 2006 [61] and updated results on the full *BABAR* data sample will soon be submitted to PRD.

Chapter 1

CP Violation in the B Meson System

In this chapter we review CP symmetry and how the Standard Model (SM) can explain its breaking in certain rare processes. We will pay particular attention to the B meson sector.

CP symmetry breaking is accounted for in the SM and explained by the Kobayashi-Maskawa mechanism. The source of CP violation (CPV) is a single phase in the mixing matrix, called the Cabibbo-Kobayashi-Maskawa (CKM) matrix, which describes the charged currents in the weak interaction between quarks. CPV was discovered in the neutral kaon system in 1964 [1]. In 1980 and 1981, Bigi, Carter and Sanda observed that studying the properties of B mesons would be a good way to test the Kobayashi-Maskawa mechanism for CPV [13]. The focus of this thesis is to test the Standard Model predictions for CPV in the B meson system. This is one of the major tasks that has motivated the construction of the BABAR detector and the B factory. So far, all measurements of CP violation are consistent with the SM, however it is possible for New Physics to emerge in case a discrepancy with the predictions is found. For this reason, it is important to measure the CP parameters with very high accuracy. In this chapter, our goal is to show why the B meson system is a promising place to look for CPV. To do so, we begin our discussion by introducing some key concepts, explain what CPV is and how it is described in the SM. In particular, we review in detail the CKM matrix. We can then turn our attention to the B meson system and study its sensitivity to CPV.

1.1 The Standard Model

The Standard Model (SM) of particle physics is a theory of elementary particles and their interactions. So far it has been very successful and its predictive power has continued to increase over the past decades as more precise measurements of its parameters are performed.

The particles of the SM can be characterized by a number of quantum numbers, which describe their properties, such as their electric charge, their spin, their weak isospin and their mass. According to Noether's theorem, the conservation of these quantum numbers is the consequence of fundamental symmetries of Nature. The particles of the SM can be organized into three groups depending on their spin. Particles of spin 1/2 are called fermions. The properties of the leptons and of the quarks are shown in Table 1.1. These particles are the fundamental constituents of matter and are organized in three *generations* of increasing masses.

Particles of spin 1 are gauge bosons and are force mediators for the electromagnetic, weak and strong interactions. They are displayed in Table 1.2. Finally a particle of spin 0, the Higgs boson is predicted by the SM and is required to explain the masses of

Fundamental fermions (spin 1/2)					
Leptons			Quarks		
Particle	Charge (e)	Mass (MeV/c^2)	Particle	Charge (e)	Mass (MeV/c^2)
ν_e	0	< 0.002	u	$+\frac{2}{3}$	1.5-3.3
e	-1	0.511	d	$-\frac{1}{3}$	3.5-6.0
ν_μ	0	< 0.19	c	$+\frac{2}{3}$	$1.27^{+0.07}_{-0.11} \times 10^3$
μ	-1	105.7	s	$-\frac{1}{3}$	104^{+24}_{-34}
ν_τ	0	< 18.2	t	$+\frac{2}{3}$	$171.2 \pm 2.1 \times 10^3$
τ	-1	1776.8 ± 0.17	b	$-\frac{1}{3}$	$4.20^{+0.17}_{-0.07} \times 10^3$

Table 1.1: Standard Model fermions. The masses are taken from the 2008 PDG[14].

Fundamental bosons (spin 0, 1)			
Particle	Charge (e)	Mass (GeV/c^2)	Interaction
γ photon	0	0	electromagnetic
$W^\pm$	± 1	80.398 ± 0.025	weak
Z^0	0	91.1876 ± 0.0021	weak
g gluon	0	0	strong

Table 1.2: Standard Model gauge bosons. The masses are taken from the 2008 PDG[14].

the W and Z bosons. According to the SM, it gives rise to the masses of all particles.

Mesons are composed of a valence quark-antiquark pair. For the neutral B meson, one of these quarks is a b quark and the second one is either a d or an s quark. Some properties of these mesons are shown in Table 1.3. Here we consider the system of two neutral mesons, the B^0_d ($\bar{b}d$) and its antiparticle, the $\bar{B}^0_d$ ($b\bar{d}$) [1]. These two particles can be distinguished by an internal quantum number B for *Beauty*. This number is conserved by the strong and electromagnetic interactions but not by the

[1]In the analysis chapter, we simply refer to them as B^0 and $\overline{B}^0$, respectively.

B mesons					
Particle	Quark content	Isospin	J^P	Mass (MeV/c^2)	Mean Life (10^{-12}s)
B_u^+ or B^+	$u\bar{b}$	1/2	0^-	5279.15 ± 0.31	1.638 ± 0.011
B_d^0 or B^0	$d\bar{b}$	1/2	0^-	5279.53 ± 0.33	1.530 ± 0.009
B_s^0	$s\bar{b}$	0	0^-	5366.3 ± 0.6	$1.470^{+0.026}_{-0.027}$
B_c^+	$c\bar{b}$	0	0^-	6276 ± 4	0.46 ± 0.07

Table 1.3: B mesons. The masses and mean lifetimes are taken from the 2008 PDG[14].

weak interaction. As a result, $|B_d^0\rangle$ and $|\bar{B}_d^0\rangle$ are not mass eigenstates, causing the $B_d^0\bar{B}_d^0$ to oscillate: a pure B_d^0 at t_0 will necessarily be a superposition of B_d^0 and $\bar{B}_d^0$ at a later time $t > t_0$. This property is called *mixing* and will be discussed in detail in paragraph 1.3.

1.2 Discrete Symmetries

The Lagrangian of the SM contains different types of symmetries. It is symmetric under Lorentz transformations (products of space rotations, translations and Lorentz boosts) and contains gauge symmetries corresponding to the different interactions: U(1), SU(2) and SU(3) gauge symmetries for electromagnetic, weak and strong interactions, respectively. In addition to these continuous symmetries, there is set of three independent discrete transformations that also preserve the Minkowski interval $t^2 - \mathbf{x^2}$, namely the charge conjugation C, parity P and time-reversal T.

1.2.1 Charge Conjugation

Charge conjugation C transforms a particle to its antiparticle while keeping in the same state, namely leaving its spin and momentum unchanged. If we consider the action of charge conjugation on a Dirac field Ψ, then

$$C\Psi(t,\mathbf{x})\mathbf{C} = -\mathbf{i}(\bar{\boldsymbol{\Psi}}(\mathbf{t},\mathbf{x})\gamma^{\mathbf{0}}\gamma^{\mathbf{2}})^{\mathbf{T}}, \tag{1.1}$$

where $\bar{\Psi}(t,\mathbf{x}) = \boldsymbol{\Psi}^{\dagger}\gamma^{\mathbf{0}}$, and γ^0 and γ^2 are two of the Dirac matrices. The full set of Dirac matrices is described in detail in Appendix A.

1.2.2 Parity

The parity operator P reverses the sign of the spatial component of a four-vector, e.g. $(t,\mathbf{x}) \rightarrow (\mathbf{t},-\mathbf{x})$, while leaving the spin and angular momentum of the corresponding particle unchanged. In other words, parity transforms an object to its mirror image. The action of parity on a Dirac field Ψ can be written

$$P\Psi(t,\mathbf{x})\mathbf{P} = \gamma^{\mathbf{0}}\boldsymbol{\Psi}(\mathbf{t},-\mathbf{x}). \tag{1.2}$$

1.2.3 Time Reversal

The time reversal operator reverses the sign of the time coordinate $(t,\mathbf{x}) \rightarrow (-\mathbf{t},\mathbf{x})$. It transforms the Dirac fields as follows

$$T\Psi(t,\mathbf{x})\mathbf{T} = -\gamma^{\mathbf{1}}\gamma^{\mathbf{3}}\boldsymbol{\Psi}(-\mathbf{t},\mathbf{x}) \tag{1.3}$$

1.2.4 CP and CPT

The CP operator is the product of the C and P operators. It changes a particle into its antiparticle and reverses its momentum.

C and P, as well as CP are conserved in the strong and electromagnetic interactions. However, while C and P are not conserved in the weak interaction, their combination CP is conserved in most cases. It is only violated in certain weak processes.

It is interesting to note that the combination of the three, CPT, is strongly believed to be an invariance of nature [15]. A consequence of the CPT invariance is that CP violation in some weak decays implies a violation of T as well.

In order to keep the Lagrangian a Lorentz scalar, it has to be constructed as a combination of bilinear terms such as $\bar{\Psi}\Psi$. It is therefore useful to look at the transformation properties of such terms, which are shown in Table 1.4.

	$\bar{\Psi}\Psi$ *scalar*	$i\bar{\Psi}\gamma^5\Psi$ *pseudo scalar*	$\bar{\Psi}\gamma^\mu\Psi$ *vector*	$\bar{\Psi}\gamma^\mu\gamma^5\Psi$ *pseudo vector*	$\bar{\Psi}\sigma^{\mu\nu}\Psi$ *tensor*	∂_μ *derivative operator*
C	$+1$	$+1$	-1	$+1$	-1	$+1$
P	$+1$	-1	$(-1)^\mu$	$-(-1)^\mu$	$(-1)^\mu(-1)^\nu$	$(-1)^\mu$
T	$+1$	-1	$(-1)^\mu$	$(-1)^\mu$	$-(-1)^\mu(-1)^\nu$	$-(-1)^\mu$
CP	$+1$	-1	$-(-1)^\mu$	$-(-1)^\mu$	$-(-1)^\mu(-1)^\nu$	$(-1)^\mu$
CPT	$+1$	$+1$	-1	-1	$+1$	-1

Table 1.4: Summary of discrete symmetries properties of scalars, pseudo-scalars, vectors, pseudo-vectors, tensors and derivative operator where γ^μ, γ^5 and $\sigma^{\mu\nu}$ are defined in details in Appendix A. We use $(-1)^\mu \equiv 1$ and -1 for $\mu = 0$ and $\mu = 1, 2, 3$, respectively.

Based on these properties, one can see that the combinations of fields and derivatives that the Lagrangian is composed of are CP invariant. However, this statement is not true for the coefficients in front of these terms, which are combinations of coupling constants and masses. A complex component in any these quantities would introduce a phase shift relative to the quantities that transform under CP. As a consequence, CP would not be a true symmetry of the Lagrangian. Such complex phases therefore introduce potential room for CP symmetry violation. The overall shift has to be robust against gauge transformation, since a redefinition of the phases of any of the

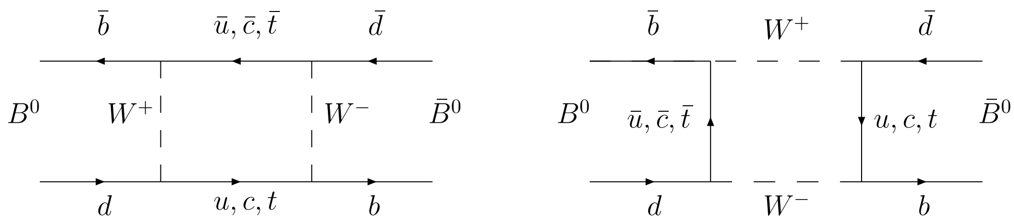

Figure 1.1: Mixing diagrams.

fields might cancel it. We will discuss where these complex phases appear in the B-meson system and how they give rise to CP asymmetry in Section 1.5.

1.3 Mixing and Time Evolution of Neutral Mesons

In this section, we are interested in the phenomen of mixing of neutral kaons and B mesons. Even though it doesn't require CP violation, it led to the first observation of CP violation. Indeed these neutral mesons can mix with their respective antiparticle via a pair of box diagrams, which are shown in Figure 1.1 for the B^0 mesons. A consequence of the property of mixing is that the flavor eigenstates have to be different from the mass eigenstates.

1.3.1 The Neutral K Meson System

In 1955, Gell-Mann and Pais were the first to predict mixing between the two neutral weak eigenstates K^0 and $\bar{K}^0$ [16]. The physical states of the kaon system - K_S^0 and

K^0_L - could be written as a combination of their flavor eigenstates, as follows:

$$|K^0_S\rangle = p|K^0\rangle + q|\bar{K}^0\rangle, \tag{1.4}$$

$$|K^0_L\rangle = p|K^0\rangle - q|\bar{K}^0\rangle. \tag{1.5}$$

If these states were also CP eigenstates, then we would have $p = q$, so that $|K^0_S\rangle$ and $|K^0_L\rangle$ would be CP-even and CP-odd, respectively.

The dominant decay mode of neutral K mesons is to $\pi^+\pi^-$, however $\pi^+\pi^-$ is a CP-even eigenstate. Therefore, if CP were to be conserved, K^0_L could not decay as such and would have to decay into three pions. The phase space for such decays is very limited (the mass of three pions being close to the kaon mass), forcing the lifetime of the CP-odd eigenstate to be much larger (thus the nomenclature S and L standing for short-lived and long-lived respectively). This lifetime difference makes the two physical states easy to separate experimentally.

In 1964, Christenson, Cronin, Fitch and Turlay discovered that the K^0_L can in fact decay into $\pi^+\pi^-$ with a branching fraction of 2×10^{-3}[1], showing that K^0_L contains a small $CP = +1$ component. This was the first evidence of CPV.

1.3.2 The Neutral B Meson System

In this thesis, we are mostly interested in the neutral pairs of B mesons, $B^0\bar{B}^0$. This system is complicated since - as in the case of K mesons - the flavor eigenstates, which define the quark content are different from the Hamiltonian eigenstates, which are associated with the observable masses and lifetimes of the particles.

The discussion that follows could be applied to K, D, B_s or B_d mesons alike, but since our topic of interest here is the mixing in the B meson system, we will only focus on the latter, and refer to it as B^0. Thereby the flavor eigenstates, we are studying are the following: $B^0 = \bar{b}d$ and $\overline{B}^0 = b\bar{d}$. The transitions $B^0 \to \bar{B}^0$ and $B^0 \to \bar{B}^0$ are due to the weak interaction as shown in Figure 1.1. If we now consider an arbitrary linear combination of the neutral B-meson flavor eigenstates

$$a|B^0\rangle + b|\overline{B}^0\rangle, \tag{1.6}$$

then the time-dependent Shrödinger equation for this system is given by

$$i\frac{d}{dt}\begin{pmatrix} a \\ b \end{pmatrix} = H \begin{pmatrix} a \\ b \end{pmatrix}, \tag{1.7}$$

where $\mathbf{H} = \mathbf{M} - \frac{\mathbf{i}}{\mathbf{2}}\mathbf{\Gamma}$, and $\mathbf{M}$ and $\mathbf{\Gamma}$ are 2×2 Hermitian matrices.

- $\mathbf{M}$, the mass matrix, is the dispersive term. Its diagonal elements determine the mass of each of the states B^0 and $\overline{B}^0$, while the off-diagonal ones describe their oscillations via off-shell (virtual) intermediate states;
- $\mathbf{\Gamma}$, the decay matrix, is the absorptive term. It describes transitions via on-shell (real) intermediate states. The diagonal terms account for all possible decay modes of each of the states, while the off-diagonal terms only contain decay modes that are common to both of them.

Since their diagonal elements describe the flavor-conserving transitions $B^0 \to B^0$ and $\overline{B}^0 \to \overline{B}^0$, whereas their off-diagonal elements represent the flavor-changing transitions $B^0 \leftrightarrow \overline{B}^0$, M and Γ must satisfy $M_{11} = M_{22} = M$ and $\Gamma_{11} = \Gamma_{22} = \Gamma$ in order to conserve CPT. One can then write H as

$$H = \begin{pmatrix} M - \frac{i}{2}\Gamma & M_{12} - \frac{i}{2}\Gamma_{12} \\ M_{12}^* - \frac{i}{2}\Gamma_{12}^* & M - \frac{i}{2}\Gamma \end{pmatrix}. \tag{1.8}$$

The Hamiltonian or mass eigenstates can be written as (as was the case for the kaon system in the previous paragraph)

$$
\begin{aligned}
|B_L\rangle &= p|B^0\rangle + q|\overline{B}^0\rangle, & (1.9)\\
|B_H\rangle &= p|B^0\rangle - q|\overline{B}^0\rangle, & (1.10)
\end{aligned}
$$

where B_L and B_H represent the light and heavy mass eigenstates respectively. p and q are complex coefficients that satisfy $|p|^2 + |q|^2 = 1$. $\frac{q}{p}$ can be defined with different phase conventions and therefore is not an observable, but $|\frac{q}{p}|$ is. When solving the eigenvalue system, we find that the mass eigenvalues are given by

$$
\begin{aligned}
M_L - \frac{i}{2}\Gamma_L = (M - \frac{i}{2}\Gamma) - \sqrt{(M_{12} - \frac{i}{2}\Gamma_{12})(M_{12}^* - \frac{i}{2}\Gamma_{12}^*)}, && (1.11)\\
M_H - \frac{i}{2}\Gamma_H = (M - \frac{i}{2}\Gamma) + \sqrt{(M_{12} - \frac{i}{2}\Gamma_{12})(M_{12}^* - \frac{i}{2}\Gamma_{12}^*)}. && (1.12)
\end{aligned}
$$

Solving for p and q, we end up with

$$
\left|\frac{q}{p}\right|^2 = \left|\frac{M_{12}^* - \frac{i}{2}\Gamma_{12}^*}{M_{12} - \frac{i}{2}\Gamma_{12}}\right| \tag{1.13}
$$

Now if we define

$$
\begin{aligned}
\Delta m_B \equiv M_H - M_L && (1.14)\\
\Delta\Gamma_B \equiv \Gamma_H - \Gamma_L, && (1.15)
\end{aligned}
$$

then the system of equations 1.11 and 1.12 becomes

$$
\begin{aligned}
(\Delta m_B)^2 - \frac{1}{4}(\Delta\Gamma_B)^2 &= 4(|M_{12}|^2 - \frac{1}{4}|\Gamma_{12}|^2), & (1.16)\\
\Delta m_B \Delta\Gamma_B &= 4\Re(M_{12}\Gamma_{12}^*), & (1.17)
\end{aligned}
$$

and

$$\frac{q}{p} = -\frac{\Delta m_B - \frac{i}{2}\Delta\Gamma_B}{2(M_{12} - \frac{i}{2}\Gamma_{12})}. \tag{1.18}$$

Unlike the neutral kaons, we do not expect the B^0 and $\bar{B^0}$ to have a significant difference in their lifetimes. Thus $\Delta\Gamma_B \ll \Gamma_B$, where $\Gamma_B = \Gamma_{B^0} \simeq \Gamma_{\bar{B^0}}$. Δm_B has been measured [14] and $\Delta m_B = (0.766 \pm 0.008)\Gamma_B$. Thus $\Delta\Gamma_B \ll \Delta m_B$ and Eqs. 1.17- 1.18 become:

$$\begin{aligned}
\Delta m_B &\simeq 2|M_{12}|, && (1.19)\\
\Delta\Gamma_B &\simeq \frac{2\Re(M_{12}\Gamma_{12}^*)}{|M_{12}|}, && (1.20)\\
\frac{q}{p} &\simeq -\frac{|M_{12}|}{M_{12}}. && (1.21)
\end{aligned}$$

As a consequence, studying the decays of the two neutral B mass eigenstates independently is made very difficult and we therefore consider their time evolution from a pure $|B^0\rangle$ or $|\overline{B}^0\rangle$ at $t = 0$. It can be written

$$\begin{aligned}
|B^0(t)\rangle &= g_+(t)|B^0\rangle + \frac{q}{p}g_-(t)|\overline{B}^0\rangle, && (1.22)\\
|\overline{B}^0(t)\rangle &= \frac{p}{q}g_-(t)|B^0\rangle + g_+(t)|\overline{B}^0\rangle, && (1.23)
\end{aligned}$$

where (ignoring $\Delta\Gamma_B$)

$$\begin{aligned}
g_+(t) &= e^{-iMt}e^{-\Gamma t/2}\cos(\Delta m_B t/2), && (1.24)\\
g_-(t) &= ie^{-iMt}e^{-\Gamma t/2}\sin(\Delta m_B t/2), && (1.25)\\
M &= \frac{1}{2}(M_H + M_L), && (1.26)\\
\Gamma &= \frac{1}{2}(\Gamma_H + \Gamma_L). && (1.27)
\end{aligned}$$

At the B factories, e^+e^- are produced at the $\Upsilon(4S)$ resonance, just above the threshold for $B^0\overline{B}^0$ pair production. The $\Upsilon(4S)$ then decays to a $B^0\overline{B}^0$ pair. This is an example of Einstein-Podolsky-Rosen [17] correlated system : the two particles are entangled and even though they can both be described by the above equations, they evolve in phase in such a way that at all times one is a B^0 and the other is a $\overline{B}^0$. The decay of one of them fixes the flavor of the other, but the latter can continue to evolve and decay as a B^0 or a $\overline{B}^0$.

1.4 Types of *CP* Violation

In this section, we will describe the three types of CP violation that can appear in the B meson system.

1.4.1 *CP* Violation in Decay

CP violation in decay or *direct CP* violation occurs when the amplitude of a decay and its CP conjugate have different magnitudes. This can happen for both neutral and charged decays.

The amplitude for B^0 decaying to a final state f contains two types of phases. The first one comes from complex parameters in the Lagrangian term that contributes to the amplitude. They transform into their conjugate under *CP*. They appear in charged weak coupling and are therefore referred to as *weak phases*. The second type of phases, called *strong phases*, appears in processes involving contributions from intermediate on-shell states, which rescatter via strong interactions. One can therefore write the amplitude

$$A_f = \langle f|H|B^0\rangle = \sum_i A_i e^{i(\Phi_i+\delta_i)}. \tag{1.28}$$

Similarly for $\overline{B}^0$ decaying to the CP conjugate final state, $\bar{f}$ we have

$$\bar{A}_{\bar{f}} = \langle \bar{f}|H|\overline{B}^0\rangle = e^{2i(\xi_f-\xi_B)} \sum_i A_i e^{i(-\Phi_i+\delta_i)}, \tag{1.29}$$

Here Φ_i and δ_i are the weak and strong phases, respectively, and the sum is done over all amplitudes that contribute to the decay. In general, the CP transformation of the states mentioned above can be written as

$$CP|B^0\rangle = e^{+i\xi_B}|\overline{B}^0\rangle, \tag{1.30}$$

$$CP|\overline{B}^0\rangle = e^{-i\xi_B}|B^0\rangle, \tag{1.31}$$

and

$$CP|f\rangle = e^{+i\xi_f}|\bar{f}\rangle, \tag{1.32}$$

$$CP|\bar{f}\rangle = e^{-i\xi_f}|f\rangle, \tag{1.33}$$

where the phases ξ_B and ξ_f are arbitrary since flavor conservation is a symmetry of the strong interaction. When looking for CP violation, one can look at the convention-independent quantity:

$$\left|\frac{\bar{A}_{\bar{f}}}{A_f}\right| = \left|\frac{\sum_i A_i e^{i(-\Phi_i+\delta_i)}}{\sum_i A_i e^{i(\Phi_i+\delta_i)}}\right| \tag{1.34}$$

CP violation emerges then when

$$\left|\frac{\bar{A}_{\bar{f}}}{A_f}\right| \neq 1. \tag{1.35}$$

It is called CP violation in decay because it is caused by interference between different

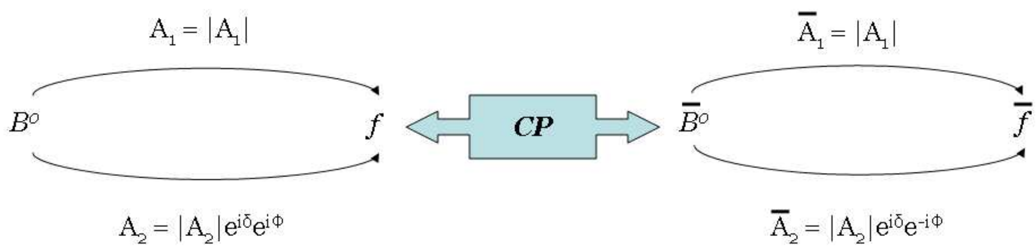

Figure 1.2: Direct CP violation with two amplitudes A_1 and A_2. $\bar{A}_1$ and $\bar{A}_2$ are CP conjugate of A_1 and A_2, respectively. If we have both a relative weak phase and strong phase between A_1 and A_2, the norm of $\bar{A}_1 + \bar{A}_2$ is different than that of $A_1 + A_2$, which translates into CP violation.

terms in the decay amplitude. CP violation in this case will only happen if at least two terms that have different weak acquire strong phases. It is seen easily when one looks at the diagram shown in Figure 1.2. In that simplified case,

$$\left|\frac{\bar{A}_{\bar{f}}}{A_f}\right| = \left|\frac{A_1 + A_2 e^{i(-\Phi+\delta)}}{A_1 + A_2 e^{i(\Phi+\delta)}}\right|. \tag{1.36}$$

The only way this can lead to CP violation is for both Φ and δ to be different from 0. Because of the strong phases involved in the measurement, CP violation can only be measured indirectly in this case.

1.4.2 *CP* Violation in Mixing

CP violation in mixing or *indirect* CP violation can occur because the mass eigenstates of the two neutral mesons are different from their CP eigenstates. The mass eigenstates are a mixture of the mass eigenstates as has previously been described by Eqs 1.9- 1.10

$$|B_{L,H}\rangle = p|B^0\rangle \pm q|\bar{B}^0\rangle, \tag{1.37}$$

where we derived the convention-independent quantity $\left|\frac{q}{p}\right|^2$ to be (see Eq 1.21)

$$\left|\frac{q}{p}\right|^2 = \left|\frac{M_{12}^* - \frac{i}{2}\Gamma_{12}^*}{M_{12} - \frac{i}{2}\Gamma_{12}}\right|. \tag{1.38}$$

Using the convention used in the previous section, we can write the CP conjugate of these states as

$$CP|B_{L,H}\rangle = pe^{2i\xi_B}|\bar{B}^0\rangle \pm qe^{-2i\xi_B}|B^0\rangle. \tag{1.39}$$

For the mass eigenstates to also be CP eigenstates, we need

$$CP|B_{L,H}\rangle = |B_{L,H}\rangle. \tag{1.40}$$

One can deduce then that, in this case, CP is violated if

$$\left|\frac{q}{p}\right| \neq 1. \tag{1.41}$$

This does not depend on the decay mode and is purely an effect of mixing. Following the discussion in section 1.3 and recalling Eq. 1.21, we can infer that the effects of CP violation in mixing should be very small in the B meson system. However, it is the main contribution of CP violation in the K meson system observed when CP violation was discovered in 1964 [1].

1.4.3 *CP* Violation in the Interference between Decays With and Without Mixing

CP violation in the interference of decays with and without mixing occurs when B^0 and $\overline{B}^0$ decay to the same final state. Let us consider the time-dependent CP

asymmetry

$$a_{f_{CP}}(t) = \frac{\Gamma(B^0(t) \to f_{CP}) - \Gamma(\bar{B}^0(t) \to f_{CP})}{\Gamma(B^0(t) \to f_{CP}) + \Gamma(\bar{B}^0(t) \to f_{CP})}. \tag{1.42}$$

If $A_{f_{CP}} = \langle f_{CP}|H|B^0\rangle$ and $\bar{A}_{f_{CP}} = \langle f_{CP}|H|\bar{B}^0\rangle$, then using the time evolution notations given in Eqs 1.22 and 1.23, we can write

$$\langle f_{CP}|H|B^0(t)\rangle = A_{f_{CP}}(g_+(t) + \lambda g_-(t)), \tag{1.43}$$

$$\langle f_{CP}|H|\bar{B}^0(t)\rangle = A_{f_{CP}}\frac{p}{q}(g_-(t) + \lambda g_+(t)), \tag{1.44}$$

where $\lambda = \frac{q}{p}\frac{\bar{A}_{f_{CP}}}{A_{f_{CP}}}$. λ is an important quantity here. It is convention-independent and we have already seen in the previous paragraphs that CP is violated if $|\frac{q}{p}| \neq 1$ or $|\frac{A}{\bar{A}}| \neq 1$ and either one of these statement can lead to $|\lambda| \neq 1$. In the following, we will get a better understanding of why this quantity is so fundamental in our search for CP violation. Since $\Gamma(B^0(t) \to f_{CP}) \propto |\langle f_{CP}|H|B^0(t)\rangle|^2$ and $\Gamma(\overline{B}^0(t) \to f_{CP}) \propto |\langle f_{CP}|H|\overline{B}^0(t)\rangle|^2$, it is useful to simplify these expressions so that:

$$\begin{aligned} |\langle f_{CP}|H|B^0(t)\rangle|^2 &= |A_{f_{CP}}|^2 e^{-\Gamma t}(\frac{1+|\lambda|^2}{2} + \frac{1-|\lambda|^2}{2}\cos\Delta m_B t \qquad (1.45)\\ &- \Im\lambda \sin\Delta m_B t) \\ &\propto |A_{f_{CP}}|^2 e^{-\Gamma t}(1 + C\cos\Delta m_B t - S\sin\Delta m_B t), \qquad (1.46) \end{aligned}$$

where

$$C = \frac{1-|\lambda|^2}{1+|\lambda|^2}, \tag{1.47}$$

$$S = \frac{2\Im\lambda}{1+|\lambda|^2}. \tag{1.48}$$

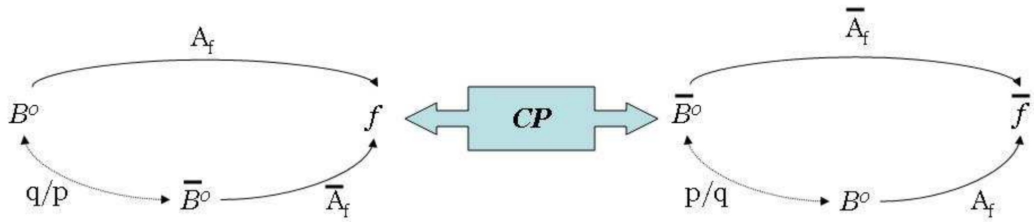

Figure 1.3: CP violation in the interference between mixing and decay.

Similarly, we find

$$
\begin{aligned}
|\langle f_{CP}|H|\bar{B}^0(t)\rangle|^2 &= |A_{f_{CP}}|^2 e^{-\Gamma t}(\frac{1+|\lambda|^2}{2} - \frac{1-|\lambda|^2}{2}\cos\Delta m_B t \qquad (1.49)\\
&+ \Im\lambda \sin\Delta m_B t)\\
&\propto |A_{f_{CP}}|^2 e^{-\Gamma t}(1 - C\cos\Delta m_B t + S\sin\Delta m_B t). \qquad (1.50)
\end{aligned}
$$

The time-dependent asymmetry then becomes

$$a_{f_{CP}}(t) = C\cos\Delta m_B t - S\sin\Delta m_B t. \qquad (1.51)$$

With this simplified notation, one can easily see that for CP to be conserved, both S and C have to be 0. From the definition of C, we see that $C \neq 0$ is the condition for direct CP violation. However, we see that even if the conditions for CP violation in mixing and in decay are not fulfilled ($|\lambda| = 1$), CP violation is still possible if $\Im\lambda \neq 0$. This type of CP violation is due to the interference between decays with and without mixing. One can see that no strong phase is involved here, which is a great advantage, but it requires a time-dependent study of the decay. In the next section, we will go over some concepts of the Standard Model that are important in the determination of this CPV effect.

1.5 CP Violation in the Standard Model

In this section, we take a closer look at the Lagrangian of the SM and study how CPV emerges from it. We will see that it is due to a single phase in the quark mixing matrix (CKM) which will be described in detail.

1.5.1 The Standard Model Lagrangian

The SM is the theory that describes particle physics, i.e. the quarks, leptons and their interactions. It has been very successful and one needs to understand how CP comes to be violated in this model in order to understand effects that may be due to New Physics.

The SM is a quantum field theory, based on the gauge invariance principle. The gauge symmetry of the SM is $SU(3)_C \times SU(2)_L \times U(1)_Y$, where $SU(3)_C$ and $SU(2)_L \times U(1)_Y$ account for the strong and the electroweak interactions, respectively. The electroweak interaction is the unified description of the electromagnetic and the weak interactions. Glashow, Weinberg and Salam were awarded the Physics Nobel prize in 1979 for their contributions to the unification [18]. They unified the $SU(2)_L$ gauge group with the $U(1)_Q$ gauge group to the $SU(2)_L \times U(1)_Y$ electroweak group.

The gauge bosons that are the mediators of the interactions were described in Table 1.2 in Section 1.1. The fundamental fermions can be organized in three families of left-handed doublets and right-handed singlets, constituting the fundamental representation of $SU(2)_L \times U(1)_Y$. They have similar properties but differ by their mass. They can be classified by their quantum numbers of weak isospin I, the third component of their weak isospin I_3 and their weak hypercharge Y. Their electric charge

Q is related to these numbers by the Gell-Mann-Nishijima relation

$$Q = I_3 + Y. \tag{1.52}$$

Table 1.5 shows a summary of the three families of fermions, along with the corresponding quantum numbers.

First family	Second family	Third family	I	I_3	Y	Q
$L_1 = \begin{pmatrix} \nu_e \\ e^- \end{pmatrix}_L$	$L_2 = \begin{pmatrix} \nu_\mu \\ \mu^- \end{pmatrix}_L$	$L_3 = \begin{pmatrix} \nu_\tau \\ \tau^- \end{pmatrix}_L$	$1/2$	$+1/2$ $-1/2$	$-1/2$	0 -1
e_R^-	μ_R^-	τ_R^-	0	0	-1	-1
$Q_1 = \begin{pmatrix} u \\ d \end{pmatrix}_L$	$Q_2 = \begin{pmatrix} c \\ s \end{pmatrix}_L$	$Q_3 = \begin{pmatrix} t \\ b \end{pmatrix}_L$	$1/2$	$+1/2$ $-1/2$	$+1/6$	$+2/3$ $-1/3$
u_R	c_R	t_R	0	0	$+2/3$	$+2/3$
d_R	s_R	b_R	0	0	$-1/3$	$-1/3$

Table 1.5: Fermions and their associated quantum numbers. L and R denote left-handed and right-handed fields, respectively.

Let $Q^I_{Li} = \begin{pmatrix} u^I_i \\ d^I_i \end{pmatrix}_L$ be the electroweak eigenstate (in the interaction basis I) of the i^{th} family ($i = 1, 2, 3$), with $\mathbf{u} = (u, c, t)$ and $\mathbf{d} = (d, s, b)$. Then the charge current part of the Lagrangian which describes the interaction of the quarks with the gauge bosons of $SU(2)_L$ is of the form

$$\mathcal{L}^q_W = -\frac{g}{\sqrt{2}} \sum_i (\bar{u}^I_{Li}\gamma^\mu d^I_{Li} W^+_\mu + \bar{d}^I_{Li}\gamma^\mu u^I_{Li} W^-_\mu), \tag{1.53}$$

where g is the weak coupling constant.

We can build a gauge invariant field theory of the electroweak interaction using $SU(2)_L \times U(1)_Y$ as the group of gauge transformations under which the Lagrangian is invariant. However this symmetry has to be broken by the Higgs mechanism for the $W^\pm$ and the Z^0 to have a mass.

Higgs Field

One of the important features of the SM is the description of the mass generation of leptons and the massive bosons W^+, W^- and Z^0. The lepton mass terms that appear in the SM-Lagrangian are of the form $m_f \bar{\Psi}_f \Psi_f$, where m_f and Ψ_f are the mass and the Dirac spinor of the fermion f respectively. However, simply adding these terms to the Lagrangian would break the local $SU(2)$ gauge invariance. The solution to this problem is to introduce a single complex scalar, weakly-interacting Higgs-double

$$\phi(\mathbf{x}) = \begin{pmatrix} \phi^+(x) \\ \phi^0(x) \end{pmatrix}. \tag{1.54}$$

It has a non zero vacuum expectation value that allows spontaneous breaking of the $SU(2)_L \times U(1)_Y$ symmetry

$$< \phi > = \frac{1}{\sqrt{2}} \begin{pmatrix} 0 \\ v \end{pmatrix}. \tag{1.55}$$

This so-called Higgs mechanism was named after Peter Higgs who first suggested this idea in the 1960s [19]. The Higgs boson has not been observed yet and is still the object of a long search that is hoped to come to an end at the LHC [20].

The Higgs boson can interact with the fermions in the model and the corresponding coupling terms in the Lagrangian are the so-called Yukawa interactions. They are fundamental as they are the only electroweak part of the Lagrangian which can violate CP.

Yukawa Interaction

The Yukawa term of the Lagrangian for the quarks only (a similar one for the leptons also exist) is given by

$$\mathcal{L}_Y^q = -\sum_{i,j}[Y_{ij}^u \bar{Q}_{Li}^I \tilde{\phi} u_{Rj}^I + Y_{ij}^d \bar{Q}_{Li}^I \phi d_{Rj}^I + h.c.], \tag{1.56}$$

where Y_{ij}^d, Y_{ij}^d and Y_{ij}^d are the complex Yukawa coupling constants, and $\tilde{\phi} = \begin{pmatrix} \phi^0(x) \\ -\phi^{+*}(x) \end{pmatrix}$. One can easily see how CPV arises here. Each term and its CP conjugate are represented in the Lagrangian, i.e. $\bar{Q}_{Li}^I \phi d_{Rj}^I$ and its CP conjugate $\bar{d}_{Ri}^I \phi^\dagger Q_{Li}^I$. The difference is in their coefficient, i.e. Y_{ij}^d and Y_{ij}^{d*} respectively. So CP is not a symmetry of this Lagrangian if these three matrices are not real.

Mass Terms

After the spontaneous symmetry breaking, one can perform a gauge transformation and write the Higgs field as

$$\phi(\mathbf{x}) = \frac{1}{\sqrt{2}} \begin{pmatrix} 0 \\ v + H(x) \end{pmatrix}. \tag{1.57}$$

This particular gauge is the unitarity gauge. In this gauge, the Yukawa term can be simplified and the following mass terms arise

$$\mathcal{L}_{mass}^q = -\sum_{i,j}[M_{ij}^u \bar{u}_{Li}^I u_{Rj}^I + M_{ij}^d \bar{d}_{Li}^I d_{Rj}^I + h.c.], \tag{1.58}$$

where

$$
\begin{aligned}
M_{ij}^{u} &= Y_{ij}^{u}\frac{v}{\sqrt{2}}, && (1.59)\\
M_{ij}^{d} &= Y_{ij}^{d}\frac{v}{\sqrt{2}}. && (1.60)
\end{aligned}
$$

It is now more intuitive to turn to a base where the matrices M^u and are M^d diagonalized. To do this, we use unitary 3×3 transformation matrices, V_L^u, V_R^u, V_L^d and V_R^d such that

$$
V_L^u M_u V_R^{u\dagger} = \begin{pmatrix} M_u & 0 & 0 \\ 0 & M_c & 0 \\ 0 & 0 & M_t \end{pmatrix} \tag{1.61}
$$

and

$$
V_L^d M_d V_R^{d\dagger} = \begin{pmatrix} M_d & 0 & 0 \\ 0 & M_s & 0 \\ 0 & 0 & M_b \end{pmatrix}. \tag{1.62}
$$

By definition, the mass eigenstates of the quarks are related to their electroweak counterpart by

$$
\begin{aligned}
u_{Li} &= V_{Lij}^{u} u_{Lj}^{I}, && (1.63)\\
u_{Ri} &= V_{Rij}^{u} u_{Rj}^{I}, && (1.64)\\
d_{Li} &= V_{Lij}^{d} d_{Lj}^{I}, && (1.65)\\
d_{Ri} &= V_{Rij}^{d} d_{Rj}^{I}. && (1.66)
\end{aligned}
$$

If we now write down the Lagrangian term that describes the coupling of the W^+ and W^- to the fermions (see Eq. 1.53), so that it is expressed using the mass eigenstates rather than the interaction eigenstates, we have

$$\mathcal{L}_{\mathcal{W}} = -\frac{g}{\sqrt{2}}\sum_{i,j}[\bar{u}_{Li}\gamma^{\mu}(V_L^u V_L^{d\dagger})_{ij}d_{Lj}W_{\mu}^{+} + h.c.]. \tag{1.67}$$

A matrix component appears of the form $(V_L^u V_L^{d\dagger})_{ij}$. $\mathbf{V} = \mathbf{V_L^u V_L^{d\dagger}}$ is called the *Cabibbo-Kobayashi-Maskawa* matrix or CKM matrix.

1.5.2 The CKM Matrix and the Unitarity Triangle

In order to explain the CPV effect that had been observed in the kaon system in 1964 [1], Kobayashi and Maskawa were awarded the 2008 Nobel Prize in Physics for their formulation of the *KM Mechanism*, which extended the idea of the quark mixing attributed to Nicola Cabibbo [4], from two to three families [3].

Conditions for CPV

The fact that the mass matrices, and consequently the CKM matrix contain complex phases does not necessarily imply that they will generate CPV. Let us calculate the number of independent physical parameter of the CKM matrix. A unitary matrix of dimension N has N^2 parameters, but they are not all significant. Indeed, it is possible to reduce the number of phases by applying a transformation

$$V_{CKM} \Rightarrow D_u V_{CKM} D_d^*, \tag{1.68}$$

where D_u and D_d are diagonal phase matrices. The latter can be defined so that the transformation eliminates $2N-1$ of the $2N$ initial phases. This leaves V_{CKM} with $(N-1)^2$ independent parameters. Amongst these, $\frac{N(N-1)}{2}$ are mixing angles, i.e. Euler angles characteristic of a rotation matrix of dimension N. As a result, only $(N-1)^2 - \frac{N(N-1)}{2} = \frac{(N-1)(N-2)}{2}$ independent phases are left. We can thereby conclude that three families of quarks are needed for V_{CKM} to have a non-trivial complex phase. This phase is called the Kobayahsi-Maskawa phase [3], δ.

Nonetheless, even in the SM with three quark generations, CP is not necessarily violated. If two quarks had the same mass, one mixing angle and one phase could be removed from V_{CKM}. If one of the mixing angles were 0 or $\pi/2$, or δ were 0 or π, CP would likewise be conserved. All these conditions can be summarized in one condition, which is independent of phase convention [21], by defining the commutator of mass matrices in the interaction basis I

$$iC_J = [M_U M_U^\dagger, M_D M_D^\dagger]. \tag{1.69}$$

Then

$$\det C_J = -2J(m_t^2 - m_c^2)(m_c^2 - m_u^2)(m_t^2 - m_u^2)(m_b^2 - m_s^2)(m_s^2 - m_d^2)(m_b^2 - m_d^2), \tag{1.70}$$

where J is the Jarslkog invariant. Using the unitarity condition of V_{CKM}, one can write

$$\Im[V_{ij} V_{kl} V_{il}^* V_{kj}^*] = J \sum_{m,n=1}^{3} \epsilon_{ikm} \epsilon_{jln}, \tag{1.71}$$

where (i,k) and (j,l) represent type "u" and "d", respectively. The general condition for the mass matrices in the interaction basis to violate CP is therefore

$$\det C_J \neq 0 \Leftrightarrow CPV, \tag{1.72}$$

or in the case where the quarks masses are not degenerate

$$J \neq 0 \Leftrightarrow CPV. \tag{1.73}$$

V_{CKM} Parametrization

By convention, we write the CKM matrix in order of increasing quark mass values:

$$V_{CKM} = \begin{pmatrix} V_{ud} & V_{us} & V_{ub} \\ V_{cd} & V_{cs} & V_{cb} \\ V_{td} & V_{ts} & V_{tb} \end{pmatrix}. \tag{1.74}$$

Since $\mathbf{V}$ is a complex matrix, it may have up to eighteen real parameters. However it is possible to reduce the number of parameters by using the unitarity conditions of the matrix:

$$\sum_{k=1}^{3} = V_{ki} V_{kj}^{*} = \delta_{if}, \tag{1.75}$$

where $i, j = 1, 2, 3$. This system of nine equations leaves nine independent parameters. As we have seen in other cases before, the Lagrangian stays invariant under phase shifts of the quark mass eigenstates fields such as $u_{Li} \rightarrow e^{i\phi_u^q} u_{Li}$. One can choose a phase transformation that eliminates five out of the six independent phase parameters, which leaves us only four independent parameters total. The so-called *standard representation* is defined by the combination of three rotation matrices - one of which is complex - using three mixing angles θ_{12}, θ_{13} and θ_{23}, and a phase δ, the CP violating term. It results in

$$V = \begin{pmatrix} c_{12}c_{13} & s_{12}c_{13} & s_{13}e^{-i\delta} \\ -s_{12}c_{23} - c_{12}s_{23}s_{13}e^{i\delta} & c_{12}c_{23} - s_{12}s_{23}s_{13}e^{i\delta} & s_{23}c_{13} \\ -s_{12}s_{23} - c_{12}c_{23}s_{13}e^{i\delta} & -c_{12}s_{23} - s_{12}c_{23}s_{13}e^{i\delta} & c_{23}c_{13} \end{pmatrix}, \tag{1.76}$$

where $c_{ij} = \cos\theta_{ij}$ and $s_{ij} = \sin\theta_{ij}$. In this parametrization, the Jarslkog invariant is given by

$$J = c_{12}c_{23}c_{13}^2 s_{12}s_{23}s_{13}\sin\delta, \tag{1.77}$$

which shows explicitly that for $J \neq 0$, all the mixing angles must be different from 0 or $\pi/2$ and the phase different from 0 or π.

Measurements of $|V_{ud}|, |V_{cb}|$ and $|V_{ub}|$ show that there is a hierarchy in the mixing angles, so we can expand the CKM matrix in powers of $\lambda = \sin\theta_{12} \approx 0.23$ [14]. Wolfenstein took advantage of a few observations to introduce a new parametrization of the matrix:

- Comparing 1.74 and 1.76, one can see that $s_{13} = |V_{ub}|$, which is measured to be of the order of λ^3. This implies that to that order, $c_{13} \sim 1$, which allows us to simplify 1.76 greatly.
- As a consequence of the above, one can see that $s_{23} \sim V_{cb}$, which is expected to be of the order of λ^2 experimentally.
- Finally, since δ is always coupled to $s_{13} \sim \lambda^3$ in the matrix, we can deduce that the term $s_{13}e^{-i\delta}$ is suppressed.

Following this observed hierachy, one can develop the CKM matrix in powers of λ, as suggested by Wolfenstein [22]

$$V_{CKM} = \begin{pmatrix} 1 - \frac{\lambda^2}{2} & \lambda & A\lambda^3(\rho - i\eta) \\ -\lambda & 1 - \frac{\lambda^2}{2} & A\lambda^2 \\ A\lambda^3(1 - \rho - i\eta) & -A\lambda^2 & 1 \end{pmatrix} + O(\lambda^4), \tag{1.78}$$

including terms up to the order of λ^3. Using this parametrization, the order of magnitude of each terms becomes obvious.

In order to get better precision, however, it is interesting to use an exact parametrization, based on the standard representation. We can then define the parameters (A, λ, ρ, η) as

$$
\begin{aligned}
s_{12} &\equiv \lambda, && (1.79)\\
s_{23} &\equiv A\lambda^2, && (1.80)\\
s_{13}e^{-i\delta} &\equiv A\lambda^3(\rho - i\eta). && (1.81)\\
& && (1.82)
\end{aligned}
$$

The CKM matrix written in this representation is not subject to approximations and satisfies unitarity. It also makes it possible to develop it to higher orders, as follows:

$$
\begin{aligned}
V_{ud} &= 1 - \frac{1}{2}\lambda^2 - \frac{1}{8}\lambda^4 + O(\lambda^6), && (1.83)\\
V_{us} &= \lambda + O(\lambda^7), && (1.84)\\
V_{ub} &= A\lambda^3(\rho - i\eta), && (1.85)\\
V_{cd} &= -\lambda + \frac{1}{2}A^2\lambda^5[1 - 2(\rho + i\eta)] + O(\lambda^7), && (1.86)\\
V_{cs} &= 1 - \frac{1}{2}\lambda^2 - \frac{1}{8}\lambda^8(1 + 4A^2) + O(\lambda^7), && (1.87)\\
V_{cb} &= A\lambda^2 + O(\lambda^8), && (1.88)\\
V_{td} &= A\lambda^3[1 - \bar{\rho} - i\bar{\eta}] + O(\lambda^7), && (1.89)\\
V_{ts} &= -A\lambda^2 + \frac{1}{2}A\lambda^4[1 - 2(\rho + i\eta)] + O(\lambda^6), && (1.90)\\
V_{tb} &= 1 - \frac{1}{2}A^2\lambda^4 + O(\lambda^6), && (1.91)
\end{aligned}
$$

where

$$
\begin{aligned}
\bar{\rho} &= \rho\left(1 - \frac{\lambda^2}{2}\right), && (1.92)\\
\bar{\eta} &= \eta\left(1 - \frac{\lambda^2}{2}\right). && (1.93)
\end{aligned}
$$

Unitarity Triangle

We have already mentioned the unitarity conditions of the CKM matrix in Eq 1.75. Let us have a closer look at the orthogonality conditions ($i \neq j$), which lead to the following three equations:

$$a) \quad V_{ud}V_{us}^*(\lambda) + V_{cd}V_{cs}^*(\lambda) + V_{td}V_{ts}^*(\lambda^5) = 0, \tag{1.94}$$

$$b) \quad V_{us}V_{ub}^*(\lambda^4) + V_{cs}V_{cb}^*(\lambda^2) + V_{ts}V_{tb}^*(\lambda^2) = 0, \tag{1.95}$$

$$c) \quad V_{ud}V_{ub}^*(\lambda^3) + V_{cd}V_{cb}^*(\lambda^3) + V_{td}V_{tb}^*(\lambda^3) = 0, \tag{1.96}$$

where the order of magnitude of each term is shown in parentheses. As the sum of three complex numbers adding up to zero, each can be represented by a triangle in the complex plane, as shown in figure 1.4. The area of each angle in the triangles

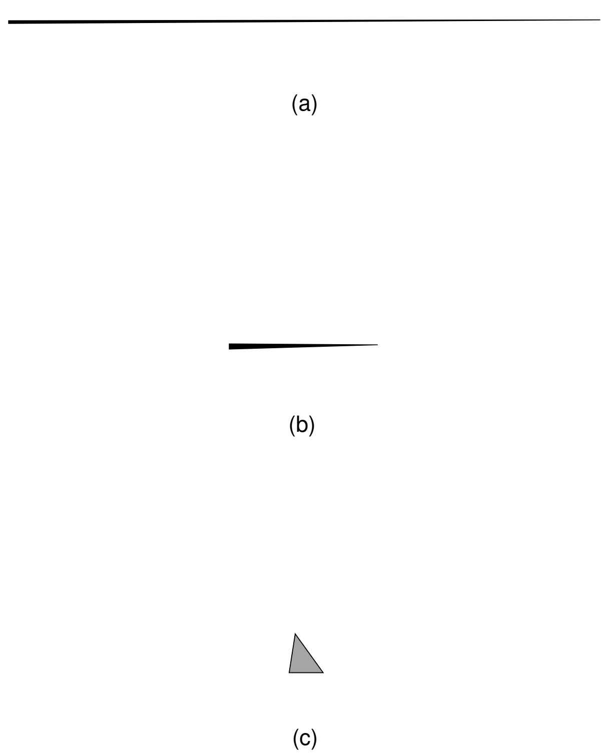

Figure 1.4: "Unitarity triangles" reflecting equations 1.94 - 1.96, respecting the magnitude of each term.

gives a direct measure of the magnitude of the violation of CP. They all have the same surface area $|J|/2$. One can see from this graphical representation that the most interesting place to look for CPV is in the third triangle, which one can intuitively relate to the B system while looking at Equation 1.96. From now on, we will therefore only refer to the third triangle as the *Unitarity Triangle* (UT). Equation 1.96 is equivalent to

$$\frac{V_{ud}V_{ub}^*}{V_{cd}V_{cb}^*} + 1 + \frac{V_{td}V_{tb}^*}{V_{cd}V_{cb}^*} = 0, \tag{1.97}$$

where we just divided the equation by the second term. Written in this form, this equation corresponds to the triangle shown in Figure 1.6. The triangle only depends

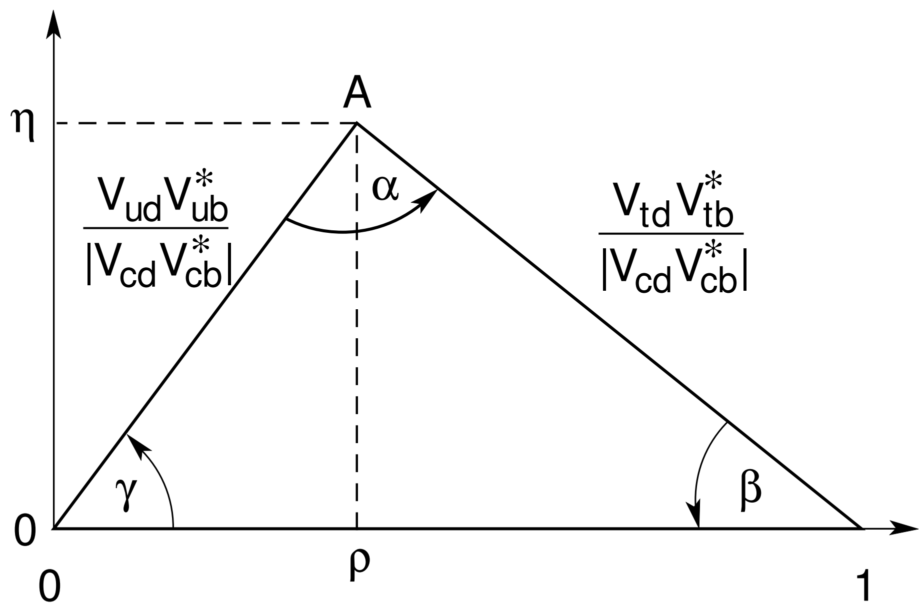

Figure 1.5: Unitarity triangle normalized by $V_{cd}V_{cb}^*$ in the complex plane.

on the CKM parameters ρ and η and its angles are

$$\alpha \equiv \arg\left[-\frac{V_{td}V_{tb}^*}{V_{ud}V_{ub}^*}\right], \beta \equiv \arg\left[-\frac{V_{cd}V_{cb}^*}{V_{td}V_{tb}^*}\right], \gamma \equiv \arg\left[-\frac{V_{ud}V_{ub}^*}{V_{cd}V_{cb}^*}\right]. \tag{1.98}$$

The main goal of the *BABAR* experiment is to study the properties of the UT. In this thesis, we are interested in determining sin2β.

Constraints on the UT

Some measured parameters already put a number of constraints on the triangle, therefore limiting the possible values of sin2β. The current measurements are in great agreement with the theoretical expectations as shown on Figure 1.6, compiled by the *CKMFitter* group [23].

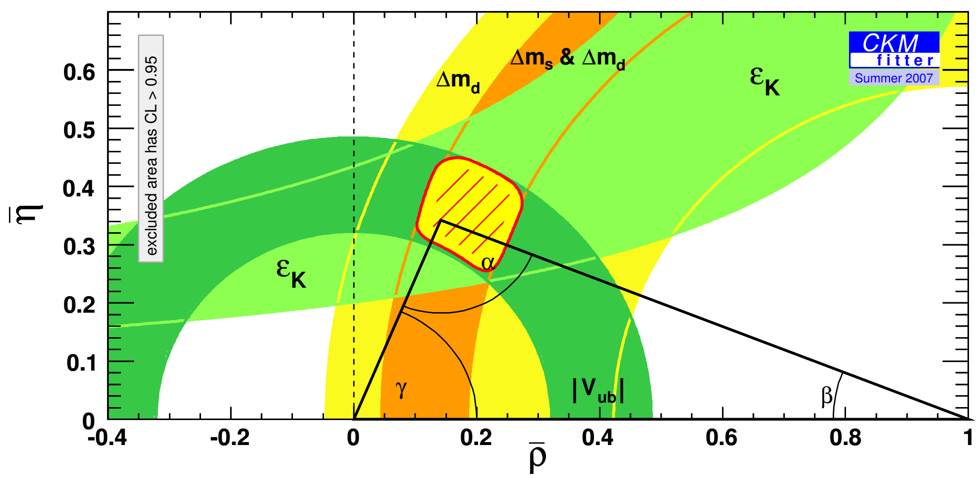

Figure 1.6: Unitarity triangle constraints [23].

In particular, Δm_B (which corresponds Δ_{Bd} or Δm_d here), the $B^0\overline{B}^0$ oscillation frequency studied in section 1.3 gives a good estimate of the value of $|V_{tb}^*V_{td}|^2$. The amplitude of the diagrams shown in Figure 1.1 indeed satisfies

$$M_{12} \propto (V_{qb}^* V_{qd} m_q)^2, \tag{1.99}$$

where $q \in (u, c, t)$. However we have seen that all $V_{qb}^*V_{qd}$ are all of order of magnitude λ^3, according to Equation 1.78, meaning that M_{12} is dominated by the diagrams containing the top quark. If we recall Equation 1.21, then we can conclude that

$$\frac{q}{p} \simeq -\frac{M_{12}^*}{|M_{12}|} \propto \frac{V_{td}V_{tb}^*}{V_{td}^*V_{tb}} = e^{-2i\beta}. \tag{1.100}$$

Likewise, according to Equation 1.19,

$$\Delta m_B \simeq 2|M_{12}| \propto |V_{tb}^* V_{td}|^2. \tag{1.101}$$

The value measured for Δm_B is therefore a constraint on the length of one of the sides of the triangle.

The length of the second complex side is also calculated using $|V_{ub}|$ with additional inputs from $|V_{us}|$ and $|V_{cb}|$ and both are constraints are depicted in Figure 1.6.

Δm_s, the mass difference between the light and heavy B_s^0 mesons, is another strong constraint on the UT. In itself, it only has a weak dependence on the UT parameters, but it is very useful to improve the constraint on the measurement of Δm_d. Measurements show that it has a lower limit of $\Delta m_d > 14.4\text{ps}^{-1}$ at a 95% Confidence Level (CL).

Finally the CPV parameter in the K^0 system, ϵ_K, is defined as

$$\epsilon_K = \frac{2}{3}\eta_{+-} + \frac{1}{3}\eta_{00}, \tag{1.102}$$

and is also shown on Figure 1.6. η_{+-} and η_{00} are the ratio between the disintegration of the K_L^0 and K_S^0 to two charged pions and two neutral pions respectively. Reference [14] reports $\epsilon_K = (2.229 \pm 0.012) \times 10^{-3}$. It gets contributions from several terms in the CKM matrix.

The constraints due to the measurement of sin2β are added when the final results are discussed in the conclusion.

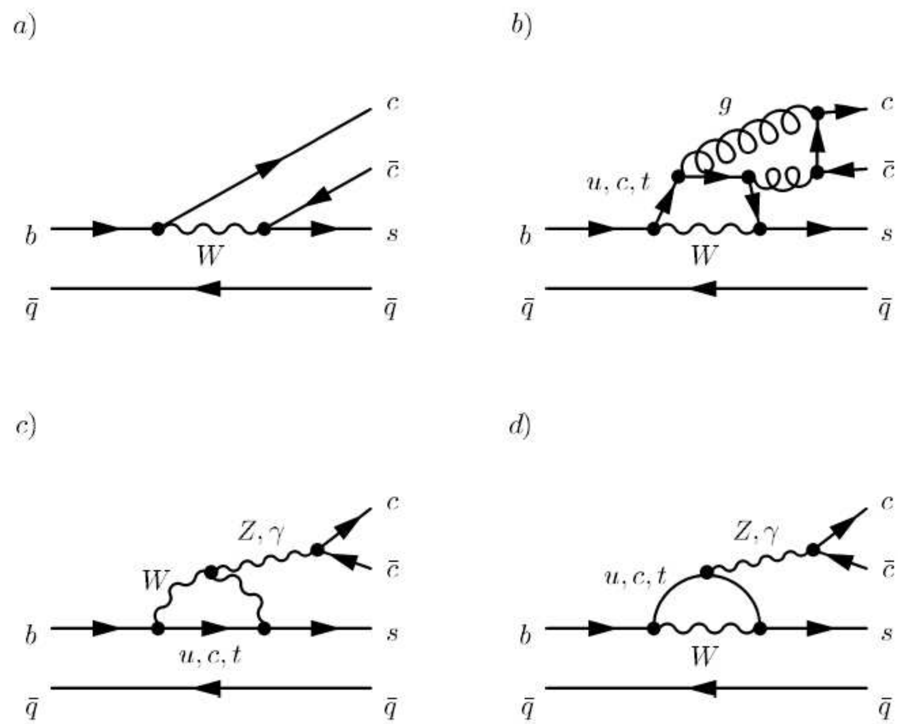

Figure 1.7: Feynman diagrams contributing to the $b \to c\bar{c}s$ decays. a) tree diagram; b) strong penguin diagram; c,d) electroweak penguin diagram.

1.5.3 *CP* Violation in $B^0 \to J/\psi\, K^0_L$

In the SM, two classes of quark-level diagrams contribute to hadronic B decays, the tree and penguin diagrams, as shown in Figure 1.7 for the $b \to c\bar{c}s$ decays. $B^0 \to J/\psi\, K^0_L$ is one of the decays studied at BABAR that enters this category and is the object of this thesis. Let $A(c\bar{c}s)$ be the amplitude describing B decays including a $b \to c\bar{c}s$ transition. It can be written as the sum of three terms with definite CKM coefficients:

$$A(c\bar{c}s) = V_{tb}V^*_{ts}P^t_s + V_{cb}V^*_{cs}(T_{c\bar{c}s} + P^c_s) + V_{ub}V^*_{us}P^u_s, \tag{1.103}$$

where P and T are the contributions from the tree and penguin diagrams, respectively. Using the unitarity relation, $V_{tb}V_{ts}^* = -V_{ub}V_{us}^* - V_{cb}V_{cs}^*$, it can be simplified, as follows

$$A(c\bar{c}s) = V_{cb}V_{cs}^*(T_{c\bar{c}s} + P_s^c - P_s^t) + V_{ub}V_{us}^*(P_s^u - P_s^t). \tag{1.104}$$

The dominant term $T_{c\bar{c}s}$ is color-suppressed. Indeed the s and $\bar{c}$ quarks generated by the W contribute to two different mesons. Consequently, the c and $\bar{c}$ quarks, which were initially color independent, must have colors that are compatible to form a meson, likewise for the s and the spectator quarks.

We recall (see Equation 1.85- 1.88)

$$V_{cb}V_{cs}^* \simeq A\lambda^2, \tag{1.105}$$

$$V_{ub}V_{us}^* \simeq A\lambda^4(\rho - i\eta). \tag{1.106}$$

The penguin diagrams with an intermediate u quark are the only ones that have a phase different from the dominating term (they are the only ones with a complex part), but they are Cabibbo-suppressed. Furthermore, the penguin diagrams are suppressed by a loop factor compared to the tree diagrams, aside from the CKM factors. $A(c\bar{c}s)$is therefore dominated by a unique weak phase and one can consider that direct CPV is absent in this type of decays to a very good approximation. It makes them very "clean" and they are commonly referred to as the *golden* modes.

If we now concentrate on the $B^0 \to J/\psi\, K_L^0$, we can consider K_L^0 to be a CP eigenstate to a good approximation, with eigenvalue -1. Consequently, the eigenvalue of the final state is $\eta_{(J/\psi\, K_L^0} = +1$. Likewise $\eta_{J/\psi\, K_S^0} = -1$. Since $B^0 \to J/\psi\, K^0$ and $\bar{B}^0 \to J/\psi\, \bar{K}^0$, we have to take into account the $K^0\bar{K}^0$ mixing in order to have the same final state for B^0 and $\overline{B}^0$. We have seen previously that this is indeed a necessary condition to study CPV in the B meson system. We obtain

$$\begin{aligned}
\lambda_f &= \eta_f \frac{q}{p}\frac{\bar{A}_{\bar{f}CP}}{A_{fCP}}\left(\frac{q}{p}\right)_K && (1.107)\\
&= \eta_f \frac{V_{td}V_{tb}^*}{V_{td}^*V_{tb}}\frac{V_{cb}V_{cs}^*}{V_{cb}^*V_{cs}}\frac{V_{cs}V_{cd}^*}{V_{cs}^*V_{cd}} && (1.108)\\
&= \eta_f e^{-2i\beta}. && (1.109)
\end{aligned}$$

We applied a few approximations to obtain this result. We neglected

- indirect CPV in the B meson system, i.e. $|q/p| = 1$;
- indirect CPV in the kaon system, i.e. $|q/p|_K = 1$;
- CPV in the decay, i.e.$|\bar{A}_{\bar{f}CP}/A_{fCP}| = 1$.

To generalize to any of the final state f, product of a $b \to c\bar{c}s$ transition, we can write in simple terms

$$\Im\lambda_f = -\eta_f \sin 2\beta. \qquad (1.110)$$

This is also equivalent to

$$\begin{aligned}
S &= -\eta_f \sin 2\beta, && (1.111)\\
C &= 0. && (1.112)
\end{aligned}$$

And recalling Equations 1.46 and 1.50, the time evolution of the B mesons $f_\pm(t)$ is

$$f_\pm(t) = \frac{\Gamma}{4}e^{-\Gamma t}(1 \pm S\sin(\Delta m_B t), \qquad (1.113)$$

where the sign + (-) corresponds to an initial state B^0 ($\overline{B}^0$).

To conclude, we have shown that the B meson system is well-adapted to the study of CPV since we expect large asymmetries thanks to the presence of quarks of the three families at the tree diagram level. The unique non removable phase of the CKM matrix is the source of CPV in the SM and leads to effects that can be tested experimentally, especially in the golden modes. They enable us to determine the CKM parameters in a clean manner.

Chapter 2

PEP-II and the *BABAR* Detector

The *BABAR* detector is located at the SLAC National Accelerator Laboratory, operated by Stanford University for the U.S. Department of Energy. Its primary goal is to study time-dependent CP asymmetries in neutral B mesons, which necessitates:

- a "B factory" - to attain a high enough precision on the measurement of sin2β, it is necessary to produce hundreds of millions of B mesons since the branching fractions of the charmonium $K^{0(*)}$ are of the order of 10^{-4};
- effective tagging of the flavor of the second B meson in the decay;
- accurate measurement of the relative life time of the two B mesons.

The first section of this chapter gives an overview of the PEP-II facility. The description of the *BABAR* detector is given in the second part of this chapter. I contributed to the running of the detector while being commissioner for the radiation protection system of the silicon vertex tracker, and therefore will give a detailed description of this system in section 2.4.

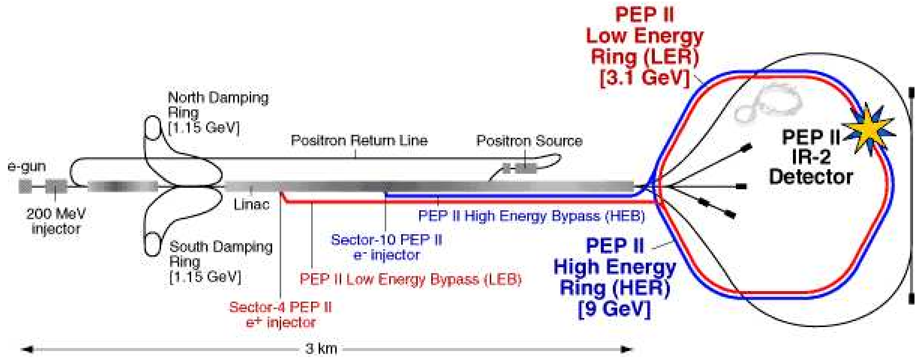

Figure 2.1: Representation of the B-meson factory at the SLAC National Accelerator Laboratory.

2.1 Production of $B\bar{B}$ pairs at the e^+e^- PEP-II Storage Rings

The linear accelerator (LINAC) and the PEP-II storage ring constitute the "B factory" and are located at the SLAC National Accelerator Laboratory. Figure 2.1 shows an overall view of this facility. PEP-II is an e^+e^- storage ring designed to operate at the $\Upsilon(4S)$ resonance, which corresponds to a center of mass energy of 10.58 GeV, as shown in Figure 2.2. The $\Upsilon(4S)$ resonance is just above the threshold for $B\bar{B}$ production and disintegrates to $B\bar{B}$ pairs more than 96% of the time.

2.1.1 The Concept

The B meson production by the process $e^+e^- \to \Upsilon(4S) \to B\bar{B}$ has the advantage of offering a cleaner environment than the hadronic production processes. The cross sections of the different background processes $e^+e^- \to q\bar{q}$, where $q = u, d, s, c$, and $e^+e^- \to \tau\bar{\tau}$ are shown in Table 2.1 and are of the same order as the cross section of the B meson production process. About 10% of so-called *off-peak data* is taken at an energy 40 MeV/c^2 below the $\Upsilon(4S)$ resonance to study these background processes.

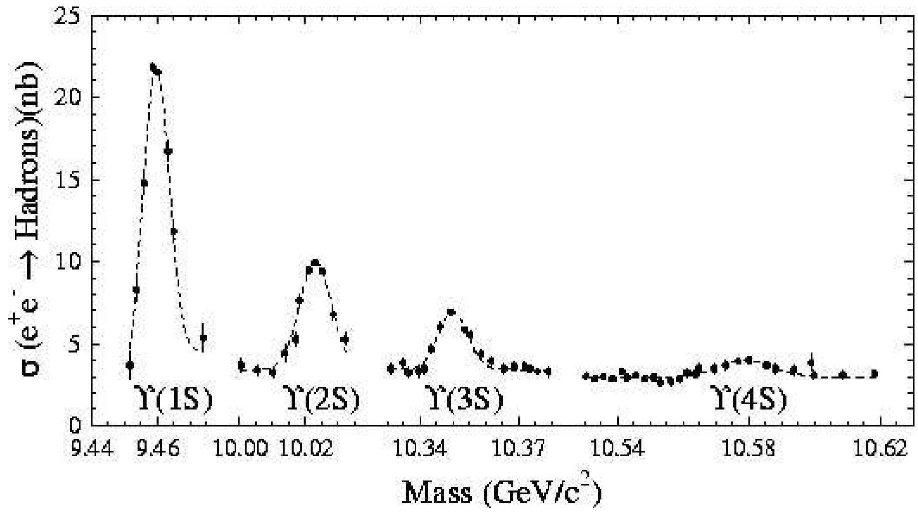

Figure 2.2: Effective cross-section for the production of Υ resonances. PEP-II operates at the $\Upsilon(4S)$ (10.58 GeV/c^2) for on-peak data and slightly under for off-peak (10.54 GeV/c^2).

To measure the time separation Δt between the decays of the two B mesons, we

$e^+e^- \rightarrow$	$b\bar{b}$	$c\bar{c}$	$s\bar{s}$	$u\bar{u}$	$d\bar{d}$	$\tau^+\tau^-$	$\mu^+\mu^-$	e^+e^-
Cross-section (nb)	1.05	1.30	0.35	1.39	0.35	0.94	1.16	~ 40

Table 2.1: Production cross-sections at $\sqrt{s} = 10.58$ GeV. The effective cross-section is given for $e^+e^- \rightarrow e^+e^-$.

reconstruct the vertices of each B meson and convert the distance between them to Δt using the appropriate kinematics, as explained in detail in Chapter 3. In the $\Upsilon(4S)$ reference frame, the B mesons are almost produced at rest, which makes it a challenge to measure the separation accurately. Quantitatively speaking, in the $\Upsilon(4S)$ reference frame, the momentum of each B meson is of the order of $p_B = \sqrt{\frac{s}{4} - m_B^2} \simeq 342$ MeV/c, which leads to a typical flight length of $d_B = \gamma\beta c\tau_B \simeq 30\mu$m, which cannot be separated by the available vertex tracker techniques. One of the key design features, which allows us to solve this issue and enables us to study the time-dependent CP violation, was proposed by Oddone in 1987 [24]. The idea lies in the asymmetry of the PEP-II beam energies, which creates a Lorentz boost $\beta\gamma = 0.56$ of the $\Upsilon(4S)$ system against the laboratory frame, which allows for an increase of the vertices separation (to about 250μm), significant enough to be accessible by the vertex tracker.

2.1.2 The LINAC

The electrons are produced with a polarized electron gun at the end of the LINAC. They are collected into bunches, which are steered through damping rings in order to optimize their shape. They are then accelerated in the 2-mile long LINAC. Some of the electrons are diverted for positron production instead of being injected into the PEP-II storage rings. They are then bombarded on a fixed tungsten target to produce e^+e^- pairs. The resulting positrons are returned to the end of the LINAC to be collected into bunches and accelerated. The electrons and positrons are accelerated in the LINAC to energies of 9.0 Gev and 3.1 GeV, respectively. They are then injected into the high energy e^- (HER) and low energy e^+ (LER) rings of PEP-II.

2.1.3 The PEP-II storage rings

The electrons rotate clockwise in the high energy ring (HER), while the positrons rotate counterclockwise in the low energy ring (LER). The *BABAR* detector is located in the Interaction Region 2 (IR-2), where the two rings cross (see Figure 2.1).

Figure 2.3 shows a horizontal view of IR-2 with the position of the different magnets. The purpose of the quadrupoles QD1-QD5 is to focus the beams. The beams collide head-on at the interaction point (IP) and are then separated by the B1 bending magnets.

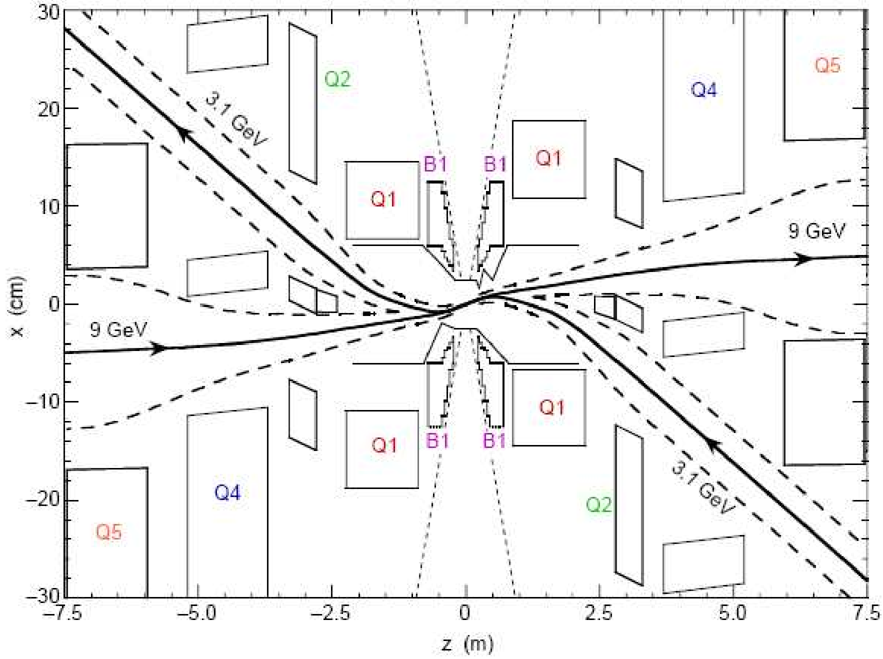

Figure 2.3: Horizontal view of the interaction region. The x scale is 25 times larger than the z scale.

2.1.4 Performance

The PEP-II B-factory has continuously delivered luminosity to the *BABAR* detector from 1999 to 2008, reaching a record-high instantaneous luminosity of $1.21 \times 10^{34} cm^{-2} s^{-2}$. The total delivered and recorded luminosities are shown in Figure 2.4. One can see the different Physics runs, which correspond to different periods of data taking, separated by downtime periods, used for machine developments and repairs. During the final run (Run 7), *BABAR* recorded data at the $\Upsilon(2S)$ and $\Upsilon(3S)$ resonances, and also performed a precision scan of the energy region above the $\Upsilon(4S)$.

The rest of this chapter is dedicated to the *BABAR* detector.

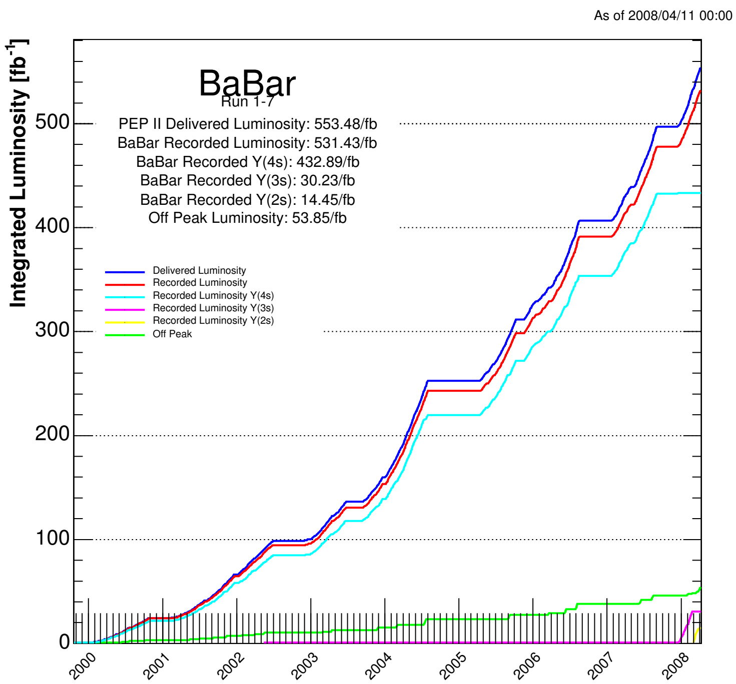

Figure 2.4: Integrated luminosity delivered by PEP-II and recorded by the *BABAR* detector between November 1999 and April 2008. This analysis uses the data taken at the $\Upsilon(4S)$ resonance.

2.2 The *BABAR* Detector

The *BABAR* detector is a standard high energy physics detector and is shown in Figure 2.5. It is constituted of six sub-systems from the IP outwards: a silicon vertex detector (SVT), a drift chamber (DCH), a Cherenkov detector (DIRC), an electromagnetic calorimeter (EMC), a superconducting solenoid producing a 1.5 Tesla magnetic field, and an instrumented flux return (IFR). In an effort to maximize the angular acceptance in the CM frame, the whole detector is offset from the IP by 0.37m in the HER direction and is asymmetric in design.

As shown in Figure 2.5, we use a right-handed coordinate system, with the origin at the IP. The z-axis points horizontally in the direction of the electron beams, while the y-axis points vertically upwards and the x-axis points outward of the PEP-II ring. In the following, we will also use the polar angle θ and azimuthal angle ϕ, defined as in the standard spherical polar coordinate system.

We will present each of the sub-detectors in the following sections. More information can be found in [25].

2.2.1 The Silicon Vertex Tracker (SVT)

The Silicon Vertex Tracker (SVT) is a charged track detector located inside of the 4.5-meter long *BABAR* support tube, very close to the beam pipe. It encompasses about 90% of the solid angle in the center of mass frame. It serves two purposes. It measures the track positions close to the interaction point with high precision. It is also used in association with the drift chamber (described below) to reconstruct the trajectories of charged particles, in particular for tracks with tranverse momentum less than 180 MeV/c. Figures 2.6 and 2.7 show two cross-sectional views of the

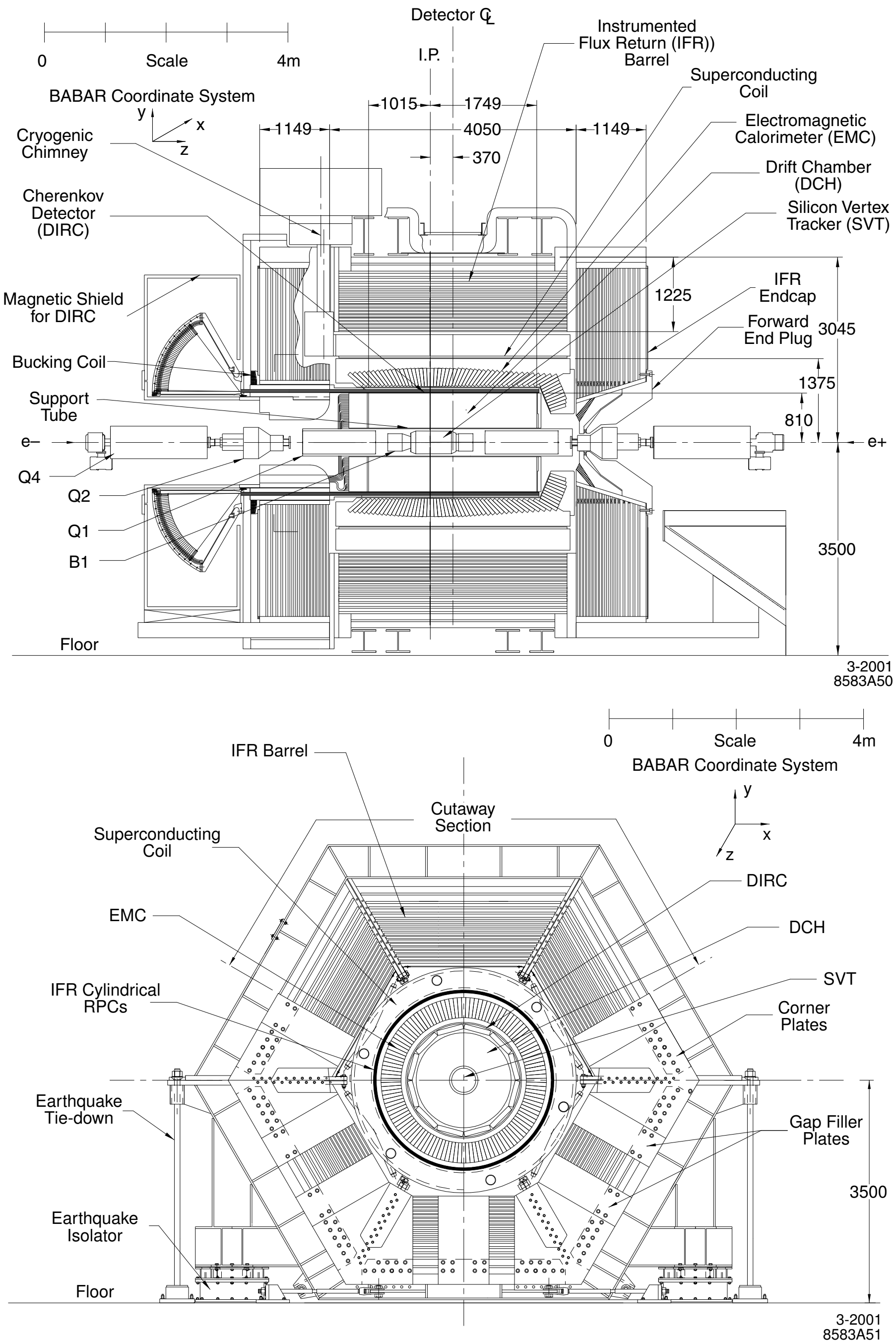

Figure 2.5: Longitudinal (top) and transversal (bottom) cross-sectional view of the *BABAR* detector. From the IP outwards: the SVT, the DCH, the DIRC, the EMC, the superconducting coil and the IFR.

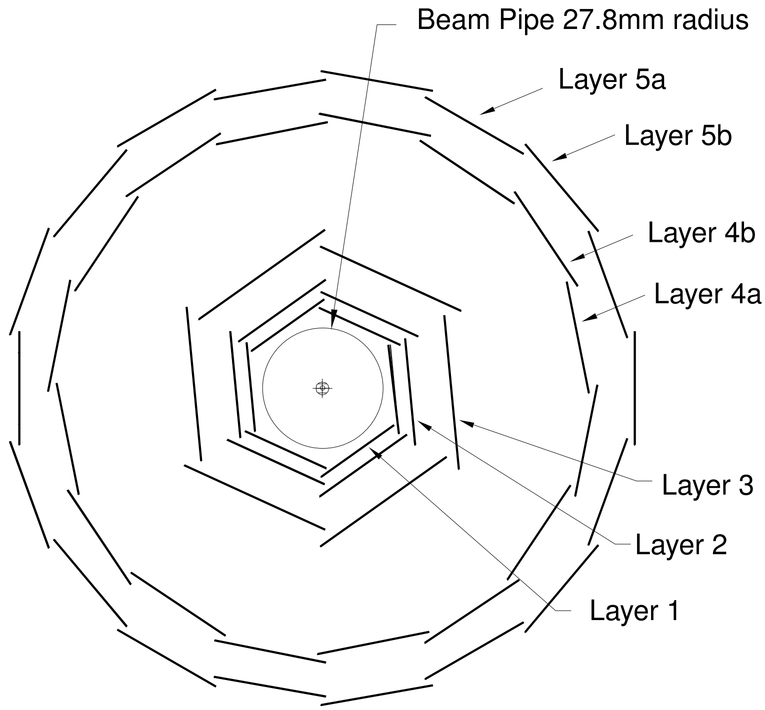

Figure 2.6: Schematic transversal view of the SVT.

SVT. The SVT consists of five cylindrical layers of double sided silicon micro strip detectors. ϕ *stripes* parallel to the z axis are located on the outer sides to allow for a precise ϕ measurement. z *stripes* are aligned perpendicular to the ϕ stripes on the inner sides to measure z precisely.

The resolution in z and ϕ is shown for each layer in Figure 2.8. Layers 1-3 are used in the B vertex reconstruction. This is crucial for the measurement of Δz, the distance between the decay vertices of the two B mesons, and therefore the measurement of sin2β. The resolution of a single vertex is better than 80μm, while the resolution of Δz is less than 130μm.

The SVT is the system which is the closest to the IP and is therefore particularly exposed to radiation. Section 2.4 describes in detail the sensitivity of the SVT to radiation as well as its associated protection system, *SVTRAD*.

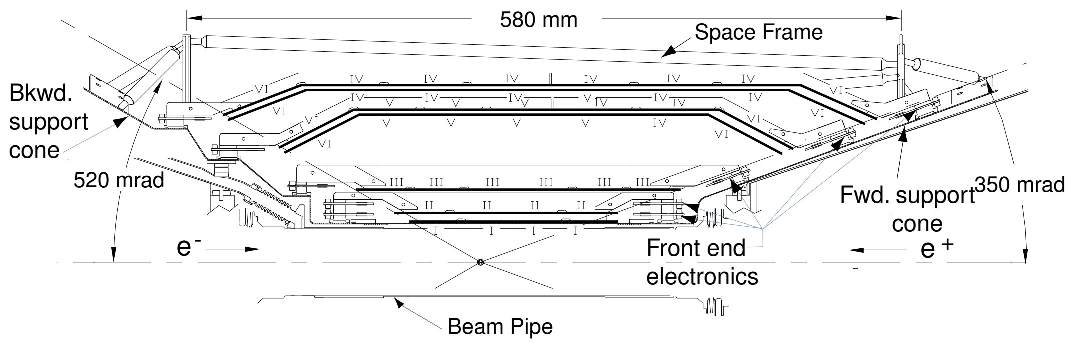

Figure 2.7: Schematic longitudinal view of the SVT.

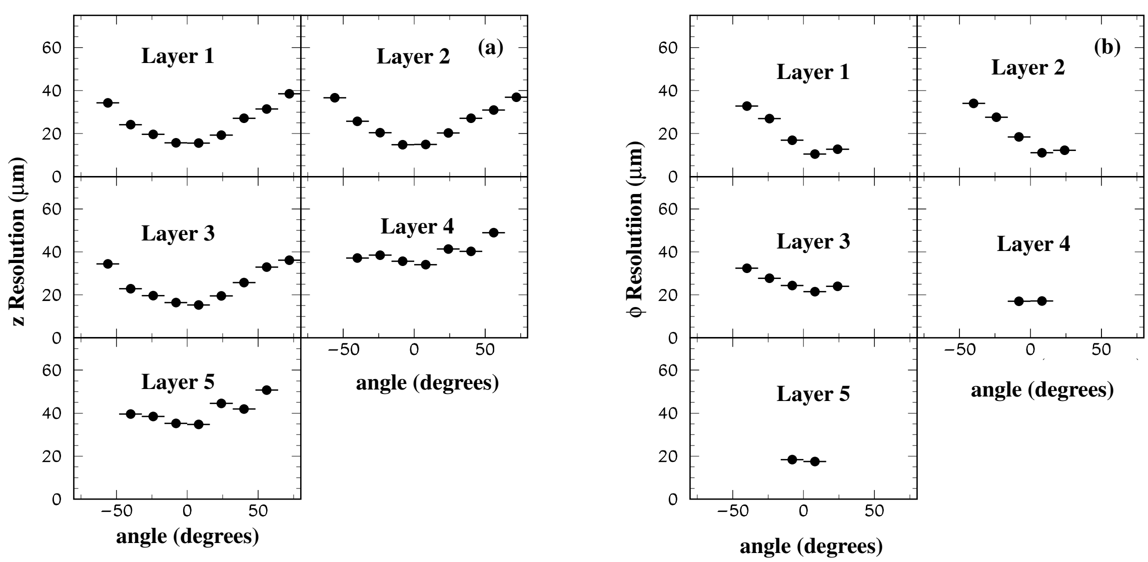

Figure 2.8: z (a) and ϕ (b) resolution as a function of the incidence angle of the track, for each of the five layers.

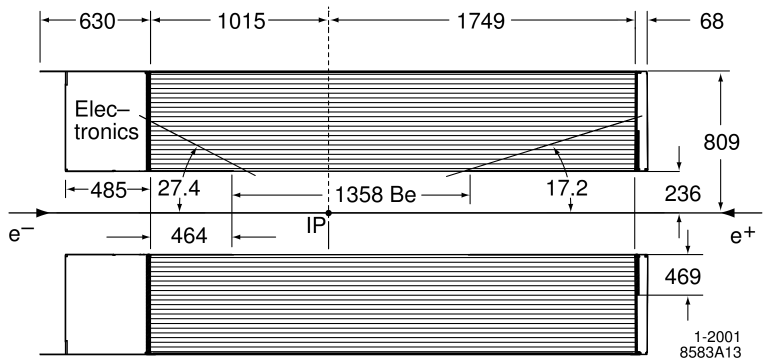

Figure 2.9: Schematic longitudinal view of the DCH. All lengths and angles are given in millimeters and degrees respectively.

2.2.2 The Drift Chamber (DCH)

The Drift Chamber (DCH) gives a precise measurement of the transverse momentum of charged particles. It is the main source of reconstruction information for K_S^0 particles, which is essential for our analysis. Figure 2.9 shows its dimensions. Its asymmetric position with respect to the IP was designed to take into account the boost of the center of mass in the *BABAR* reference frame.

The DCH is filled with a gas mixture of 80% helium and 20% isobutane, in which drift cells are arranged in 40 cylindrical layers. These cells are arranged in ten superlayers of four layers each. Figure 2.10 shows the structure of the superlayers and the cells they are composed of. These superlayers alternate between axial (A), with wires parallel to the z axis, positive stereo angle (U) and negative stereo angle (V) between the wires and the z axis, in the following order : AUVAUVAUVA. This assures an optimal spatial resolution of the trajectory.

A cell consists of a sense wire, made of tungsten-rhenium, surrounded by six field wires made of aluminum. The field wires are grounded while the sense wires are held at an operating voltage of 1930 V. A charged particle traveling through the DCH ionizes the gas molecules along its tracks. This results in electrons drifting to

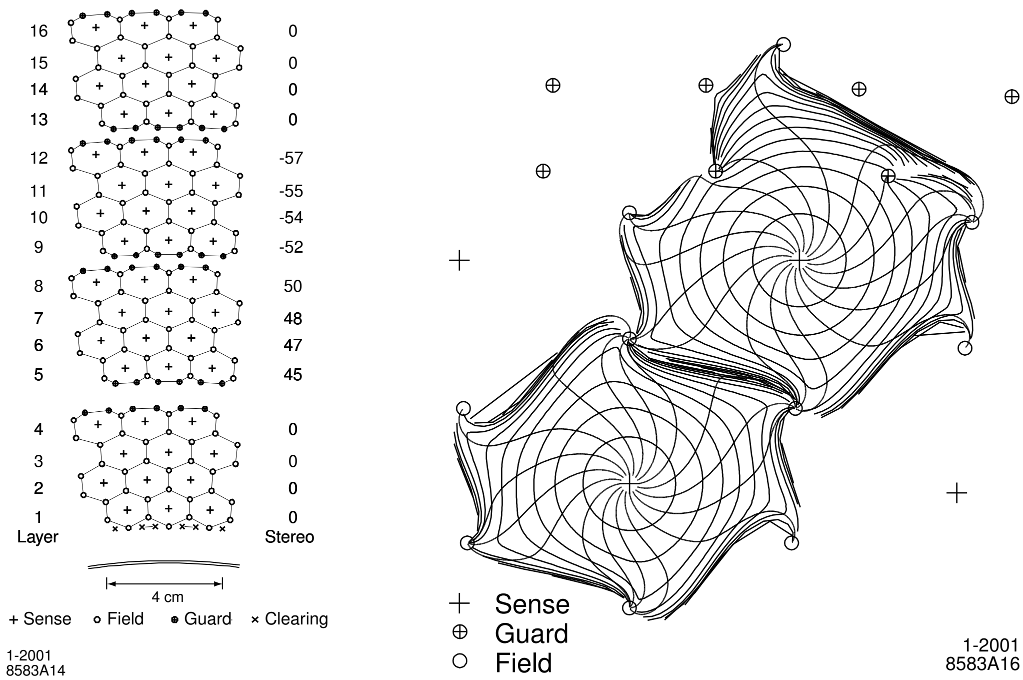

Figure 2.10: Left : Schematic view of the four innermost superlayers of the DCH. The numbers shown on the right give the stereo angles of the wires in mRad for each layer. Right: Drift cell isochrones (equal drift time contours spaced by 100 ns) in cells of layers 3 and 4 of an axial superlayer.

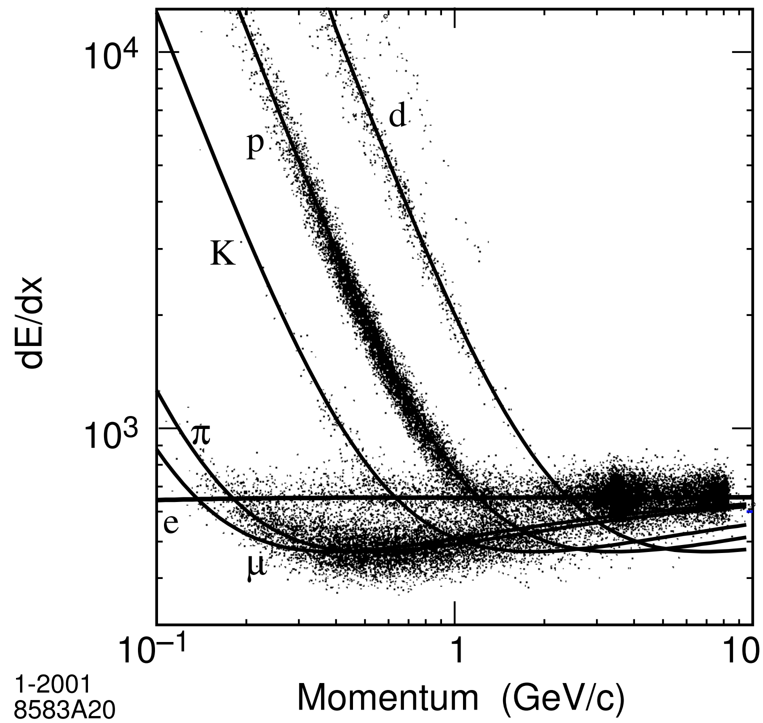

Figure 2.11: dE/dx measured in the DCH for different types of particles. The solid lines show the Bethe-Bloch predictions.

neighboring sense wires, producing a signal in these wires. We call the signal in one cell a *DCH hit* and we group all hits consistent with the trajectory of a particle in a *track*. The radius of this track allows us to reconstruct its transverse momentum and the z information is used to determine the momentum vector. The total charge deposited is also used to determine the charged particle's energy loss dE/dx, which provides the primary input for particle identification (PID), especially for the K/π separation below 700 MeV/c, as seen from Figure 2.11.

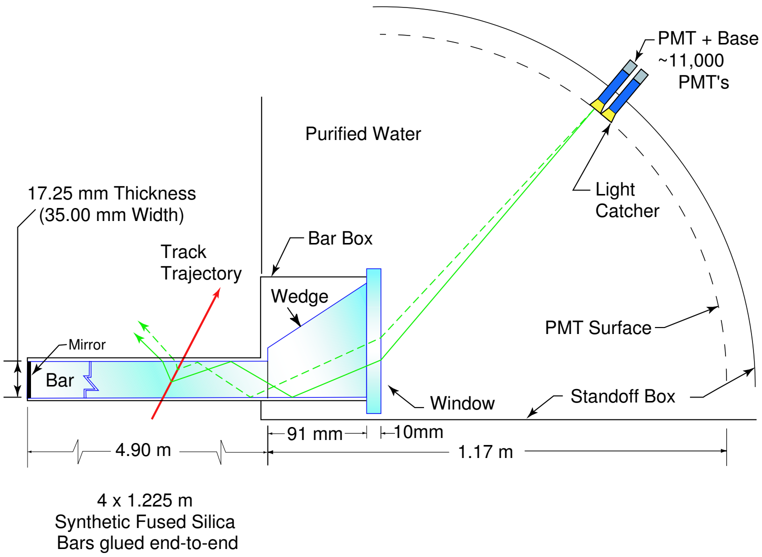

Figure 2.12: Schematic view of the DIRC principle.

2.2.3 The Detector of Internally Reflected Cherenkov Light (DIRC)

The K/π separation in the DCH becomes ineffective for charged particles with momentum above 700MeV/c. We consequently need to turn to a sub-detector dedicated to particle identification at high energies: the Detector of Internally Reflected Cherenkov Light (DIRC) which provides particle identification for tracks with momentum between 0.5 Gev/c and 4.2 Gev/c. The structure of the DIRC is shown in Figure 2.12. It consists of the arrangement of 144 bars of synthetic quartz, grouped in 12 boxes of 12 bars each. These boxes are parallel to the z axis forming a 12-sided barrel around the DCH. This allows for an azimuthal coverage of the bar of 94% (due to the gaps between in each box) and an acceptance of 83% in the polar angle. Figure 2.13 illustrates the DIRC design and principle. A charged particle traveling with a velocity $\beta > \frac{1}{n}$ will produce Cherenkov light, where $n = 1.473$ is the refractive index of the quartz. The Cherenkov photons are emitted in a cone with an opening angle θ_C, where $\cos\theta_C = \frac{1}{n\beta}$. The Cherenkov photons traveling forward are reflected by a mirror and follow the same path as the Cherenkov photons traveling backward which get reflected inside the bars until they enter the standoff box at the end of the detector. This way only the backward end of the DIRC needs to be instrumented. The standoff box is filled with about 6000 liters of purified water, since it has a refractive index very close to that of the quartz, which minimizes total reflection at the junction of the bars and the standoff box. It is also equipped with an array of 10,752 photo multiplier tubes (PMTs) to detect the incoming photons. The expected pattern of the Cherenkov light towards the PMT array can be calculated as a function of the photons arrival time, providing discriminating probabilities for different mass hypothesis. Figure 2.14 shows the separation power of θ_C.

2.2.4 The Electromagnetic Calorimeter (EMC)

The Electromagnetic Calorimeter (EMC) was designed to detect electromagnetic showers with good energy and angular resolution and with excellent efficiency over an energy range from 20 MeV to 9 GeV. It is therefore very important in the reconstruction of modes which include π^0 such as $B^0 \to J/\psi\, K^0_S(\pi^0\pi^0)$ or $B^0 \to J/\psi\, K^*(K^0_S\pi^0)$. In association with the DCH, it is also used for electron identification, which is needed for flavor tagging in time dependent CP asymmetry measurements, such as the one presented in this thesis. It is also essential to detect K^0_L and muons, in combination with the IFR (see section 2.2.5).

The EMC is composed of 6580 crystals made of caesium iodide doped with 0.1% of thallium (CsI(Tl)) arranged in 48 rings of 120 crystals in a barrel and 8 rings of 80 to 120 crystals in a forward endcap, as seen in Figure 2.15. To take into account the boost and prevent shower leakage, we require the crystals located in the forward direction to be longer, i.e. 17.5 radiation lengths or 32.4 cm, while the crystals in the

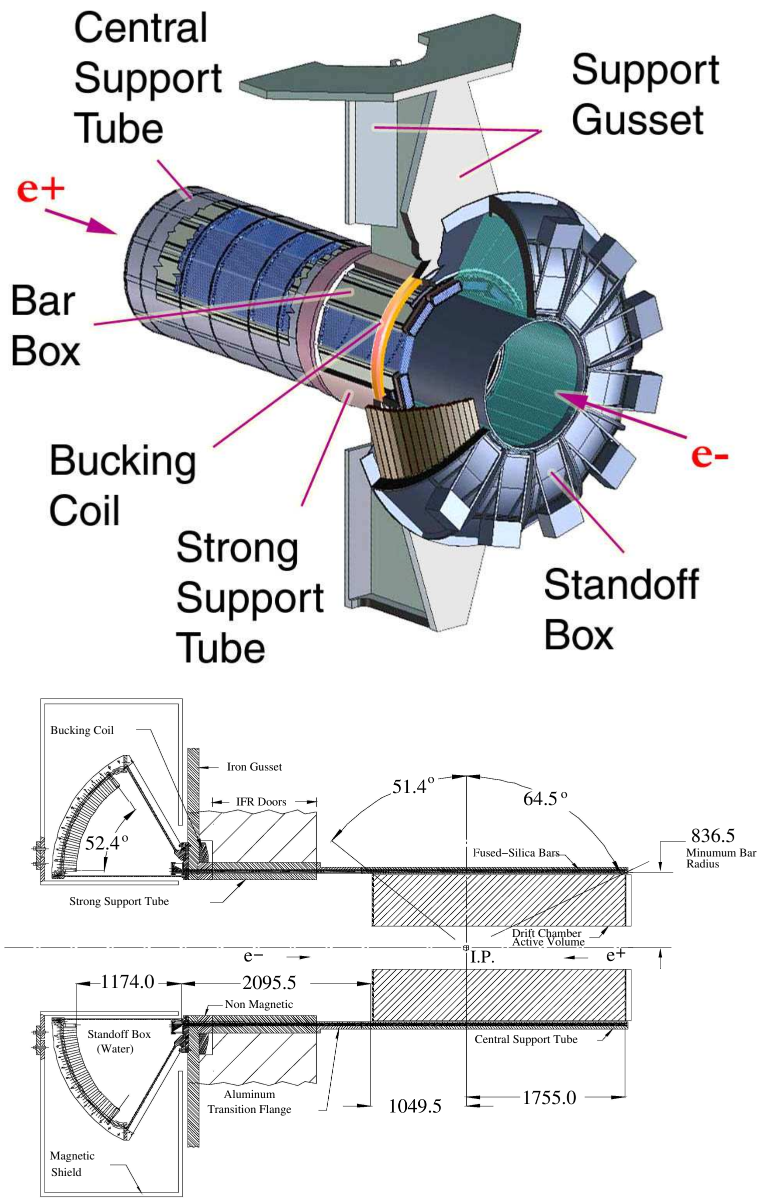

Figure 2.13: Elevation view of the nominal DIRC system geometry. All dimensions are given in millimeters.

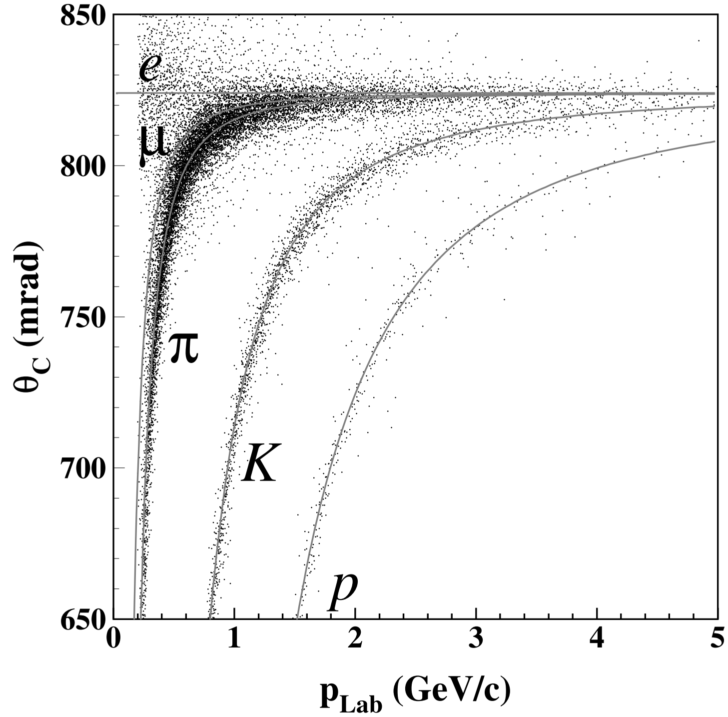

Figure 2.14: The fitted Cherenkov angle of tracks from an inclusive sample of multi-hadron events as a function of the momentum of the tracks.

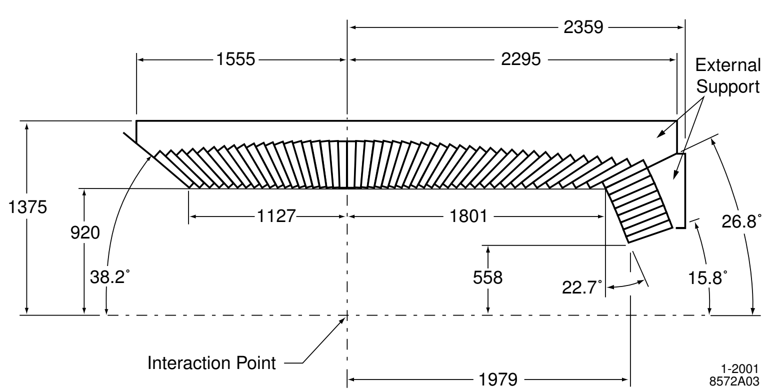

Figure 2.15: Cross-sectional view of the EMC.

backward side have 16 radiation lengths or 29.6 cm. Their transverse cross-section is about 5 cm^2 which is of the order of the Molière radius to achieve good angular resolution at low energies and limit the total number of crystals. An electromagnetic shower is indeed distributed over several crystals and the number of crystals depends on the energy.

Silicon photo-diodes are glued onto the rear side of the crystals to detect the scintillation light emitted by the atomic excitations produced by the moving shower. The reconstruction procedure consists of searching for groups of neighboring crystals called *clusters* where energy was deposited.

2.2.5 The Instrumented Flux Return (IFR)

The Instrumented Flux Return (IFR) is the outermost detector. Its role is to identify muons and neutral hadrons such as K_L^0 mesons. It is therefore essential in the reconstruction of J/ψ mesons which decay to e^+e^- or $\mu^+\mu^-$, and in the flavor tagging of the other B meson. It also acts as a flux return for the 1.5T magnetic field. The IFR, as shown in Figure 2.16, is divided into a barrel and two end doors. Each part is segmented into 18 steel layers separated by 3.2cm-thick gaps. Their thickness varies from 2 cm for the innermost layers to 10 cm for the outermost layers, compromising between muon filtering and hadron absorption. Initially, the gaps of the barrel were instrumented with 19 layers of Resistive Plate Chambers (RPC) in the barrel. 12 of them were replaced with Limited Streamer Tubes (LST) between 2004 and 2006. The end door parts are instrumented with 18 layers of RPCs, resulting in a total of 216 RPC modules.

The RPCs are filled with a gas mixture composed mainly of argon and freon. Two bakelite sheets located on either side of the gas are held at a potential difference of 7

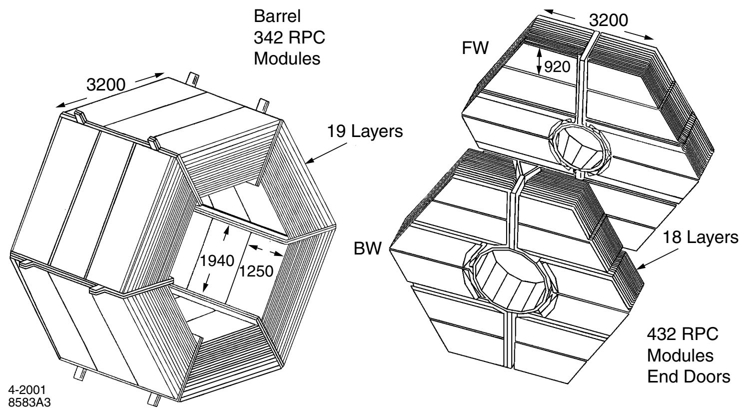

Figure 2.16: Schematic of the three volumes of the IFR. The barrel sector (left) and the forward (FW) and backward (BW) end doors (right). All dimensions are given in millimeters.

kV. A charged particle passing through generates a signal read by electrodes located on each side of it.

LSTs consist of either seven or eight cells filled with carbon dioxide, through which runs a wire held at 5500 V. Similarly to the RPCs, a particle can be detected by ionizing the gas, creating a signal which can be read out from the wire.

2.3 The Trigger

The trigger is designed to select physical events with excellent efficiency, while rejecting background events. Two trigger levels are used:

- The Level 1 hardware trigger retains almost all of the physics events while rejecting background events. It collects information from three sub-systems: the *DCH Trigger* or *DCT* for charged particles, the *EMC Trigger* or *EMT* for neutral particles and the *IFR Trigger* or *IFT* for cosmic rays. A *global trigger* or *GLT* uses the information coming from the first two to try to associate a charged track to a neutral particle and uses the third to put a veto on cosmic events.

- The Level 3 software trigger selects the physics events of interest. It analyzes the data from all the *BABAR* sub-systems.

2.4 SVT Protection System (SVTRAD)

The dependence for the B factory on high energy beams to attain high luminosity is a challenge for the *BABAR* detector because of the radiation generated by the machine backgrounds. Thus, the SVT radiation protective system (SVTRAD) has two objectives:

- measure the radiation dose due to the PEP-II background, which is useful for the SVT, as well as all the other sub-detectors;
- protect the SVT from damage due to radiation. In some particular conditions - such as a vacuum leak - the beam background can become high enough to damage the SVT considerably. It is therefore necessary to have a system that can dump the beams quickly, when necessary.

It is important to find a balance between the need of the experiment to accumulate luminosity at a fast pace and the protection of the SVT against radiation damage. Indeed, the dumping of the beams lowers the efficiency and is followed by injection which increases the radiation level.

In the following section, we will go over the machine backgrounds and the consequent risks for the SVT.

2.4.1 Machine Backgrounds

Machine backgrounds can lead to radiation damage in the detector systems, through short acute doses as well as long term exposure. Under typical conditions, there are three types of backgrounds, which are, in order of increasing importance:

- Synchrotron radiation, generated in the bending magnets and the quadrupole magnets. The geometry of the interaction region and copper masks have reduced it to a very low level.
- Bhabha scattering events due to an electron or positron hitting material close to the IP causing electromagnetic showers (beam instabilities).
- Beam particles interacting with gas molecules in the beam pipe constitute the most significant source of background and can be minimized by keeping a good vacuum in the beam pipe near the IP (Bremstrahlung Coulomb scattering).

These backgrounds can be damaging to the detector and induce high occupancy rates that lead to dead time, and therefore loss of data.

2.4.2 Possible Risks for the SVT

The SVT is the sub-detector which is the closest to the IP and thus it is the most sensitive to radiation damage. The damage due to radiation can have the following consequences:

- an incident particle can change the structure of the silicon crystals, producing free electrons and holes. It can increase the leakage current in the detector

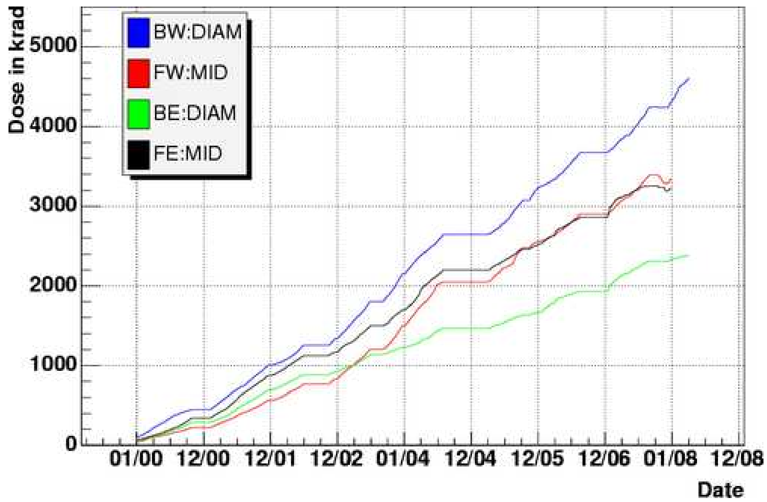

Figure 2.17: Accumulated dose for the diamonds and the diodes on the mid-plane as a function of time.

creating more noise, and change the depletion voltage resulting in different operating conditions and detector resolution.

- the radiation can also affect the electronics.

Quantitative studies on the radiation damage on the SVT have shown that performances would not be affected if the integrated radiation dose does not exceed 5 MRad [26]. This was especially important during the last months of running. The planning had been done based on the assumption that *BABAR* would be running until September 2008, but due to budget constraints the end date was moved up to April 2008. This resulted in some adjustments to allow radiation limits to gradually rise while making sure the SVT was always operational. Figure 2.17 shows the dose accumulated by the diamonds and the diodes in the mid-plane, since the beginning of *BABAR*.

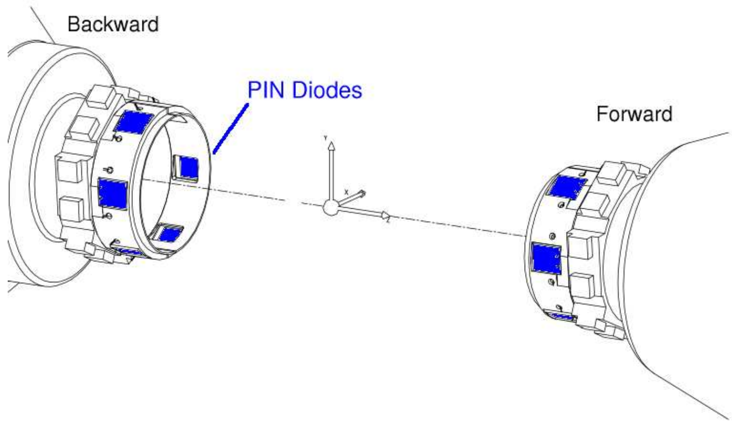

Figure 2.18: The 12 PIN diodes of the SVTRAD system.

2.4.3 Description of the SVTRAD System

A detailed description of the SVTRAD system can be found at [27]. The SVTRAD system is composed of two polycrystalline chemical vapor deposition (pCVD) diamonds and 12 silicon PIN diodes. The diodes were installed in 1999, and the diamonds were later installed in August 2002.

The Diodes

The diodes are located on two rings, which have a 3-cm radius at $z = +12.1$ cm (forward) and -8.5 cm (backward), as shown in Figure 2.18. Each ring consists of six diodes: three diodes on the east (E) side of the detector and three on the west (W) side occupying the top (TOP), middle (MID) and bottom (BTM) planes of the ring. The MID diodes see much higher background than the BTM and TOP diodes. Due to effects of the bending magnets B1, BW:MID is the diode which is most sensitive to the HER and FE:MID is the most sensitive to the LER. The electronhole population follows a Fermi-Dirac distribution. The leakage current of the diodes therefore depends on the temperature and can be written

$$I(T) = I(T_0) \times \left(\frac{T}{T_0}\right)^2 e^{-\frac{E}{k}(\frac{1}{T}-\frac{1}{T_0})}, \tag{2.1}$$

where E is the energy of the band gap for silicon (1.2 eV), T_0 is the reference temperature (20°) and k is the Boltzmann constant. Thermistors are installed next to the diodes in order to keep track of the temperature variations.

The damage due to radiation is another factor which affects the evolution of the leakage current. It increases linearly with the integrated dose.

As a result, the currents measured are dominated by leakage current. In order to extract the doses due to radiation, one has to measure precisely the total leakage current and evaluate the value of the pedestal to be subtracted.

The Diamonds

The two diamonds are located on the backward side, on the MID planes, due to space constraints. They are much more resistant to radiation damage than the silicon diodes. Indeed, the signal of the diamonds is not dominated by the leakage current which remain of the order of a few nA after years of running and a total accumulated dose of a few MRad. The leakage current in the diamonds is also independent of temperature variations.

2.4.4 Protection Algorithms

Electronics Readout

The SVTRAD electronics has two distinct functions: the radiation monitoring and the abort process, which dumps the beams in case the radiation dose is too high. Each SVTRAD board monitors the signal of three diodes and their six thermistors, or the signal of the two diamonds. They communicate via a CAN bus (Controller Area Network) [28] with a real time control software called EPICS (Experimental Physics and Industrial Control System) [29]. This software is used by the other subsystems and PEP-II and provides applications that can be used to treat the data acquired by each board, and control the latter in a UNIX environment.

The Ten-minute Timer

This protection algorithm software works under EPICS to limit the radiation dose received by the SVT in the long term. During normal *BABAR* running conditions, when the dose rate received exceeded 100 mRad/s for more than a minute, an alarm was sent to the beam operators giving them time to react and decrease the background level. If the radiation level remained above the threshold for more than ten minutes, the beams were dumped.

Short Time Abort

Two others types of beam aborts were also in effect. Their goal was to avoid high radiation doses received in a short amount of time. Their logic is electronics based: the signals received from each diode is monitored, while taking into account the temperature dependence of the leakage current of that diode. For type-A aborts, two thresholds are defined:

- d_0 is the threshold at which we start integrating the radiation dose;
- D_0 is the threshold over which the integrated dose is considered too high.

In other words, type-A aborts occur when the dose rate exceeds d_0 and integrates to reach D_0. This is illustrated in Figure 2.19, which shows an example of a type-A abort. The values of d_0 and D_0 during Run 6 are shown in Table 2.2 (see Section 2.4.5). These thresholds allow to have brief bursts without abort. For type-B aborts, the

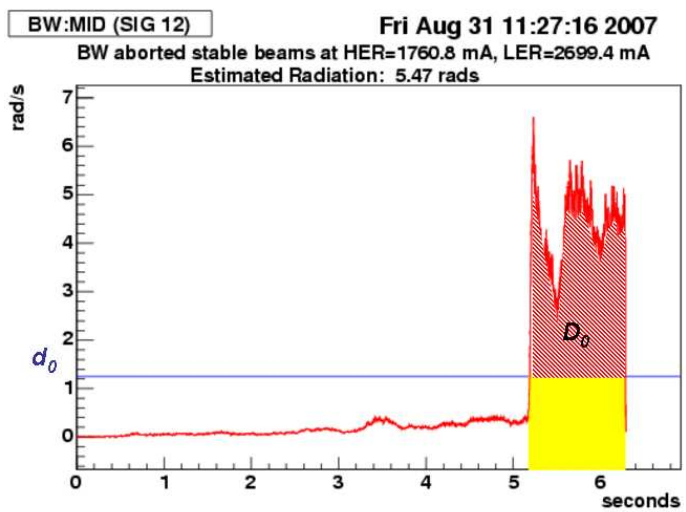

Figure 2.19: Example of radiation dose recorded during a type-A abort.

Diode	d_0 (mRad/s)	D_0 (mRad)
BW	1250	5000
FW	600	5000
BE	700	5000
FE	1000	5000

Table 2.2: Threshold values of the MID plane diodes.

beams are dumped as soon as the dose rate is higher than 400 Rad/s, as shown in

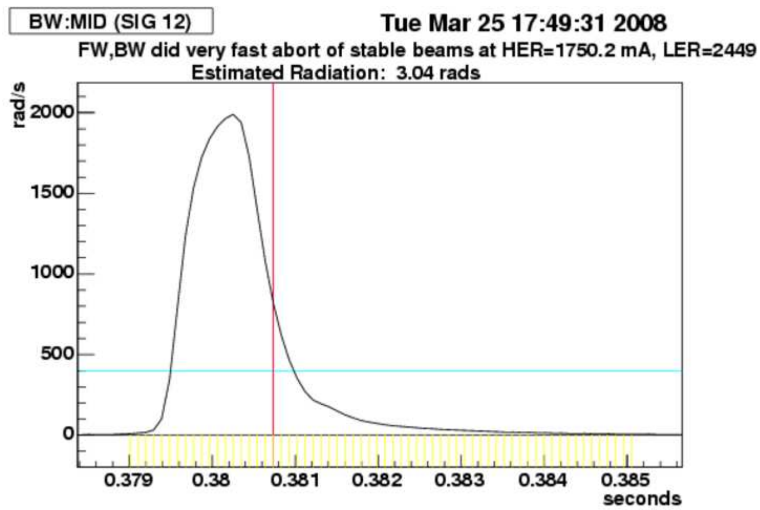

Figure 2.20: Example of radiation dose recorded during a type-B abort.

Figure 2.20. During PEP-II injection, the *BABAR* detector is automatically ramped down and these thresholds can be relaxed.

2.4.5 End of Run Conditions

At the end of 2007, Run 7, which had recently started, had to be shortened due to budget constraints. The radiation budget had to be reevaluated by the SVT and SVTRAD teams. As a consequence, some of the thresholds mentioned above were gradually increased to allow PEP-II to run at higher luminosities and minimize the number of beam aborts. d_0 reached 5000 and 2500 for the BW and FW diodes, respectively. In the meantime, daily checkups were made to make sure the SVT was still running correctly and data quality was not affected.

SVTRAD has been a reliable system which insured that the integrated radiation dose did not exceed the budget over the years of *BABAR* running, guaranteeing the SVT's lifetime and data quality.

2.5 Data Acquisition and Reconstruction

The *BABAR* data acquisition system (DAQ) consists of a chain from the front-end electronics to the logging of the data events. It relies on the following sub-systems:

- The Online Dataflow (ODF), which transports the data from the detector's front-end electronics to be stored;
- The Online Event Processing (OEP), which is responsible for the processing of complete events, including the operations of the L3 trigger algorithm and the data quality monitoring.
- The Logging Manager, which receives the selected events sent from the OEP and writes them to disks for use as input to the Online Prompt Reconstruction (OPR) system.

The volume of recorded data at *BABAR* is of the order of the Petabyte (1 PB = 10^{15} Bytes) and individual members of the collaboration need a centrally managed processing system to analyze the full data sample. The event reconstruction is done in two stages. First, the OPR processing, which is centrally performed, takes place:

- charged tracks and calorimeter clusters are reconstructed from the raw detector hits;
- the information from the tracking system and the DIRC are used to define the particle identification selectors;
- data quality monitoring and rolling calibrations are also performed.

The OPR processing makes use of several large computer farms. The calibrations and data quality monitoring are run within a few hours of the events being logged to disk, while the full reconstruction routines are usually completed within a few days of the events being logged. At the end of this stage the data are stored in an object-oriented database system, the so-called *event store*.

The second part of the reconstruction process consists in combining the information from OPR to form particle candidates from their decay products.

Charged Particle Reconstruction

Charged tracks reconstruction is based on algorithms that use the data from the SVT and DCH. The Level 3 tracks are used as a starting point for the OPR algorithm. The resulting hits are used by a Kalman filter fitter [34] that accounts for the detailed distribution of the material and magnetic field the tracks travel through. Subsequently, DCH hits consistent with these tracks are added and the fit is performed again. All DCH tracks are then extrapolated into the SVT, accounting for the intervening material and magnetic field, and all consistent silicon-strip hits are added to them. The tracks are stored in the event database in different *lists* depending on the quality of the track.

Neutral Particle Reconstruction

The EMC reconstruction algorithms combine crystals into clusters corresponding to individual particle showers. The clusters are formed starting with crystals containing at least 10 MeV. Neighboring crystals are added if their energy is greater than 1 MeV. If it if greater than 3 MeV, their neighbors are also added.

Local maxima or "bumps" within each cluster are then identified, since a cluster may be caused by showers in close proximity or overlapping.

In order to differentiate between charged and neutral particles, all tracks in the event are projected onto the inner face of the calorimeter. If no track intersects any of its crystals, a bump is determined to be neutral.

At this stage, the data sample is available to the whole *BABAR* collaboration and each analyst can study a particular decay sequence, using a series of analysis packages based on a common framework.

This is the object of Chapter 3.

Chapter 3

CP Asymmetry Measurement in $B^0 \to J/\psi\, K^0_L$

In this Chapter, we describe the Physics analysis, the goal os which is to measure the time-dependent CP asymmetry in the $B^0 \to J/\psi\, K^0_L$ decay mode.

I have worked on two iterations of the analysis. The first one used data collected by the *BABAR* detector during the Runs 1 through 5. The corresponding results were published in [10].

The second one, including Run 6, an extra 82×10^6 $B\overline{B}$ decays, has been submitted to Physics Review D [12]. All the results presented here are from the latter and were presented at the 34^{th} International Conference on High Energy Physics 2008 citeref:conferences.

The analysis includes B^0 decays to the final states $J/\psi\, K^0_S$, $J/\psi\, K^0_L$, $\psi(2S)K^0_S$, $\chi_{c1}K^0_S$, $\eta_c K^0_S$, and $J/\psi\, K^{*0}$ ($K^{*0} \to K^0_S\pi^0$).

I was involved with all the aspects of the analysis related to the $B^0 \to J/\psi\, K^0_L$ decay mode.

The measurements are given in terms of S and C. In addition to measuring a combined S and C for the CP modes described above, we measure S and C for each final state (f) individually, for the $J/\psi K^0_S$ mode where we split this into samples with $K^0_S \to \pi^+\pi^-$ and $\pi^0\pi^0$, and for the channel $J/\psi K^0$ (combining the K^0_S and K^0_L final states).

3.1 Data and Monte Carlo samples

3.1.1 Data Events

The data sample, which was used in this analysis, was recorded by the *BABAR* detector between May 1999 and September 2007 (Run 1 through Run 6) and represents 425.7 fb^{-1} of data recorded at the $\Upsilon(4S)$ resonance. The corresponding number of $B\bar{B}$ events is reported to be $(465 \pm 5) \times 10^6$ by `BbkLumi`, which is a bookkeeping utility of the *BABAR* Computing Model 2 (CM2) [30]. It is broken down by run in Table 3.1.

Sample	Integrated Luminosity (fb^{-1})	B counting ($\times 10^6$)
Run 1	20.4	22.4 ± 0.2
Run 2	61.1	67.4 ± 0.7
Run 3	32.3	35.5 ± 0.4
Run 4	100.3	110.4 ± 1.2
Run 5	133.3	147.1 ± 1.6
Run 6	78.4	81.7 ± 0.9
All	425.7	464.6 ± 5.1

Table 3.1: Integrated luminosity and B counting by run, as reported by `BbkLumi` [30].

3.1.2 Monte Carlo Simulation

Monte Carlo (MC) simulation has an important role in all of the analyses performed at *BABAR*. The MC simulated data are generated using full detector simulation, in three steps:

- First is the Physics simulation, handled by the EvtGen package [31], which simulates the decays of B mesons and other particles and resonances. The detail level is very high, permitting effects such as CPV to be included if requested for certain decay modes. JETSET [32] is also used to generate continuum events as well as some B events for which EvtGen does not have an implementation.
- Second is the simulation of the propagation of the particles in the detector material, using the GEANT4 package [33]. It requires a very detailed model of the *BABAR* detector in terms of its geometry as well as its material. The behavior of the particles passing through the detector material is simulated and recorded in the so-called *GHits*.
- Finally, the detector's response to the simulated events is handled by transforming the GHits into realistic detector signals, simulating the detector electronics. Real background events are also used in order to make the simulation more realistic.

The same reconstruction algorithms, which are applied to the actual data, are also applied to the MC simulated data, which can thereby be used in the same way as the real data events.

There are two kinds of MC information. The *truth* side contains the GHits and the complete decay tree, with the four-momentum of all participating particles, as generated by EvtGen. The *reco* side, on the other hand, only contains the information that can be found in the real data events. On top of being able to produce a large MC dataset, which is helpful when developing the analysis strategy, one can look at the truth side and compare the output of different types of decays, such as the signal and the main sources of background.

When creating the MC data sample, one has to make sure that it is systematically consistent with the actual data events. Several cycles of centrally-produced simulated data for *BABAR* have taken place. In this analysis, we use the set of Simulation Production (SP) data called SP9 [1]. We use two classes of MC events. The first one is the signal MC data, which is generated for specific decay modes, which in our case correspond to $\Upsilon(4S) \to B^0\overline{B}^0$ and $B^0 \to J/\psi K^0_L$, where $J/\psi \to e^+e^-, \mu^+\mu^-$. This dataset is needed to study the effects of the reconstruction process on true signal events. The second set of MC events is the filtered generic MC data. It consists of generated B meson pairs decaying to a set of defined final states. As we will see later, more than 90% of the events that pass our selection criteria contain a real J/ψ particle. We therefore use a set of generic MC events, which include a true J/ψ. We will refer to it as *inclusive* J/ψ MC or $B \to J/\psi X$. Looking at the inclusive J/ψ MC data sample is very similar to looking at real data in the sense that we have to search through an array of different processes to identify the events that contain $B^0 \to J/\psi K^0_L$ signal candidates.

Our MC sample consists of about 10 million signal events and about 16 million inclusive J/ψ events. About 46% of the events in the inclusive J/ψ sample correspond to signal events.

[1]For the analysis that led to the result published in [10], using Runs 1 through 5, we used SP8.

3.2 Flavor Tagging

In this analysis, one of the two neutral B mesons from the $\Upsilon(4S)$ is reconstructed exclusively ($B^0 \rightarrow J/\psi\, K^0_L$).

Flavor tagging is a key method in the measurement of time-dependent CP asymmetries. Its goal is to determine whether the above B^0 meson, decaying to a CP final state (B_{rec}), is a B^0 or a $\overline{B}^0$ at $\Delta t = 0$.

This is achieved using the decay products of the recoiling B meson (B_{tag}). After removing all the tracks originating from B_{rec} (the signal events), the remaining tracks are analyzed to determine the flavor of the second B^0 (B_{tag}), in order to"tag" its flavor, i.e. whether it is a B^0 or a $\overline{B}^0$. The latter must therefore decay to a flavor-specific final state.

It is important to determine the flavor of B_{tag} with the highest possible efficiency ϵ_{tag} and the lowest probability ω of assigning the wrong flavor. The discriminating power of our tagging algorithm is quantified using the effective tagging efficiency as a figure of merit

$$Q = \epsilon_{tag}(1 - 2\omega)^2, \tag{3.1}$$

The tagging algorithm at BABAR takes a modular, multivariate approach [38, 10]. It analyzes tracks on the tag side to assign its flavor and associated probability. The flavor of B_{tag} is determined from a combination of nine different tag signatures, such as isolated primary leptons, kaons and pions from B decays to final states containing D^* mesons, and high momentum charged particles from B decays. The properties of those signatures are used as inputs to a single neural network that is trained to assign the correct flavor to B_{tag}. The output of this neural network is then divided into seven mutually-exclusive categories (in order of decreasing signal purity as shown in Table 3.2): Lepton, Kaon I, Kaon II, Kaon-Pion, Pion, Other and Untagged.

The performance of this algorithm is determined using a sample of fully reconstructed B mesons to flavor eigenstates, the so-called B_{flav} sample. The B_{flav} sample consists of B^0 decays to $D^{(*)-}(\pi^+, \rho^+, a_1^+)$ final states. The final state of the B_{flav} sample can be classified as mixed or unmixed depending on whether the reconstructed flavor-eigenstate $B_{\mathrm{rec}} = B_{\mathrm{flav}}$ has the same or opposite flavor as B_{tag}. After taking into account the mistag probability, the decay rate $g_{\pm,B^0}(\Delta t)$ ($g_{\pm,\overline{B}^0}(\Delta t)$) for a neutral B meson decaying to a flavor eigenstate accompanied by a B^0 ($\overline{B}^0$) tag can be expressed as

$$g_{\pm,B^0}(\Delta t) \equiv [(1-\Delta w) \pm (1-2w)\cos(\Delta m_B \Delta t)], \tag{3.2}$$

$$g_{\pm,\overline{B}^0}(\Delta t) \equiv [(1+\Delta w) \pm (1-2w)\cos(\Delta m_B \Delta t)], \tag{3.3}$$

where the $\pm$ sign in the index refers to mixed ($-$) and unmixed ($+$) events, and Δw is the mistag fraction difference between B^0 and $\overline{B}^0$ tagged events.

The performance of the tagging algorithm at *BABAR* is summarized in Table 3.2. The Untagged category of events contain no flavor information. The total effective tagging efficiency at *BABAR* is $(31.2 \pm 0.3\,\%)$.

3.3 $B^0 \to J/\psi\, K_L^0$ Event Selection

The J/ψ mesons are reconstructed from pairs of oppositely charged leptons (l^+l^-), whose selection criteria are explained in section 3.3.1. The K_L^0 is challenging to identify since it is a long-lived ($c\tau > 15$m) and neutral particle. As a result, it does not leave a track in the DCH and interacts hadronically with the detector before decaying. Most of these hadronic showers leave a signal in the EMC and IFR, and the

Table 3.2: Efficiencies ϵ_i, average mistag fractions w_i, mistag fraction differences between B^0 and $\overline{B}^0$ tagged events Δw_i, and effective tagging efficiency Q_i extracted for each tagging category i from the B_{flav} sample.

Category	ε (%)	w (%)	Δw (%)	Q (%)
Lepton	8.96 ± 0.07	2.8 ± 0.3	0.3 ± 0.5	7.98 ± 0.11
Kaon I	10.82 ± 0.07	5.3 ± 0.3	-0.1 ± 0.6	8.65 ± 0.14
Kaon II	17.19 ± 0.09	14.5 ± 0.3	0.4 ± 0.6	8.68 ± 0.17
Kaon-Pion	13.67 ± 0.08	23.3 ± 0.4	-0.7 ± 0.7	3.91 ± 0.12
Pion	14.18 ± 0.08	32.5 ± 0.4	5.1 ± 0.7	1.73 ± 0.09
Other	9.54 ± 0.07	41.5 ± 0.5	3.8 ± 0.8	0.27 ± 0.04
All	74.37 ± 0.10			31.2 ± 0.3

criteria used to select the K_L^0 candidates in each of these sub-detectors are described in section 3.3.2. We reconstruct the $B^0 \to J/\psi K_L^0$ candidates from the identified $J/\psi \to ll$ candidate and K_L^0 candidate pairs. Since we do not have a way to measure the K_L^0 kinetic energy very accurately, we rely on the measurement of its direction to eliminate further background, as will be discussed in section 3.3.3. We use the same selection as the one described in [38].

3.3.1 J/ψ Reconstruction

The J/ψ mesons are reconstructed from pairs of oppositely charged electrons (e^+e^-) or muons ($\mu^+\mu^-$). We impose some general requirements on the J/ψ candidates as well as particle identification criteria on the electrons and muons as described below.

General Requirements

We put a constraint on the J/ψ candidate which requires its daughters to originate from a common vertex. In order to eliminate J/ψ candidates that are not compatible with a $B^0 \to J/\psi K_L^0$ decay, we impose $1.4 < p^* < 2.0$ GeV, where p^* is the J/ψ

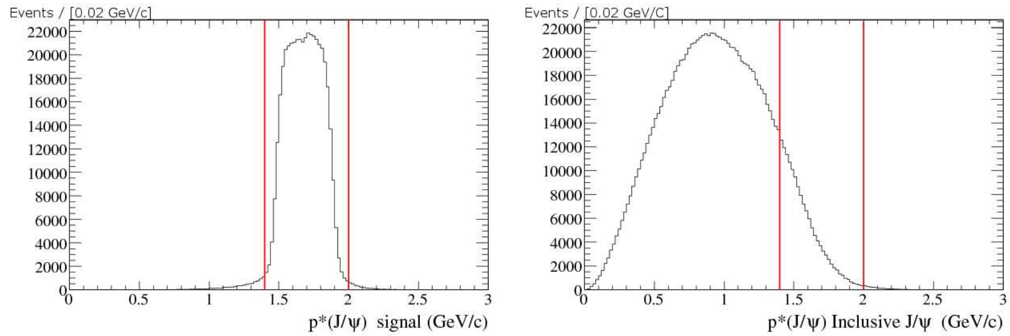

Figure 3.1: p^* distribution from MC signal (left) and inclusive J/ψ (right). The cuts are indicated by red lines.

momentum in the center-of-mass frame. Figure 3.1 shows the p^* MC distribution for signal $B^0 \to J/\psi\, K_L^0$ and for inclusive J/ψ events.

$J/\psi \to e^+e^-$: Electron Identification

The electrons produced by the J/ψ candidate may emit Bremstrahlung radiation, which results in missing energy that we try to recover. In order to do this, we identify neutral clusters with an energy greater than 30 MeV that lie in the same direction as the electron.

To reconstruct $J/\psi \to e^+e^-$ candidates, we combine two Bremsstrahlung recovered tracks and require that they pass two standard electron selectors. We require one of the electrons to pass a likelihood particle identification algorithm. This selector is based on an efficiency cut on the likelihood ratio R,

$$R = \frac{p_e L_e}{p_e L_e + p_\pi L_\pi + p_K L_K + p_p L_p}, \tag{3.4}$$

where p_i is the probability of having an i-track ($i = e, \pi, K$ or p) in the event and L_i is the likelihood of the track to originate from the particle i. The likelihood is a function of following five variables:

- E/p is the ratio of E, the energy deposited in the EMC, and p, the momentum measured in the DCH. We expect this quantity to have a narrow distribution slightly below one, since the electrons that we are interested in are highly relativistic and deposit almost all their energy in the EMC. This is not the case for the other particles we want to discriminate them against.

- The specific energy loss in the DCH, dE/dx, as described in section 2.2.2.

- LAT, or lateral shower shape of the track in the EMC, is given by $LAT = \frac{\sum_{i=3}^{N} E_i r_i^2}{\sum_{i=1}^{N} E_i r_i^2}$, where N, E_i and r_i are the number of crystals associated with the shower, the energy of the i-th crystal and the distance between the centers of that crystal and the cluster, respectively. We use the fact that electrons have a peaking LAT distribution while that distribution is flat for hadrons.

- The longitudinal shape of the shower left by the track in the EMC is used as well by measuring the angle $\Delta\Phi$ between the EMC cluster center and the point of intersection of the track with the EMC. The discriminating power of this variable is due to the fact that the length of the shower is expected to be greater for hadronic showers than electromagnetic showers.

- The Cherenkov angle, θ_C, as described in section 2.2.3.

Some of these variables are shown in Figure 3.2. This selector has a very good electron efficiency and low hadron misidentification rate as can be seen in Figure 3.3. The figures are made available by the BABAR Particle Identification (PID) group [35, 36, 37]. The second electron has to pass looser requirements that include loose cuts on some of the above variables:

- $500 < dE/dx < 1000$ or roughly within $(-3.0\sigma, +7.0\sigma)$ of the expected dE/dx mean,

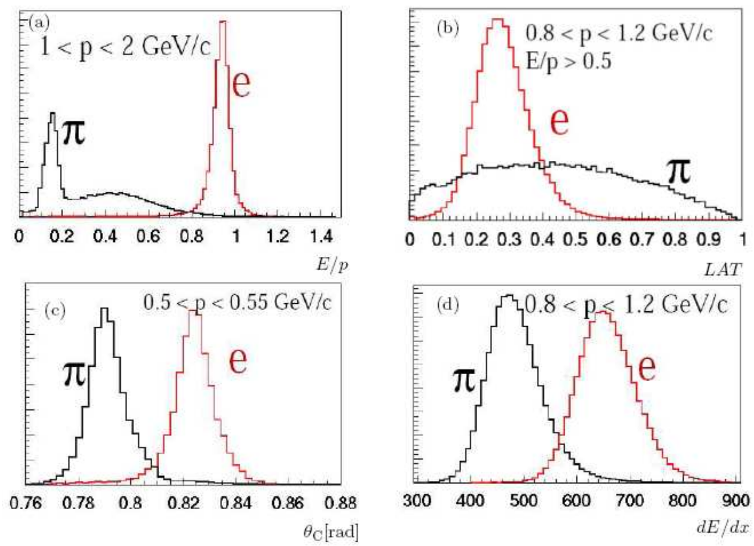

Figure 3.2: Distributions of discriminating variables used in the electron selector, showing their separation power between electron (red) and pions (black). They were obtained using data samples composed of pure electron and pion tracks.

- $0.65 < E/p < 5.0$.

There must also be at least three EMC crystals used to form the cluster.

The vertex constrained mass of the $J/\psi \to ee$ candidate, M_{ee} is shown in Figure 3.4. We require that $3.02 < M_{ee} < 3.14$ GeV. Since electrons may radiate Bremsstrahlung photons, we choose an asymmetric J/ψ mass window in order to accept candidates for which the Bremstrahlung recovery was partial or unsucessful.

$J/\psi \to \mu^+\mu^-$: Muon Identification

Muon identification at BABAR is mainly based on the IFR. A number of variables is used including

- The number of IFR hit layers in a cluster;

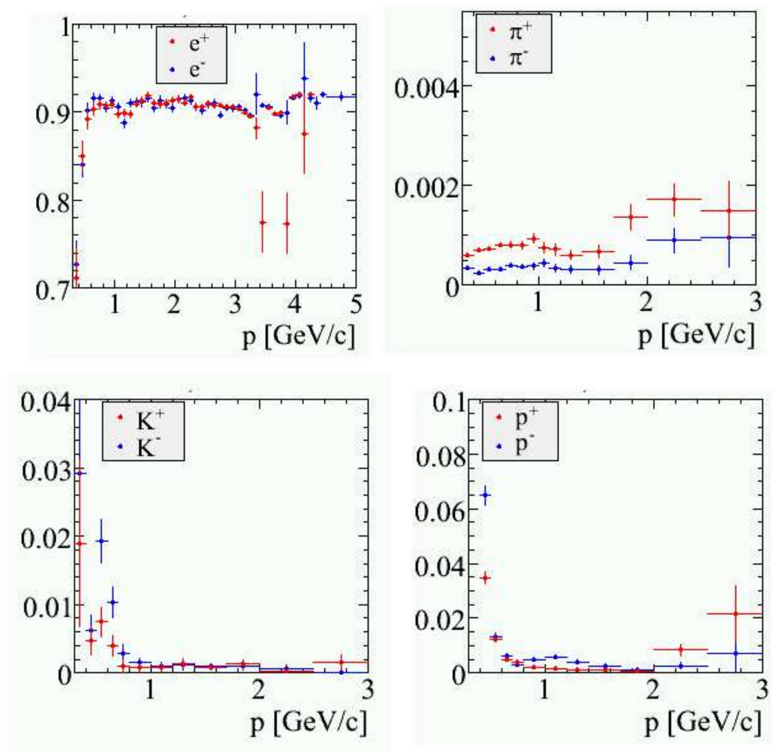

Figure 3.3: Selection rates of the electron selector plotted with respect to the track momentum p. The electron efficiency, as well as the pions, kaons and protons misidentification rates are shown for tracks reaching the backward part of the EMC barrel (similar plots are also available for the forward side). They were obtained using data samples composed of pure tracks of the corresponding particle type.

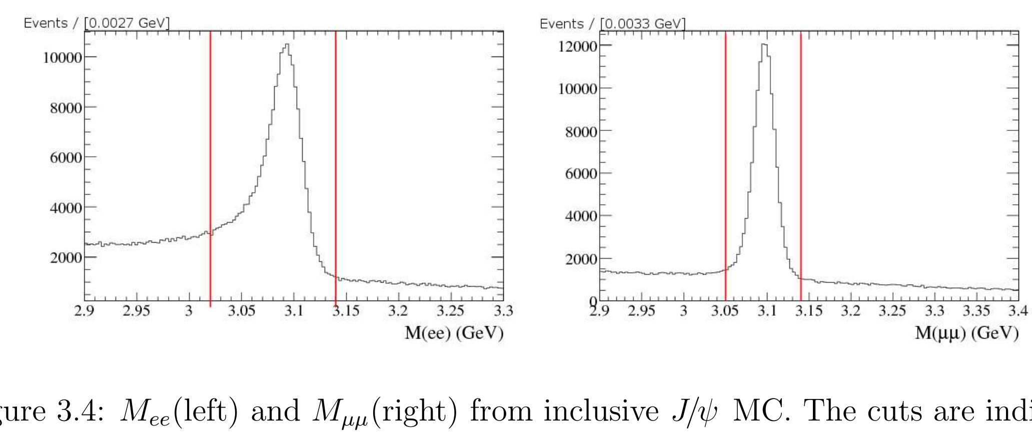

Figure 3.4: M_{ee}(left) and $M_{\mu\mu}$(right) from inclusive J/ψ MC. The cuts are indicated by red lines.

- The energy released in the EMC - all the muons candidates in this analysis should intersect with the EMC and be consistent with an ionizing particle;
- The number of hadronic interaction lengths traversed by the track from the outside radius of the DCH through the IFR, λ_{meas};
- The difference $\Delta\lambda$ between λ_{meas} and the predicted penetration depth for a muon of same momentum and angle;
- The χ^2 for the geometric match between the IFR hit strips and the track extrapolation.

We require one of the daughter muons of the J/ψ to pass the tight level of a neural network selector, which uses these variables as input to a neural network. The muon efficiency of the selector as well as the hadron misidentification rates are shown in Figure 3.5. The second one is required to pass a loose cut-based selector using the same variables.

As with M_{ee}, the vertex constrained mass of the $J/\psi \rightarrow \mu\mu$ candidate, $M_{\mu\mu}$ is shown in Figure 3.4. We require that $3.05 < M_{\mu\mu} < 3.14$ GeV.

J/ψ Sideband

Events from the J/ψ di-lepton invariant mass sideband are used to determine the properties of the non-J/ψ background. The sideband is defined as

- $J/\psi \rightarrow \mu^+\mu^-$; $2.90 < M(\mu\mu) < 3.00$ GeV and $3.175 < M(\mu\mu) < 3.50$ GeV
- $J/\psi \rightarrow e^+e^-$; $3.175 < M(ee) < 3.50$ GeV.

The sideband events are required to pass all other event selection criteria.

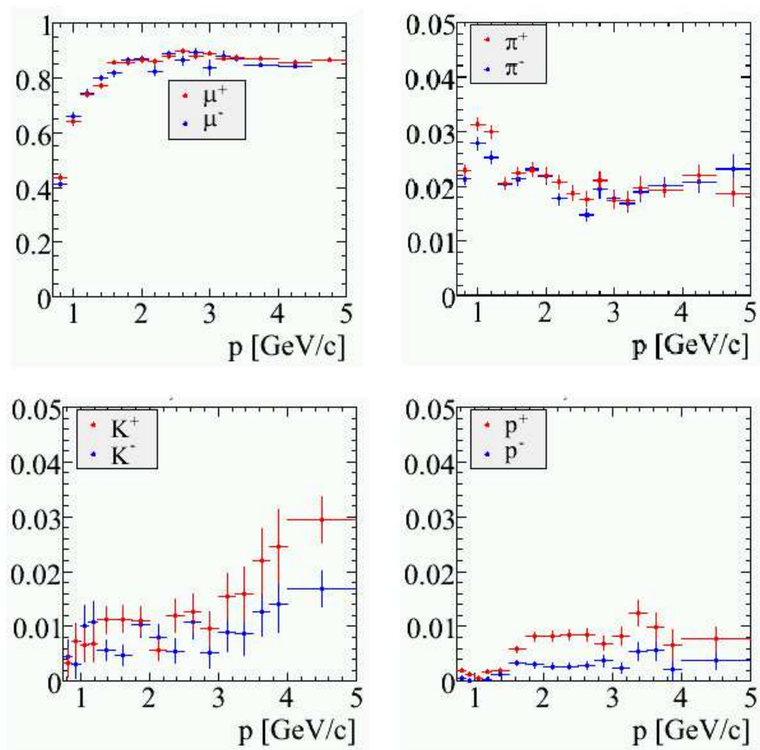

Figure 3.5: Selection rates of the muon selector plotted with respect to the track momentum p. The muon efficiency, as well as the pions, kaons and protons misidentification rates are shown for tracks reaching the forward part of the IFR (similar plots are also available for the barrel and the backward side). They were obtained using data samples composed of pure tracks of the corresponding particle type.

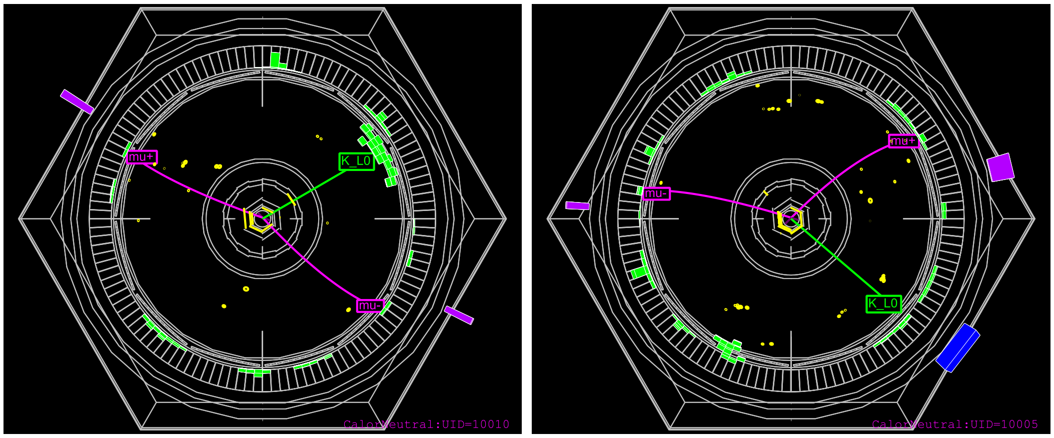

Figure 3.6: Examples of event displays showing K_L^0 producing hits in the EMC only (left) and in the IFR (right). They are shown in a fisheye projection, using the HepRApp software [39].

3.3.2 K_L^0 Reconstruction

As previously mentioned, K_L^0 reconstruction is difficult because of the hadronic interactions that the K_L^0 undergoes in the detector before decaying. The energy of the K_L^0 is not well measured by the EMC or the IFR, therefore we only require that it passes minimal selection criteria. The K_L^0 candidate must be reconstructed as a neutral particle, i.e. a cluster in the EMC or IFR which is not associated with any charged track in the event (see Section 2.5). We also require detector-specific selection criteria.

MC studies show that about 20% and 30% of the K_L^0 produce hits in the EMC only and IFR only, respectively. About a half of them produce hits in both the EMC and the IFR. We show examples of K_L^0 detection in $B^0 \to J/\psi K_L^0$ events in Figure 3.6.

K_L^0 from the EMC

The selection of K_L^0 in the EMC is discussed in detail in [40]. Figure 3.7 shows the distribution of the energy deposited by K_L^0 in the EMC for signal $B^0 \to J/\psi K_L^0$

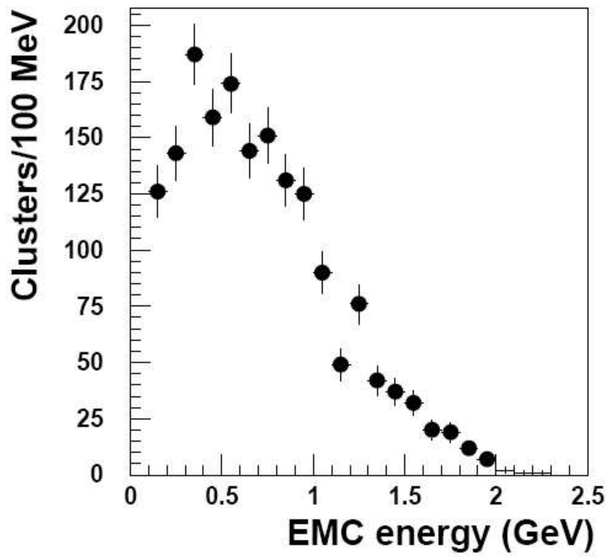

Figure 3.7: Distribution of the energy deposited by K_L^0 candidates in the EMC on a sample of MC signal events.

MC events. The K_L^0 candidates are required to have a cluster energy of at least 200 MeV and less than 2 GeV. The track reconstruction efficiency falls in the very forward region of the detector, we therefore impose that the polar angle θ of the cluster satisfy $\cos\theta < 0.935$.

The rejection of photons from π^0 decays must be given special care. K_L^0 candidates, which are consistent with a photon, are paired with other neutral clusters, where energy deposited in the EMC is greater than 100 MeV. The candidate is rejected if the combined mass of the pair is such that $100 < m(\gamma\gamma) < 150$ MeV/c^2. We also require that clusters with two bumps more than 1 GeV be rejected if the bump energies as well as the shower shapes are consistent with two photons from a π^0.

Isolated clusters that may have been produced by charged hadrons are removed, using a clustering algorithm requiring a minimum separation of 20 cm between clusters.

K_L^0 from the IFR

The IFR candidates are defined as clusters with hits in at least two layers. For similar reasons as the ones invoked in the previous paragraph, we require that the polar angle θ of the IFR cluster satisfies $-0.75 < \cos\theta < 0.935$.

Some hits from charged tracks may be missed by the tracking algorithm due to the irregularity of the hadronic showers. To remedy this, we reject K_L^0 candidates that lie within ± 350 mrad in polar angle, and in the range -750(-300) to +300(+750) mrad in azimuth of the EMC intersection of a positively (negatively) charged track in the event.

3.3.3 $B^0 \to J/\psi\, K_L^0$ Reconstruction

The pairs of $J/\psi \to ll$ and K_L^0 candidates described above are considered as potential $B^0 \to J/\psi\, K_L^0$ candidates. We improve the resolution of the measurement by refitting the momenta of the lepton tracks to constrain the mass of the $J/\psi \to ll$ candidate to the world average [14].

In order to calculate the momentum of the K_L^0, one has to combine the result of the mass-constrained fit of the J/ψ candidate and the measured flight direction of the K_L^0 determined from the EMC and IFR clusters to constrain the invariant mass of the $J/\psi + K_L^0$ system to the world average mass of the B^0 meson [14]. We can then define a quantity which has a high discriminating power against the background in this system: the difference between the calculated $B^0 \to J/\psi\, K_L^0$ candidate energy $E^*_{B^0}$ and the beam energy $E^*_{beam} = \frac{1}{2}\sqrt{s}$ in the center-of-mass (CM) frame

$$\Delta E \equiv E^*_{B^0} - E^*_{beam}. \tag{3.5}$$

We expect this quantity to be null for $B^0 \to J/\psi\, K_L^0$ signal events within experimental resolution and we only accept candidates with $|\Delta E| < 80$ MeV. The ΔE distributions are studied in detail later in section 3.4 and 3.8.1.

Decay Angle Requirements

In order to reduce our background, we take into consideration two decay angles:

- The angle between the $J/\psi\, K_L^0$ candidate and the z-axis, in the CM frame, θ_B. Since this angle has a $\sin^2\theta_B$ distrbibution in B^0 meson decays, we require that $|\cos\theta_B| < 0.9$.
- The angle between one of the legs of the $J/\psi \to ll$ in the rest frame of the J/ψ, and the J/ψ flight direction, $\theta_{helicity}$. Likewise, this angle has a $\sin^2\theta_B$ distribution for all pseudoscalar to vector pseudoscalar decays, such as $B^0 \to J/\psi\, K_L^0$ and we require that $|\cos\theta_{helicity}| < 0.9$.
- Background rejection is improved if we use a simultaneous cut on these variables $|\cos\theta_B| + |\cos\theta_{helicity}| < 1.3$.

These cuts are shown in Figure 3.8.

Missing Momentum Requirement

Since the K_L^0 energy and therefore its momentum are not well measured by the *BABAR* detector, it is interesting to look at the *missing* transverse momentum in the event. The missing momentum corresponds to the momentum of all charged tracks and EMC clusters, except for the K_L^0, projected along the flight direction of the K_L^0 candidate.

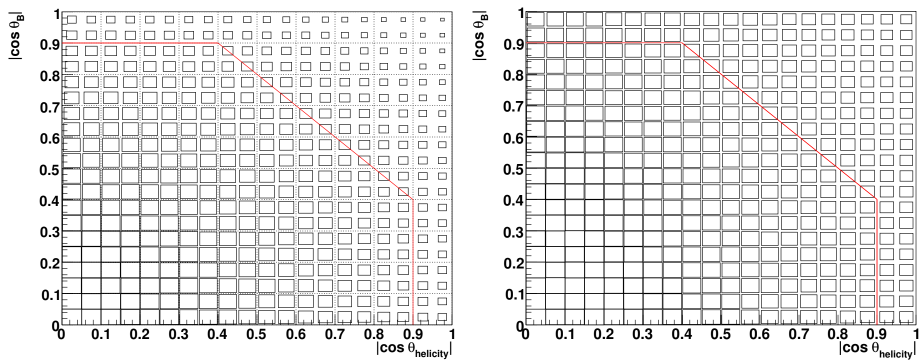

Figure 3.8: Distributions of $|\cos\theta_B|$ versus $|\cos\theta_{helicity}|$ in MC signal (left) and inclusive J/ψ (right). The cuts are indicated by red lines.

We require that the transverse missing momentum be consistent with the K_L^0 momentum of the $B^0 \to J/\psi\, K_L^0$ candidate, i.e. it must be no more than 0.25 GeV/c and 0.40 GeV/c lower than the expected K_L^0 transverse momentum for candidates reconstructed in the EMC and IFR, respectively.

Veto of Similar B^0 Decays

We explicitly remove the following fully reconstructed B mesons events:

- $B^0 \to J/\psi\, K_S^0$, with $K_S^0 \to \pi^+\pi^-$ or $\pi^0\pi^0$;
- $B^0 \to J/\psi\, K^{*0}$, with $K^{*0} \to K^\pm\pi^\mp$ or $K_S^0\pi^0$;
- $B^\pm \to J/\psi\, K^\pm$;
- $B^\pm \to J/\psi\, K^{*\pm}$, with $K^{*\pm} \to K_S^0\pi^\pm$ or $K^\pm\pi^0$.

Since the J/ψ in these decays has a momentum that lies in the accepted range of the $B^0 \to J/\psi\, K_L^0$ decay, they are more likely to form a false signal candidate from a real J/ψ and random EMC and IFR clusters.

Multiple Candidates per Event

In the event that more than one $B^0 \to J/\psi\, K_L^0$ candidates passes the above requirements, we select the best one according to the following :

- If we find multiple B candidates with K_L^0 reconstructed in the EMC, we select the candidate that has the EMC cluster with the highest energy.
- If we find multiple B candidates with K_L^0 reconstructed in the IFR, we select the candidate that has the IFR cluster with the largest number of layers.
- If an EMC and an IFR candidate are selected:
  - if $\cos\theta < 0.9$, where θ is the opening angle between the two candidates, we keep the EMC candidate, since the EMC has a better K_L^0 direction resolution than the IFR.
  - otherwise, we use the EMC kinematic information, but include the event with the other IFR candidates, since they have a similar signal purity.

3.4 Event Yield Determination : the ΔE fit

A binned maximum likelihood fit of the ΔE spectrum in data is performed to determine the relative amounts of signal, inclusive-J/ψ background, and non-J/ψ background. The likelihood function is given by

$$\mathcal{L}(N_{J/\psi\, K_L^0}, N_{J/\psi\, X}, N_{non-J/\psi}) = \sum_{i=1}^{n} \frac{\mu_i^{N_i} e^{-\mu_i}}{N_i!} \times \frac{1}{\sqrt{2\pi(\sigma^2 + N_{non-J/\psi})}} e^{-\frac{(N_{non-J/\psi} - N^0_{non-J/\psi})^2}{2(\sigma^2 + N_{non-J/\psi})}}, \tag{3.6}$$

where:

n is the number of bins used in the fit;

$N_{J/\psi\, K_L^0}, N_{J/\psi\, X}, N_{non-J/\psi}$ are extracted from the likelihood fit and represent the numbers of reconstructed $B^0 \to J/\psi\, K_L^0$, inclusive J/ψ background and background events without a J/ψ, respectively;

μ_i is the expected total number of events in the ith bin;

N_i is the number of reconstructed data events in the ith bin;

$N^0_{non-J/\psi}$ is the expected number of non-J/ψ background events determined using the J/ψ sideband data;

σ is the uncertainty of the value of $N^0_{non-J/\psi}$.

The signal and inclusive-J/ψ distributions are obtained from Monte Carlo, while the non-ψ distribution is determined from an Argus fit [41] to the J/ψ mass sideband region (see Section 3.3.1). The fit to the Argus function is performed because of the lower statistics in the sideband sample.

ΔE: MC Corrections

The event yield calculation relies strongly on the ability of the MC to reproduce the behavior of data. Unfortunately, some variations on the beam parameters that can affect the ΔE resolution and mean are not included in the MC simulation. We need to correct for these effects in order to obtain agreement between the MC and data samples. This can be done by studying a sample of J/ψ K_S^0 events where the K_S^0 is reconstructed as a K_L^0. The advantage of using K_S^0's here, is that their direction is well measured and can be used in the calculation of ΔE along with the B^0 mass constraint. In turn, the ΔE resolution in this sample reflects the uncertainty in

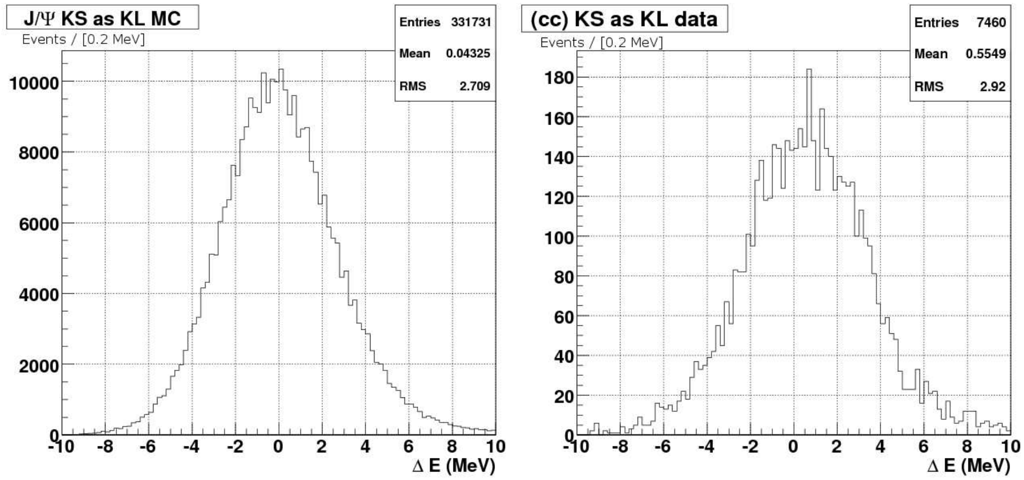

Figure 3.9: ΔE distributions for Monte Carlo (left) and data (right) charmonium K_S^0 events where ΔE was computed in the same way as for $J/\psi\ K_L^0$, using a B^0 mass constraint and the K_S^0 direction only.

the beam parameters to a good approximation. The ΔE distributions for MC and data are shown in Figure 3.9 and we find that we need to shift the MC distribution by 0.5MeV in order to be consistent with the data distribution. We also need to compensate for the beam energy smear which is underestimated. This is done by adding an additional Gaussian with a width of 1.1MeV.

ΔE Fit Method

The binned likelihood fit was executed separately for the EMC and the IFR event samples, due to their differences in purity and background composition, which depend on the K_L reconstruction type. Further, we split the ΔE fit according to J/ψ lepton type in the decay to account for the difference of muon and electron contributions to the non-J/ψ background.

In order to counter the loss of statistics when splitting the data sample in $J/\psi \rightarrow ee$ and $J/\psi \rightarrow \mu\mu$, the fits are done simultaneously, and their ratio of $J/\psi K_L^0$ events to inclusive J/ψ events is constrained to be equal within the precision of the Monte Carlo. Using inclusive-J/ψ Monte Carlo events, we obtain a ratio of :

$$\frac{\frac{\text{Fraction of } J/\psi K_L^0}{\text{Fraction of inclusive } J/\psi}\ (J/\psi \to ee)}{\frac{\text{Fraction of } J/\psi K_L^0}{\text{Fraction of inclusive } J/\psi}\ (J/\psi \to \mu\mu)} = 1.011 \pm 0.007 \tag{3.7}$$

Results of the ΔE Fit

The results of the ΔE fits for all the data events are shown in Figure 3.10 for the EMC and for the IFR. In Appendix B, we present all the fits split by tagging category. The numerical results of the ΔE fits are given in Tables 3.3 and 3.4 for all events and for the flavor tagged events only, respectively. Table 3.7 shows the results for the

EMC K_L^0				
	ΔE Fit $J/\psi \to ee$		ΔE Fit $J/\psi \to \mu\mu$	
	Events	Fraction	Events	Fraction
Signal	1353 ± 49	29.9 ± 1.0	1499 ± 50	24.7 ± 0.8
J/ψ-X	2345 ± 69	51.8 ± 1.2	2621 ± 84	43.2 ± 1.1
non-J/ψ	831 ± 35	18.3 ± 0.8	1953 ± 45	32.2 ± 0.8
IFR K_L^0				
	ΔE Fit $J/\psi \to ee$		ΔE Fit $J/\psi \to \mu\mu$	
	Events	Fraction	Events	Fraction
Signal	1025 ± 43	49.4 ± 1.7	1149 ± 44	44.9 ± 1.5
J/ψ-X	821 ± 44	39.6 ± 1.9	931 ± 53	36.4 ± 1.8
non-J/ψ	228 ± 18	11.0 ± 0.9	480 ± 23	18.8 ± 1.0

Table 3.3: Results of binned ΔE fit for all events. The fractions and yields are for the range $|\Delta E| < 80$ MeV.

flavor tagged events by runs. Tables 3.5 and 3.6 correspond to the fractions obtained from the ΔE fits performed separately for EMC and IFR K_L^0 and split by tagging category.

The efficiency by run is also shown in Table 3.8.

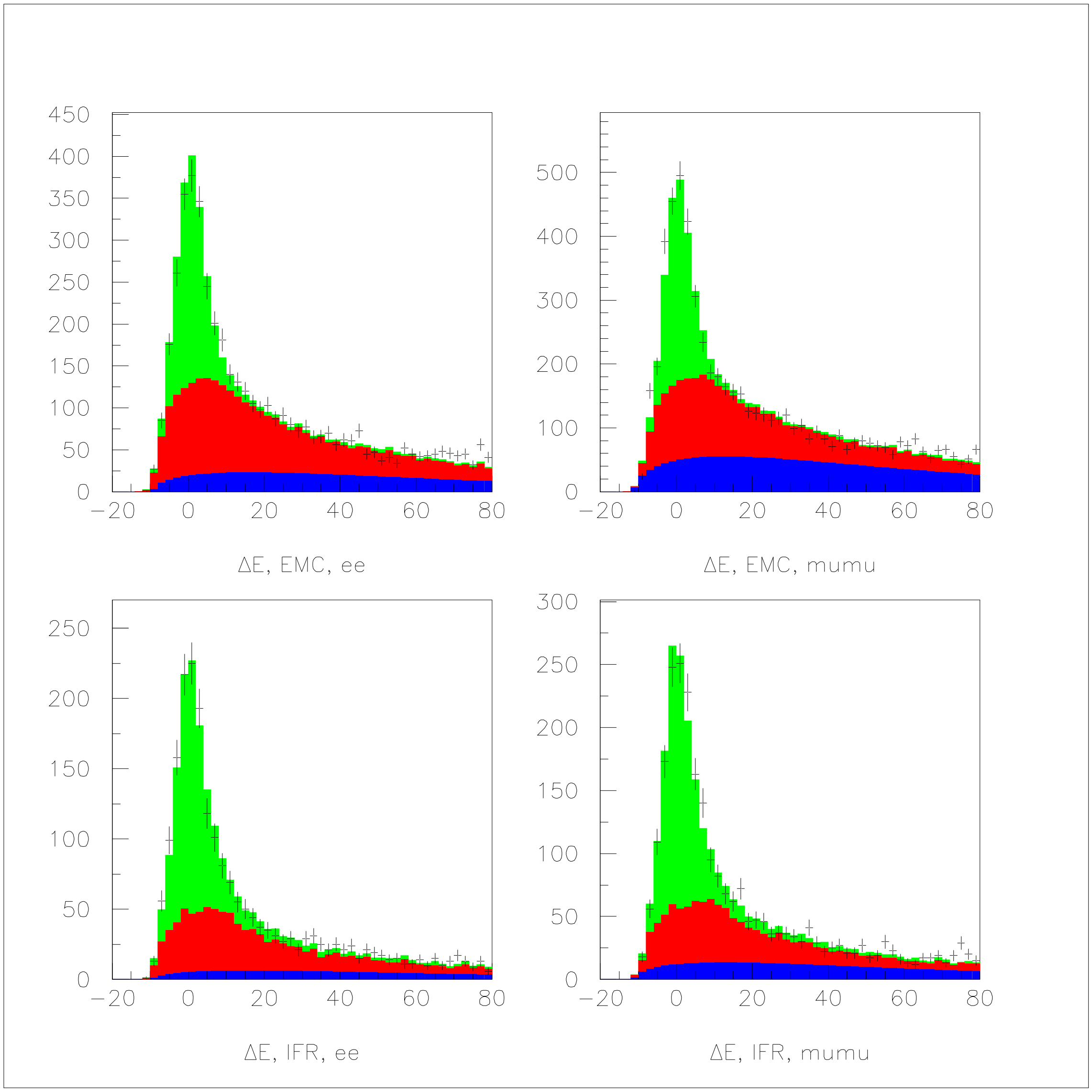

Figure 3.10: Fit of the ΔE spectrum in the data for EMC K_L^0 events (upper plots) and for the IFR K_L^0 events (bottom plots). The blue (dark) distribution is the non-J/ψ component, which was fit to an Argus function. The red (medium) component is inclusive-J/ψ background from Monte Carlo and the green (light) component is signal, also from Monte Carlo.

EMC K_L^0				
	ΔE Fit $J/\psi \to ee$		ΔE Fit $J/\psi \to \mu\mu$	
	Events	Fraction	Events	Fraction
Signal	996 ± 42	29.6 ± 1.1	1113 ± 43	24.9 ± 0.9
J/ψ-X	1762 ± 59	52.3 ± 1.4	1988 ± 72	44.4 ± 1.3
non-J/ψ	609 ± 30	18.1 ± 0.9	1376 ± 38	30.7 ± 0.9

IFR K_L^0				
	ΔE Fit $J/\psi \to ee$		ΔE Fit $J/\psi \to \mu\mu$	
	Events	Fraction	Events	Fraction
Signal	735 ± 37	47.8 ± 2.0	826 ± 37	44.0 ± 1.8
J/ψ-X	638 ± 37	41.5 ± 2.2	724 ± 46	38.6 ± 2.1
non-J/ψ	165 ± 15	10.7 ± 1.0	325 ± 19	17.4 ± 1.1

Table 3.4: Results of binned ΔE fit for all flavor tagged events. The fractions and yields are for the range $|\Delta E| < 80$ MeV.

EMC K_L^0 - $J/\psi \to ee$						
	Lepton Frac(%)	Kaon1 Frac(%)	Kaon2 Frac(%)	KaonPion Frac(%)	Pion Frac(%)	Other Frac(%)
Signal	30.2 ± 3.1	33.8 ± 2.9	31.8 ± 2.3	25.2 ± 2.5	29.7 ± 2.5	26.7 ± 3.1
J/ψ-X	54.4 ± 3.7	54.6 ± 3.4	49.9 ± 2.9	54.0 ± 3.2	49.5 ± 3.2	56.0 ± 3.8
non-J/ψ	15.4 ± 2.6	11.7 ± 2.1	18.3 ± 1.9	20.8 ± 2.2	20.7 ± 2.3	17.4 ± 2.5
EMC K_L^0 - $J/\psi \to \mu\mu$						
	Lepton Frac(%)	Kaon1 Frac(%)	Kaon2 Frac(%)	KaonPion Frac(%)	Pion Frac(%)	Other Frac(%)
Signal	31.8 ± 3.2	28.6 ± 2.4	26.3 ± 1.8	20.0 ± 1.9	24.4 ± 2.0	20.8 ± 2.3
J/ψ-X	57.9 ± 3.7	46.7 ± 3.2	41.8 ± 2.7	43.5 ± 3.1	41.1 ± 3.0	44.1 ± 3.6
non-J/ψ	10.3 ± 1.8	24.7 ± 2.2	31.8 ± 2.0	36.5 ± 2.4	34.4 ± 2.2	35.1 ± 2.8

Table 3.5: Results of yields from the ΔE fit split by tagging categories for EMC K_L^0 events. The fractions and yields are for the range $|\Delta E| < 80$ MeV.

IFR K_L^0 - $J/\psi \to ee$						
	Lepton Frac(%)	Kaon1 Frac(%)	Kaon2 Frac(%)	KaonPion Frac(%)	Pion Frac(%)	Other Frac(%)
Signal	56.3 ± 5.5	51.1 ± 5.2	40.2 ± 4.1	50.8 ± 4.7	48.0 ± 4.8	44.8 ± 5.4
J/ψ-X	36.8 ± 5.7	44.2 ± 5.4	48.5 ± 4.5	38.4 ± 5.1	38.5 ± 5.1	40.3 ± 6.0
non-J/ψ	6.8 ± 2.3	4.6 ± 1.8	11.2 ± 2.2	10.8 ± 2.4	13.5 ± 2.5	14.9 ± 3.4
IFR K_L^0 - $J/\psi \to \mu\mu$						
	Lepton Frac(%)	Kaon1 Frac(%)	Kaon2 Frac(%)	KaonPion Frac(%)	Pion Frac(%)	Other Frac(%)
Signal	56.9 ± 5.4	46.0 ± 4.5	36.6 ± 3.6	45.9 ± 4.1	43.8 ± 4.1	42.1 ± 4.8
J/ψ-X	37.6 ± 5.8	40.2 ± 5.2	44.7 ± 4.4	35.1 ± 4.9	35.6 ± 5.0	38.3 ± 5.8
non-J/ψ	5.4 ± 1.9	13.9 ± 2.5	18.7 ± 2.4	19.0 ± 2.6	20.6 ± 2.8	19.6 ± 3.0

Table 3.6: Results of yields from the ΔE fit split by tagging categories for IFR K_L^0 events. The fractions and yields are for the range $|\Delta E| < 80$ MeV.

EMC K_L^0				
	ΔE Fit $\psi \to ee$		ΔE Fit $\psi \to \mu\mu$	
	Events	Fraction	Events	Fraction
Run 1	41 ± 9	26.0 ± 5.0	77 ± 11	35.5 ± 5.0
Run 2	127 ± 15	24.6 ± 2.5	223 ± 19	36.3 ± 2.9
Run 3	60 ± 11	19.9 ± 3.1	104 ± 14	30.1 ± 3.8
Run 4	194 ± 19	22.0 ± 1.8	350 ± 25	32.3 ± 2.2
Run 5	229 ± 20	20.8 ± 1.6	432 ± 28	30.6 ± 1.9
Run 6	135 ± 16	20.3 ± 2.2	210 ± 19	29.6 ± 2.6
IFR K_L^0				
	ΔE Fit $\psi \to ee$		ΔE Fit $\psi \to \mu\mu$	
	Events	Fraction	Events	Fraction
Run 1	38 ± 3	43.8 ± 3.7	54 ± 4	59.7 ± 3.5
Run 2	124 ± 18	51.7 ± 5.3	168 ± 14	67.6 ± 3.6
Run 3	54 ± 15	48.7 ± 9.9	82 ± 10	60.0 ± 6.2
Run 4	155 ± 20	42.3 ± 4.3	223 ± 19	56.2 ± 4.2
Run 5	200 ± 22	39.1 ± 3.6	290 ± 22	50.8 ± 3.5
Run 6	136 ± 18	35.8 ± 4.1	197 ± 18	49.0 ± 4.2

Table 3.7: Results of binned ΔE fit for all tagged signal events by run. The fractions and yields are for the range $|\Delta E| < 80$ MeV.

Run Block	EMC K_L		IFR K_L	
	$J/\psi \to ee$ Events per fb^{-1}	$J/\psi \to \mu\mu$ Events per fb^{-1}	$J/\psi \to ee$ Events per fb^{-1}	$J/\psi \to \mu\mu$ Events per fb^{-1}
Run 1	2.45 ± 0.49	4.79 ± 0.64	3.03 ± 1.17	4.06 ± 0.54
Run 2	2.88 ± 0.29	4.89 ± 0.36	2.85 ± 0.34	3.72 ± 0.28
Run 3	2.70 ± 0.40	4.62 ± 0.50	1.95 ± 0.40	3.25 ± 0.37
Run 4	2.62 ± 0.26	4.65 ± 0.29	2.12 ± 0.22	3.04 ± 0.21
Run 5	2.93 ± 0.20	3.52 ± 0.21	2.18 ± 0.18	2.42 ± 0.17
Run 6	2.82 ± 0.27	2.86 ± 0.24	2.58 ± 0.26	3.28 ± 0.27
All	2.79 ± 0.26	4.00 ± 0.30	2.36 ± 0.29	3.00 ± 0.25

Table 3.8: Number of events per fb^{-1} by run block.

3.5 Measurement of CP Asymmetries at *BABAR*

As discussed in the first chapter, in order to measure *CP* asymmetries, we study the $B^0\overline{B}^0$ system, which evolves in a coherent state until one of the B^0 mesons decays. We proceed to tag the flavor of one of the B^0 (B_{tag}) as discussed in Section 3.2 to determine the flavor of the other B at t_0, the time of the decay of the B_{tag}. We require that the second B (B_{reco}) decays to $J/\psi\, K_L^0$. We can then measure the proper time interval between the decay of the two B mesons, $\Delta t = t_{J/\psi\, K_L^0} - t_{tag}$.

Recalling Equation 1.113, and introducing the dilution factor $\mathcal{D} \equiv 1 - 2\omega$ to account for the probability ω that the flavor of the tagging B is not identified correctly, we can write the time-dependent rate for the decay of the B_{reco} final state as

$$f_{\pm}(\Delta t) = \frac{\Gamma}{4} e^{-\Gamma \Delta t}[(1 \mp \Delta\omega) \pm \mathcal{D} S \sin \Delta m_d \Delta t]. \tag{3.8}$$

In order to account for the finite resolution of the detector, $f_{\pm}$ must be convoluted with a time resolution function $\mathcal{R}$, such that

$$\mathcal{F}_{\pm} \equiv f_{\pm} \otimes \mathcal{R}. \tag{3.9}$$

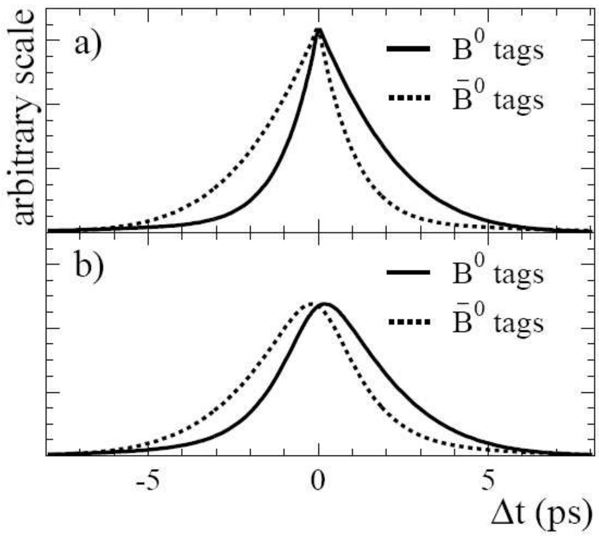

Figure 3.11: Expected Δt distribution for B^0-tagged and $\overline{B}^0$-tagged events a) without mistag nor Δt resolution effects, and b) with mistag and Δt resolution effects.

Figure 3.11 shows the effects of the mistag and the Δt resolution on the time-dependent distribution for B^0-tagged and $\overline{B}^0$-tagged events. We can then build a CPV observable

$$\mathcal{A}_{CP}(\Delta t) = \frac{\mathcal{F}_+(\Delta t) - \mathcal{F}_-(\Delta t)}{\mathcal{F}_+(\Delta t) + \mathcal{F}_-(\Delta t)}, \tag{3.10}$$

which is proportional to S if one neglects resolution effects

$$\mathcal{A}_{CP}(\Delta t) \propto \mathcal{D} S \sin \Delta m_d \Delta t. \tag{3.11}$$

The value of the parameter S can be extracted by maximizing the likelihood function

$$\ln \mathcal{L}_{CP} = \sum_{tag} [\sum_{B^0} \ln \mathcal{F}_+ + \sum_{\overline{B}^0} \ln \mathcal{F}_-], \tag{3.12}$$

where the sum is done over the tagging categories; for each tagging category, the first and second term are summed over the B^0 and $\overline{B}^0$ events, respectively. One also needs to add additional terms to take into account the backgrounds and their time dependences (see Section 3.7).

In addition to the likelihood function described in Equation 3.12, we introduce a mixing likelihood function to determine the frequency of oscillations of the B system, Δm_d. Similarly to the above reasoning, we can use Equations 3.2 and 3.3, and define

$$\ln \mathcal{L}_{mix} = \sum_{tag} [\sum_{unmixed} \ln \mathcal{H}_{+} + \sum_{mixed} \ln \mathcal{H}_{-}], \tag{3.13}$$

where

$$\mathcal{H}_{\pm} \equiv g_{\pm} \otimes \mathcal{R}. \tag{3.14}$$

The mistag rates and Δz resolution are needed for the measurement, but are best determined using the large mixing sample. We therefore perform the fit by simultaneously maximizing the sum

$$\ln \mathcal{L}_{CP} + \ln \mathcal{L}_{mix} \tag{3.15}$$

on the combined tagged B_{flav} and $B^0 \to J/\psi K^0_L$ signal samples.

In the following sections, we will describe how to determine the likelihood function, as well as its different input variables. We will then be able to perform the fit that will lead to the value of the CP asymmetry variables, S and C.

3.6 Time Difference Measurement

The proper time difference between the decay of the reconstructed B meson (B_{reco}) and the flavor-tagging B meson (B_{tag}), $\Delta t = t_{rec} - t_{tag}$, is determined from the measurement of the separation between the vertices of those two B mesons along the z axis, Δz.

The z position of the B_{reco} vertex is determined from the charged daughter tracks. The

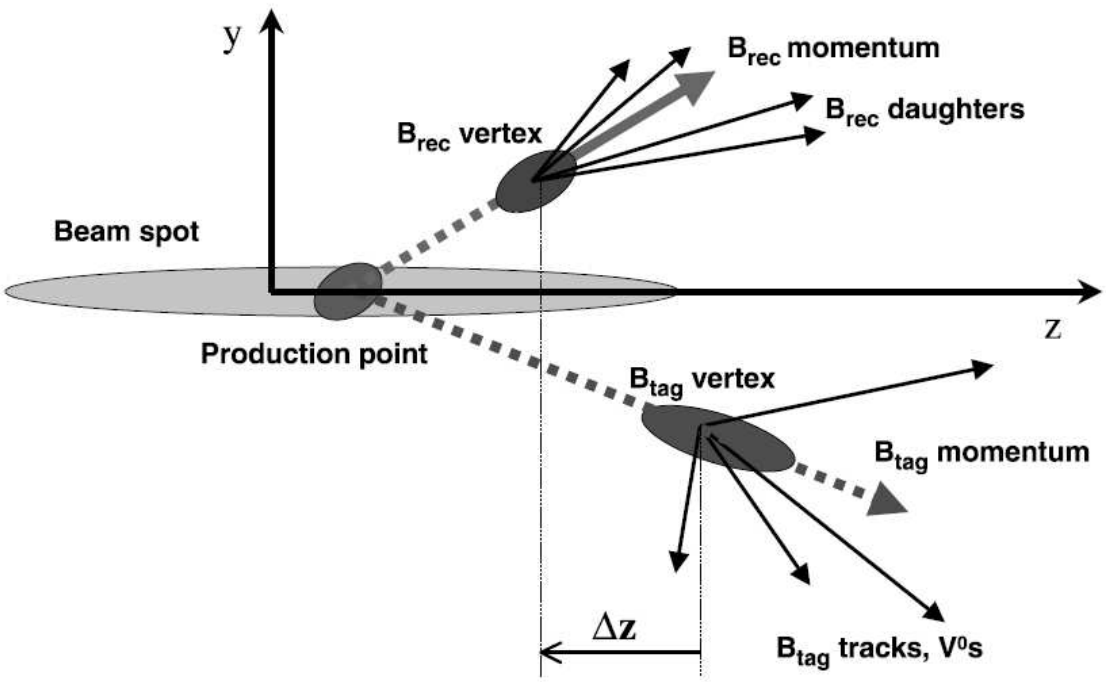

Figure 3.12: Geometry of a $\Upsilon(4S) \to B\bar{B}$ decay in the yz plane.

B_{tag} decay vertex is determined by fitting tracks not belonging to the B_{reco} candidate to a common vertex, and including constraints from the beam spot location and the B_{reco} momentum as shown in Figure 3.12 [38]. Neglecting the B momentum in the $\Upsilon(4S)$ rest frame, we can write

$$\Delta z = \beta\gamma c \Delta t, \tag{3.16}$$

where $\beta\gamma$ is the $\Upsilon(4S)$ boost factor, whose average value is 0.56. Corrections are applied to account for the momentum of the B mesons in the $\Upsilon(4S)$ rest frame (340 MeV/c on average) and improve the Δt resolution.

The Δt distributions for the signal are convolved with a resolution function common to both the B_{flav} and B_{CP} samples, modeled by the sum of three Gaussian functions [38], called the core, tail and outlier components. They can be represented as a function of the reconstruction uncertainty $\delta t = \Delta t - \Delta t_{\rm true}$ as follows:

$$\begin{aligned}
\mathcal{R}(\delta t;\sigma_{\Delta t}) &= f_{\rm core} h_G(\delta t;\delta_{\rm core}\sigma_{\Delta t}, S_{\rm core}\sigma_{\Delta t}) \\
&+ f_{\rm tail} h_G(\delta t;\delta_{\rm tail}\sigma_{\Delta t}, S_{\rm tail}\sigma_{\Delta t}) \\
&+ f_{\rm out} h_G(\delta t;\delta_{\rm out}, S_{\rm out}),
\end{aligned} \tag{3.17}$$

where

$$h_G(\delta t;\delta,\sigma) = \frac{1}{\sqrt{2\pi}\sigma}\exp\left(-\frac{(\delta t-\delta)^2}{2\sigma^2}\right), \tag{3.18}$$

and

$$f_{\rm core} + f_{\rm tail} + f_{\rm out} = 1. \tag{3.19}$$

The widths (σ) of the core and tail components call for two independent scale factors, S_{core} and S_{tail}, to accommodate an overall underestimate or overestimate of the uncertainties. The value of S_{tail} is derived from MC studies and fixed to be 3.

We account for residual charm decay products included in the $B_{\rm flav}$ vertex by allowing the core and tail Gaussians distributions to have non-zero means (bias). While the bias (δ) and width of the core component are split between lepton-tagged events and non-lepton tagged events, we use common parameters for the tail component. In order to account for the strong correlations with other resolution parameters, the outlier bias and width are fixed to 0 ps and 8 ps, respectively.

Events are accepted if the calculated Δt uncertainty is less than 2.5 ps and $|\Delta t|$ is less than 20 ps. The fraction of signal MC events satisfying such a requirement is 95 %.

3.7 Maximum Likelihood Fit Method : the Δt fit

The CPV parameters, S and C are extracted by performing a simultaneous maximum likelihood fit to the Δt distribution of the flavor-tagged $J/\psi K_L^0$ and B_{flav} samples.

As seen previously, an important fraction of our data sample consists of different sources of background, which need to be included in the definition of our likelihood function (see Equation 3.12). In particular, some of these backgrounds have a non-zero CP asymmetry, such as $J/\psi K_S^0$. In order to include the properties of the background events, we modify the probability density function (PDF) $\mathcal{F}_\pm$ so that

$$\mathcal{F}_\pm = f^{signal}\mathcal{F}_\pm + \sum_{J/\psi X_i} f^i \mathcal{F}_\pm + f^{non-J/\psi}\mathcal{F}_\pm^{non-J/\psi}. \tag{3.20}$$

f^{signal}, f^i and $f^{non-jpsi}$ correspond to the relative fraction of signal, $B^0 \to J/\psi X_i$ and non-J/ψ events, respectively. $J/\psi X_i$ represents one of the decay products of the inclusive-J/ψ background. These fractions will be determined from a binned maximum likelihood fit to ΔE, as seen in Section 3.4. Different PDFs exist for each tagging and K_L^0 reconstruction category (in the EMC or IFR).

While we can use the same resolution function for signal and inclusive-J/ψ background, the non-J/ψ background has contributions from continuum events ($u\bar{u}, d\bar{d}, s\bar{s}, c\bar{c}$), B^+B^- decays and $B^0\overline{B^0}$ decays. The continuum is parameterized as a prompt time-dependent component while the $B\bar{B}$ backgrounds are treated as having a single 'effective' lifetime. The non-J/ψ background PDF therefore consists of a zero and a non-zero lifetime component convolved with a resolution function $\mathcal{R}^{non-J/\psi}$ distinct from that of the signal:

$$\mathcal{F}_\pm^{non-J/\psi} = \frac{1}{2}f_0\delta(\Delta t)\otimes\mathcal{R}^{non-J/\psi} + \frac{\Gamma_{non-J/\psi}}{4}(1-f_0)e^{-|\Delta t|/\tau_{BG}}\otimes\mathcal{R}^{non-J/\psi}, \tag{3.21}$$

where $\Gamma_{non-J/\psi}$ is the effective decay width. f_0 is the fraction of prompt background, which is determined from a Δt fit to the J/ψ dilepton mass sideband (see Section 3.3.1).

We use the RooFit package to implement the maximum likelihood fit [42].

We used different fit configurations:

- the K_L^0 only fit, whose output is the values of S and C for $B^0 \to J/\psi K_L^0$ only;
- the K_S^0 only fit, whose output is the values of S and C for $B^0 \to J/\psi K_S^0(K_S^0 \to \pi^+\pi^-$ or $\pi^0\pi^0$ only;
- the $K^0 = K_L^0 + K_S^0$ only fit, whose output is the values of S and C for $B^0 \to J/\psi K_S^0$ and $B^0 \to J/\psi K_L^0$ together, for direct comparison with the results from Belle;
- the simultaneous fit for each of the 7 charmonium modes, whose output is the individual values of S and C for each mode;
- the simultaneous fit of all the modes together, which output is the values of S and C on the entire CP sample.

The systematic errors were calculated for all of the above cases (see Section 4.2).

In addition to S and C, there are 69 free parameters in the CP fit. For the signal, these consist of

- 7 parameters for the Δt resolution,
- 12 parameters for the average mistag fractions w and the differences Δw between B^0 and $\overline{B}^0$ mistag fractions for each tagging category,

- 7 parameters for the difference between B^0 and $\overline{B}^0$ reconstruction and tagging efficiencies.

The background is described by

- 24 mistag fraction parameters,
- 3 parameters for the Δt resolution,
- 4 parameters for the B_{flav} time dependence,
- 8 parameters for possible CP violation in the background, including the apparent CP asymmetry of non-peaking events in each tagging category,
- 1 parameter for possible direct CP violation in the $\chi_{c1} K_S^0$ background coming from $J/\psi\, K^{*0}$, and
- 3 parameters for possible direct CP violation in the $J/\psi\, K_L^0$ mode, coming from $J/\psi\, K_S^0$, $J/\psi\, K^{*0}$, and the remaining J/ψ backgrounds.

The effective $|\lambda|$ of the non-J/ψ background is fixed from a fit to the J/ψ-candidate sidebands in $J/\psi\, K_L^0$. The determination of the mistag fractions and Δt resolution function parameters for the signal is dominated by the B_{flav} sample, which is about 10 times more abundant than the CP sample.

Likelihood Fit Validation

Before fitting the data in order to extract CP asymmetry parameters, we validate the integrity of the likelihood. We perform different tests to validate the fit. The first of these tests consists of generating ensembles of simulated experiments from the PDF and fitting each simulated experiment. The distribution of fitted S and

C parameters are required to be unbiased, and we verify that the uncertainties are extracted correctly from the fit.

The second test involves fitting simulated CP events with the full BABAR detector simulation. We later assign a systematic uncertainty corresponding to any deviations and the statistical uncertainties of the mean values of the fitted S and C distributions from the generated values.

The third test on our ability to extract S and C correctly is to perform null tests on control samples of neutral and charged B events where S and C should equal zero. We use charged B decays to $J/\psi K^{\pm}$, $\psi(2S)K^{\pm}$, $\chi_{c1}K^{\pm}$, $J/\psi K^{*\pm}$ with $K^{*\pm} \rightarrow K^{\pm}\pi^{0}$ and $K^{0}_{S}\pi^{\pm}$, and neutral $B_{\rm flav}$ decays for this purpose. The parameters S and C from the fit are consistent with zero within the statistical uncertainties , as expected from the SM.

3.8 Input Parameters Calculation

A number of parameters are needed in the maximum likelihood fit. In the following, we show how they are determined and point out the differences and similarities we observe between signal and background.
Several parameters for the (S,C) fit are unique to the $B^{0} \rightarrow J/\psi K^{0}_{L}$ decay :

- The relative fractions for signal and background modes ($J/\psi K^{*0}$, $J/\psi K^{*+}$, $J/\psi K^{0}_{S}$, $J/\psi K^{0}_{L}\pi^{0}$, $J/\psi K^{0}_{L}\pi^{+}$, $J/\chi_{c1}K^{0}_{L}$, the rest of J/ψ inclusive background, non-J/ψ prompt and non prompt backgrounds). They are split by reconstruction type (EMC or IFR), J/ψ lepton decay type and tagging category.

- The parameters of the PDFs to the ΔE shapes for signal, inclusive J/ψ, $J/\psi K_S^0$, and the non-J/ψ distributions derived from fits to the Monte Carlo events and split by reconstruction type (EMC or IFR) and J/ψ lepton decay type.

3.8.1 Sample Composition

Inclusive $B^0 \to J/\psi X$

More than 90% of the events that pass our selection contain a real J/ψ. Table 3.9 lists the number of inclusive J/ψ Monte Carlo events that pass our selection. The table is broken down by decay mode, flavor tag type, and K_L^0 reconstruction type. The data has been divided by K_L^0 reconstruction type because the two samples have different detector-related backgrounds and thus different purity (signal fraction). The signal and total inclusive J/ψ fractions are also broken down by the decay mode of the J/ψ. Dividing the data into high and low purity samples gives a statistical advantage in the maximum likelihood fit for (S,C). It has been assumed that the ratio between $J/\psi K_L^0$ and inclusive J/ψ events would not be affected by the J/ψ lepton type within statistical precision, so the data was not further divided by lepton type. A plot of $J/\psi K_L^0$ and inclusive J/ψ events split by lepton type is included in Section 3.8.2. The fractions are listed by flavor tag type because the flavor tagging efficiency could be different for different decay modes, which would give a flavor tag dependent sample composition. In Table 3.9, the top 6 background modes, which with the exception of $J/\psi K_S^0$, contain a real K_L^0 in the decay, are specifically listed.

EMC K_L^0 Decay mode	All events Evts	Frac(%)	Lepton tag Evts	Frac(%)	Kaon1 tag Evts	Frac(%)	Kaon2 Evts	Frac(%)
$J/\psi K_L^0$ (signal)	28008	40.35 ± 0.19	2425	34.88 ± 0.57	3033	40.96 ± 0.57	4778	40.19 ± 0.45
$J/\psi K^{*0}$	6046	8.71 ± 0.11	611	8.79 ± 0.34	590	7.97 ± 0.31	953	8.02 ± 0.25
$J/\psi K_L \pi^0$	337	0.49 ± 0.03	36	0.52 ± 0.09	34	0.46 ± 0.08	55	0.46 ± 0.06
$J/\psi K^{*+}$	8959	12.91 ± 0.13	1016	14.61 ± 0.42	1113	15.03 ± 0.42	1634	13.74 ± 0.32
$J/\psi K_L \pi^+$	446	0.64 ± 0.03	46	0.66 ± 0.10	45	0.61 ± 0.09	83	0.70 ± 0.08
$J/\psi K_S$	2929	4.22 ± 0.08	289	4.16 ± 0.24	294	3.97 ± 0.23	461	3.88 ± 0.18
$\chi_{c1} K_L$	984	1.42 ± 0.04	91	1.31 ± 0.14	96	1.30 ± 0.13	175	1.47 ± 0.11
Other $J/\psi X$	21702	31.27 ± 0.18	2439	35.08 ± 0.57	2200	29.71 ± 0.53	3751	31.55 ± 0.43

EMC K_L^0 Decay mode	KaonPion tag Evts	Frac(%)	Pions tag Evts	Frac(%)	Other tag Evts	Frac(%)	Untagged Evts	Frac(%)
$J/\psi K_L^0$ (signal)	3874	40.21 ± 0.50	4015	39.68 ± 0.49	2723	40.30 ± 0.60	7160	42.99 ± 0.38
$J/\psi K^{*0}$	792	8.22 ± 0.28	928	9.17 ± 0.29	601	8.90 ± 0.35	1571	9.43 ± 0.23
$J/\psi K_L \pi^0$	45	0.47 ± 0.07	50	0.49 ± 0.07	34	0.50 ± 0.09	83	0.50 ± 0.05
$J/\psi K^{*+}$	1191	12.36 ± 0.34	1168	11.54 ± 0.32	839	12.42 ± 0.40	1998	12.00 ± 0.25
$J/\psi K_L \pi^+$	56	0.58 ± 0.08	69	0.68 ± 0.08	44	0.65 ± 0.10	103	0.62 ± 0.06
$J/\psi K_S$	380	3.94 ± 0.20	428	4.23 ± 0.20	301	4.46 ± 0.25	776	4.66 ± 0.16
$\chi_{c1} K_L$	126	1.31 ± 0.12	138	1.36 ± 0.12	103	1.52 ± 0.15	255	1.53 ± 0.10
Other $J/\psi X$	3170	32.90 ± 0.48	3322	32.83 ± 0.47	2111	31.25 ± 0.56	4709	28.27 ± 0.35

IFR K_L^0 Decay mode	All events Evts	Frac(%)	Lepton tag Evts	Frac(%)	Kaon1 tag Evts	Frac(%)	Kaon2 tag Evts	Frac(%)
$J/\psi K_L^0$ (signal)	15486	60.13 ± 0.31	1413	57.98 ± 1.00	1528	59.32 ± 0.97	2583	59.67 ± 0.75
$J/\psi K^{*0}$	2122	8.24 ± 0.17	170	6.98 ± 0.52	187	7.26 ± 0.51	305	7.05 ± 0.39
$J/\psi K_L \pi^0$	133	0.52 ± 0.04	11	0.45 ± 0.14	18	0.70 ± 0.16	17	0.39 ± 0.10
$J/\psi K^{*+}$	4051	15.73 ± 0.23	427	17.52 ± 0.77	444	17.24 ± 0.74	757	17.49 ± 0.58
$J/\psi K_L \pi^+$	204	0.79 ± 0.06	27	1.11 ± 0.21	20	0.78 ± 0.17	26	0.60 ± 0.12
$J/\psi K_S$	183	0.71 ± 0.05	21	0.86 ± 0.19	17	0.66 ± 0.16	25	0.58 ± 0.12
$\chi_{c1} K_L$	432	1.68 ± 0.08	38	1.56 ± 0.25	54	2.10 ± 0.28	67	1.55 ± 0.19
Other $J/\psi X$	3145	12.21 ± 0.20	330	13.54 ± 0.69	308	11.96 ± 0.64	549	12.68 ± 0.51

IFR K_L^0 Decay mode	KaonPion tag Evts	Frac(%)	Pions tag Evts	Frac(%)	Other tag Evts	Frac(%)	Untagged Evts	Frac(%)
$J/\psi K_L^0$ (signal)	2095	60.31 ± 0.83	2222	61.26 ± 0.81	1604	59.83 ± 0.95	4041	60.93 ± 0.60
$J/\psi K^{*0}$	316	9.10 ± 0.49	330	9.10 ± 0.48	216	8.06 ± 0.53	598	9.02 ± 0.35
$J/\psi K_L \pi^0$	16	0.46 ± 0.11	20	0.55 ± 0.12	12	0.45 ± 0.13	39	0.59 ± 0.09
$J/\psi K^{*+}$	538	15.49 ± 0.61	530	14.61 ± 0.59	403	15.03 ± 0.69	952	14.35 ± 0.43
$J/\psi K_L \pi^+$	30	0.86 ± 0.16	25	0.69 ± 0.14	19	0.71 ± 0.16	57	0.86 ± 0.11
$J/\psi K_S$	25	0.72 ± 0.14	16	0.44 ± 0.11	26	0.97 ± 0.19	53	0.80 ± 0.11
$\chi_{c1} K_L$	39	1.12 ± 0.18	46	1.27 ± 0.19	53	1.98 ± 0.27	135	2.04 ± 0.17
Other $J/\psi X$	415	11.95 ± 0.55	438	12.08 ± 0.54	348	12.98 ± 0.65	757	11.41 ± 0.39

Table 3.9: Sample composition of SP9 inclusive J/ψ Monte Carlo as a function of flavor tag. A cut of $|\Delta E| < 80$ MeV has been applied.

Non-J/ψ background

We recall from Section 3.3.1 that the non-J/ψ background is characterized using events from the J/ψ di-lepton invariant mass sideband, which are required to pass all other event selection criteria and satisfy

- $J/\psi \to \mu^+\mu^-$; $2.90 < M(\mu\mu) < 3.00$ GeV and $3.175 < M(\mu\mu) < 3.50$ GeV
- $J/\psi \to e^+e^-$; $3.175 < M(ee) < 3.50$ GeV.

We observed that the background resolution function for the B_{reco} sample accurately described the non-$J/\psi K^0_L$ sideband data in each tagging category. Therefore, the resolution function and lifetime (τ_{BG}) for the non-J/ψ background events were taken from the B_{reco} background, and the fractions of the prompt component are determined from the Δt fits in each tagging category. Figure 3.13 shows the results of an unbinned likelihood fit of the Δt structure of the data sideband events split by tagging categories. In the fits, all the other parameters were fixed to those of the B_{reco} sample. The fractions of prompt background are used as input to the Δt fit (see Section 3.7).

Calculation of Input Parameters from the Binned Likelihood Fit on ΔE

The sample composition fractions from the ΔE fit (F_{sig},$F_{\psi X}$ and $F_{non-\psi}$) done simultaneously for $J/\psi \to e^+e^-$ and $J/\psi \to \mu^+\mu^-$ and separately for EMC and IFR (see Section 3.4) are fixed inputs to the δt fit split by tagging categories. The fractions of signal events ($J/\psi K^0_L$) are given in Tables 3.5 and 3.6, and also shown in Tables 3.10 and 3.11. The fractions for the $J/\psi X$ component are adjusted according to the itemized background composition given in Table 3.9. For each background mode, the

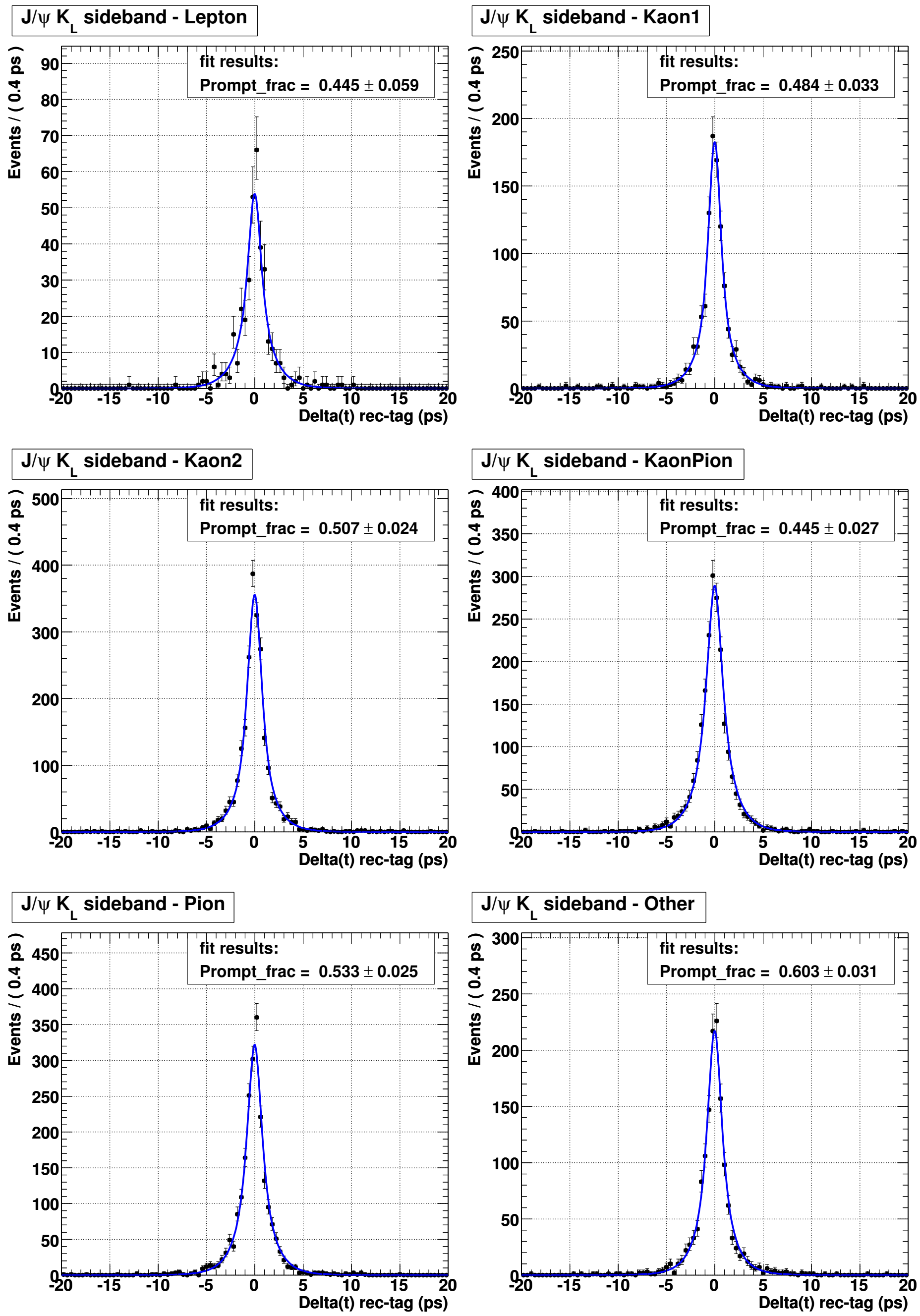

Figure 3.13: Fit of the J/ψ di-lepton invariant mass data sideband Δt distribution.

number of events is taken from Table 3.9 and normalized with respect to the other background modes. The resulting number is then multiplied by the inclusive-J/ψ fractions of Tables 3.5 and 3.6 to obtain the fractions in Tables 3.10 and 3.11 for the EMC and IFR respectively. For the non-J/ψ component, the prompt fractions obtained in Figure 3.13 for each tagging category are used as input for the calculation of the final fractions. Combined with the fractions in Tables 3.5 and 3.6, they give us the non-J/ψ prompt and lifetime fractions of Tables 3.10 and 3.11.

For both Tables 3.10 and 3.11, we note that the $J/\psi K^0_L$, $J/\psi K^{*0}$, $J/\psi K^{*+}$, $J/\psi K^0_S$, $J/\psi K^0_L \pi^+$, $\chi_c(1) K^0_L$, other J/ψ X, non$-J/\psi$, lifetime and non$-J/\psi$, prompt component fractions sum to 1.0 as expected. The $J/\psi K^0_L \pi^0$ component shown falls into the other J/ψ X category which is also shown.

3.8.2 ΔE Distributions

The variable ΔE is used on an event-by-event basis to help distinguish between signal and background in the maximum likelihood fit. As the form of the $J/\psi \to ll$ decay is not expected to influence the ΔE shape, the PDFs were generated without regard to lepton type. Monte Carlo plots for signal and inclusive J/ψ plots separated by J/ψ lepton decay mode are shown in Fig 3.14 and confirm that the ΔE shapes are similar for $J/\psi \to ee$ and $J/\psi \to \mu\mu$. In addition, Figs 3.15 and 3.16 show the ΔE distributions in the range $-0.02 < \Delta E < 0.08$ GeV for the signal $J/\psi K^0_L$ events and for all the distinct background modes superimposed on the distribution of the sum of the background modes (with the exception of the $J/\psi K^0_S$ background). We group all the background modes together, except for $J/\psi K^0_S$, because of the similarities in their ΔE shapes. We will refer to this category as $J/\psi X$ background. We choose to use 8 separate ΔE PDFs in the Δt fit, 4 for the EMC K^0_L and 4 for the IFR K^0_L:

EMC Klong - $J/\psi \to ee$						
	Tag type					
Decay mode	Lepton	Kaon1	Kaon2	KaonPion	Pion	Other
$J/\psi K_L$	0.3020	0.3380	0.3180	0.2520	0.2970	0.2670
$J/\psi K^{*0}$	0.0794	0.0797	0.0729	0.0789	0.0723	0.0818
$J/\psi K^{*+}$	0.1177	0.1181	0.1080	0.1168	0.1071	0.1212
$J/\psi K_S$	0.0385	0.0386	0.0353	0.0382	0.0350	0.0396
$J/\psi K_L \pi^0$	0.0044	0.0044	0.0041	0.0044	0.0040	0.0046
$J/\psi K_L \pi^+$	0.0059	0.0059	0.0054	0.0058	0.0053	0.0060
$\chi_c(1) K_L$	0.0129	0.0130	0.0119	0.0128	0.0118	0.0133
Oth $J/\psi X$	0.2897	0.2897	0.2655	0.2875	0.2645	0.2971
non$-J/\psi$, lifetime	0.0885	0.0626	0.0937	0.1202	0.1002	0.0710
non$-J/\psi$, prompt	0.0654	0.0544	0.0893	0.0878	0.1068	0.1030

EMC Klong - $J/\psi \to \mu\mu$						
	Tag type					
Decay mode	Lepton	Kaon1	Kaon2	KaonPion	Pion	Other
$J/\psi K_L$	0.3180	0.2860	0.2630	0.2000	0.2440	0.2080
$J/\psi K^{*0}$	0.0846	0.0682	0.0610	0.0635	0.0600	0.0644
$J/\psi K^{*+}$	0.1253	0.1011	0.0904	0.0941	0.0889	0.0954
$J/\psi K_S$	0.0410	0.0330	0.0296	0.0308	0.0291	0.0312
$J/\psi K_L \pi^0$	0.0047	0.0038	0.0034	0.0035	0.0033	0.0036
$J/\psi K_L \pi^+$	0.0062	0.0050	0.0045	0.0047	0.0044	0.0048
$\chi_c(1) K_L$	0.0138	0.0111	0.0099	0.0103	0.0098	0.0105
Oth $J/\psi X$	0.3081	0.2486	0.2236	0.2316	0.2198	0.2347
non$-J/\psi$, lifetime	0.0592	0.1321	0.1628	0.2110	0.1665	0.1432
non$-J/\psi$, prompt	0.0438	0.1149	0.1552	0.1540	0.1775	0.2078

Table 3.10: Sample composition fractions for $J/\psi\, K^0_L$ with K^0_L-EMC and background modes split for each tagging category and J/ψ decay mode.

IFR Klong - $J/\psi \to ee$						
	Tag type					
Decay mode	Lepton	Kaon1	Kaon2	KaonPion	Pion	Other
$J/\psi K_L$	0.5630	0.5110	0.4020	0.5080	0.4800	0.4480
$J/\psi K^{*0}$	0.0760	0.0913	0.1002	0.0793	0.0795	0.0833
$J/\psi K^{*+}$	0.1452	0.1743	0.1913	0.1515	0.1519	0.1590
$J/\psi K_S$	0.0066	0.0079	0.0086	0.0068	0.0069	0.0072
$J/\psi K_L \pi^0$	0.0048	0.0057	0.0063	0.0050	0.0050	0.0052
$J/\psi K_L \pi^+$	0.0073	0.0088	0.0096	0.0076	0.0076	0.0080
$J/\chi_c(1) K_L$	0.0155	0.0186	0.0204	0.0162	0.0162	0.0170
Oth $J/\psi X$	0.1184	0.1421	0.1559	0.1226	0.1229	0.1285
non$-J/\psi$, lifetime	0.0391	0.0246	0.0573	0.0624	0.0653	0.0608
non$-J/\psi$, prompt	0.0289	0.0214	0.0547	0.0456	0.0697	0.0882

IFR Klong - $J/\psi \to \mu\mu$						
	Tag type					
Decay mode	Lepton	Kaon1	Kaon2	KaonPion	Pion	Other
$J/\psi K_L$	0.5690	0.4600	0.3660	0.4590	0.4380	0.4210
$J/\psi K^{*0}$	0.0777	0.0831	0.0924	0.0725	0.0736	0.0791
$J/\psi K^{*+}$	0.1483	0.1586	0.1763	0.1385	0.1404	0.1511
$J/\psi K_S$	0.0067	0.0072	0.0080	0.0063	0.0063	0.0068
$J/\psi K_L \pi^0$	0.0049	0.0052	0.0058	0.0045	0.0046	0.0050
$J/\psi K_L \pi^+$	0.0075	0.0080	0.0089	0.0070	0.0071	0.0076
$J/\chi_c(1) K_L$	0.0158	0.0169	0.0188	0.0148	0.0150	0.0161
Oth $J/\psi X$	0.1211	0.1272	0.1426	0.1119	0.1136	0.1223
non$-J/\psi$, lifetime	0.0310	0.0744	0.0957	0.1098	0.0997	0.0800
non$-J/\psi$, prompt	0.0229	0.0646	0.0913	0.0802	0.1063	0.1160

Table 3.11: Sample composition fractions for $J/\psi\, K^0_L$ with K^0_L-IFR and background modes split for each tagging category and J/ψ decay mode.

- $J/\psi\,K_L^0$ (signal),
- $J/\psi\,K_S^0$ background,
- J/ψ X background, excluding $J/\psi\,K_S^0$,
- non-J/ψ background.

Figures 3.17 and 3.18 show the ΔE fits that were used to obtain the PDFs for the EMC and IFR, respectively. The MC signal and $J/\psi\,K_S^0$ distributions were fit to a double Gaussian and an Argus [41] function, while the MC inclusive J/ψ background distribution was fit with a single Gaussian and an Argus [41] function. The non-J/ψ background ΔE shape was taken from data sideband and was fit to an Argus function [41].

3.8.3 Other Parameters

Table 3.12 lists the remaining input parameters for the maximum likelihood fit that were not already described in the text.

Parameter	Value	Reference
τ_{B^0}	1.530 ± 0.009 ps	Ref. [43]
Δm_d	$0.507 \pm 0.005\hbar$ ps^{-1}	Ref. [43]
Effective CP of $J/\psi\,K^{*0}$	-0.504 ± 0.033	Ref. [44]

Table 3.12: Miscellaneous parameters not already described in the text.

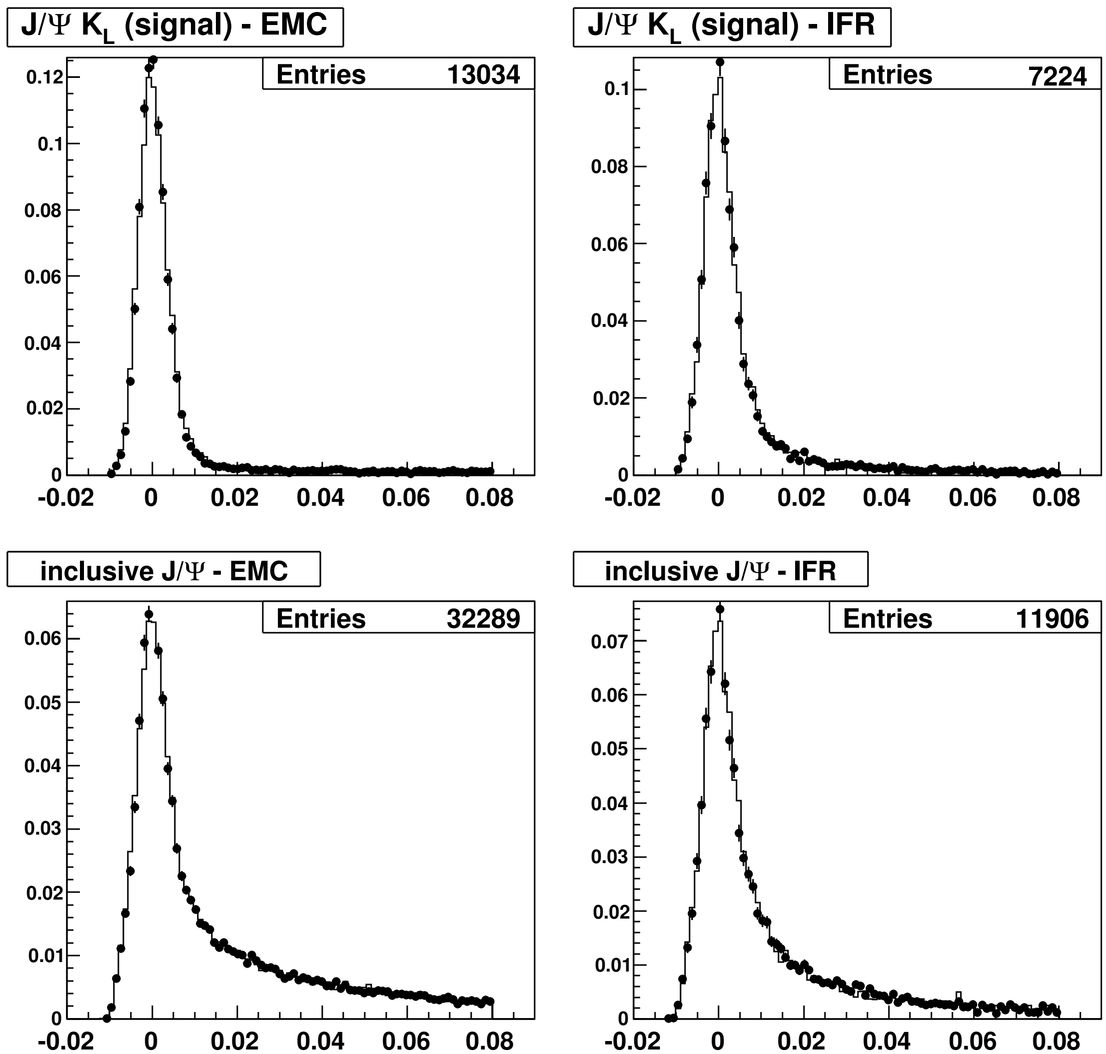

Figure 3.14: Monte Carlo ΔE distributions for $J/\psi\, K_L^0$ events in EMC (top left) and IFR (top right), and inclusive J/ψ EMC (bottom left) and IFR (bottom right) events. In each plot, the $J/\psi \to ee$ (histogram) and $J/\psi \to \mu\mu$ (points) events are normalized to unit area .

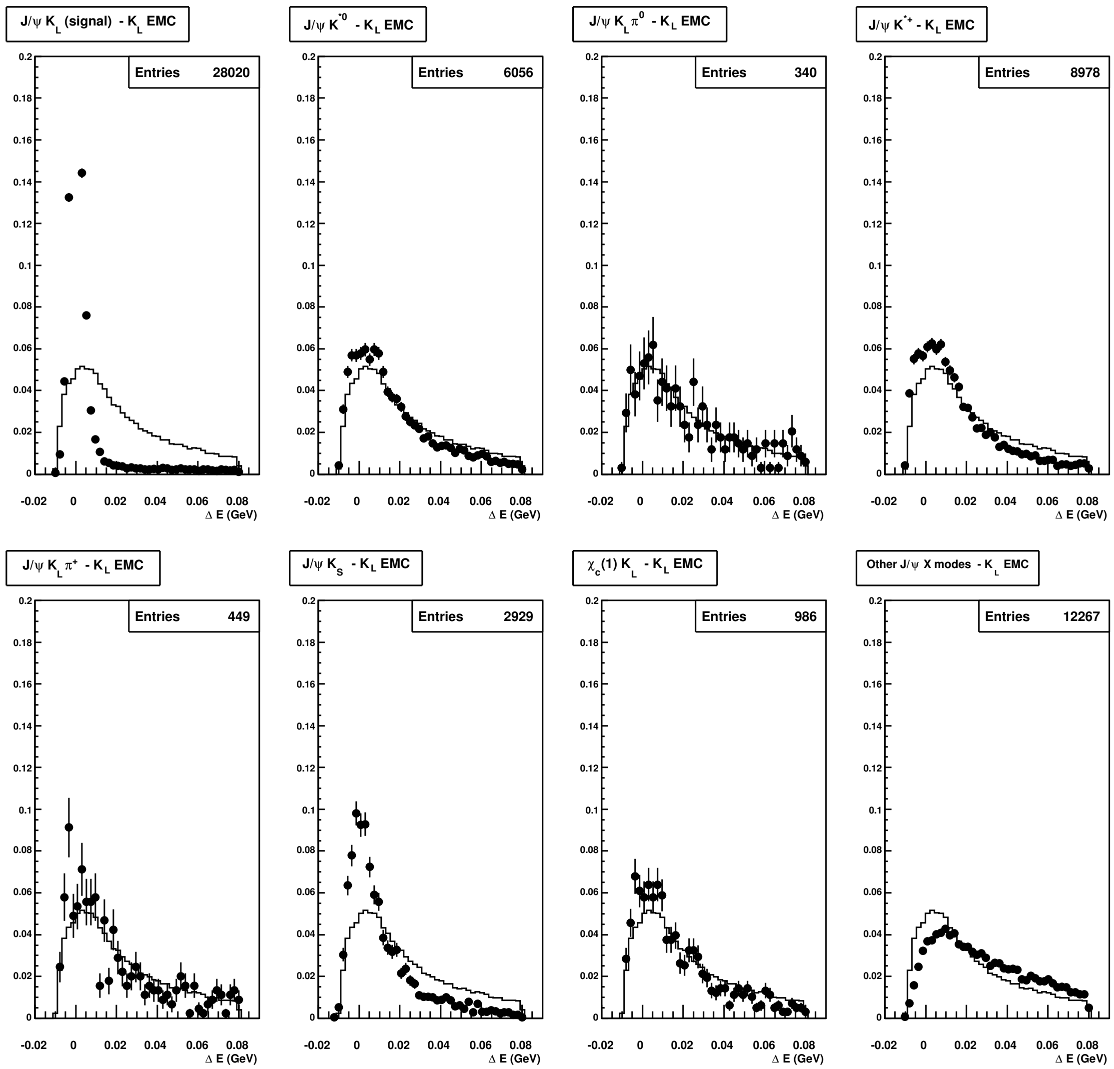

Figure 3.15: Monte Carlo ΔE distributions in the range $-0.02 < \Delta E < 0.08$ GeV for $J/\psi\, K_L^0$ events and the other background modes in EMC. Each distribution is normalized to unit area. The solid histogram in each plot corresponds to the sum of all inclusive J/ψ background modes.

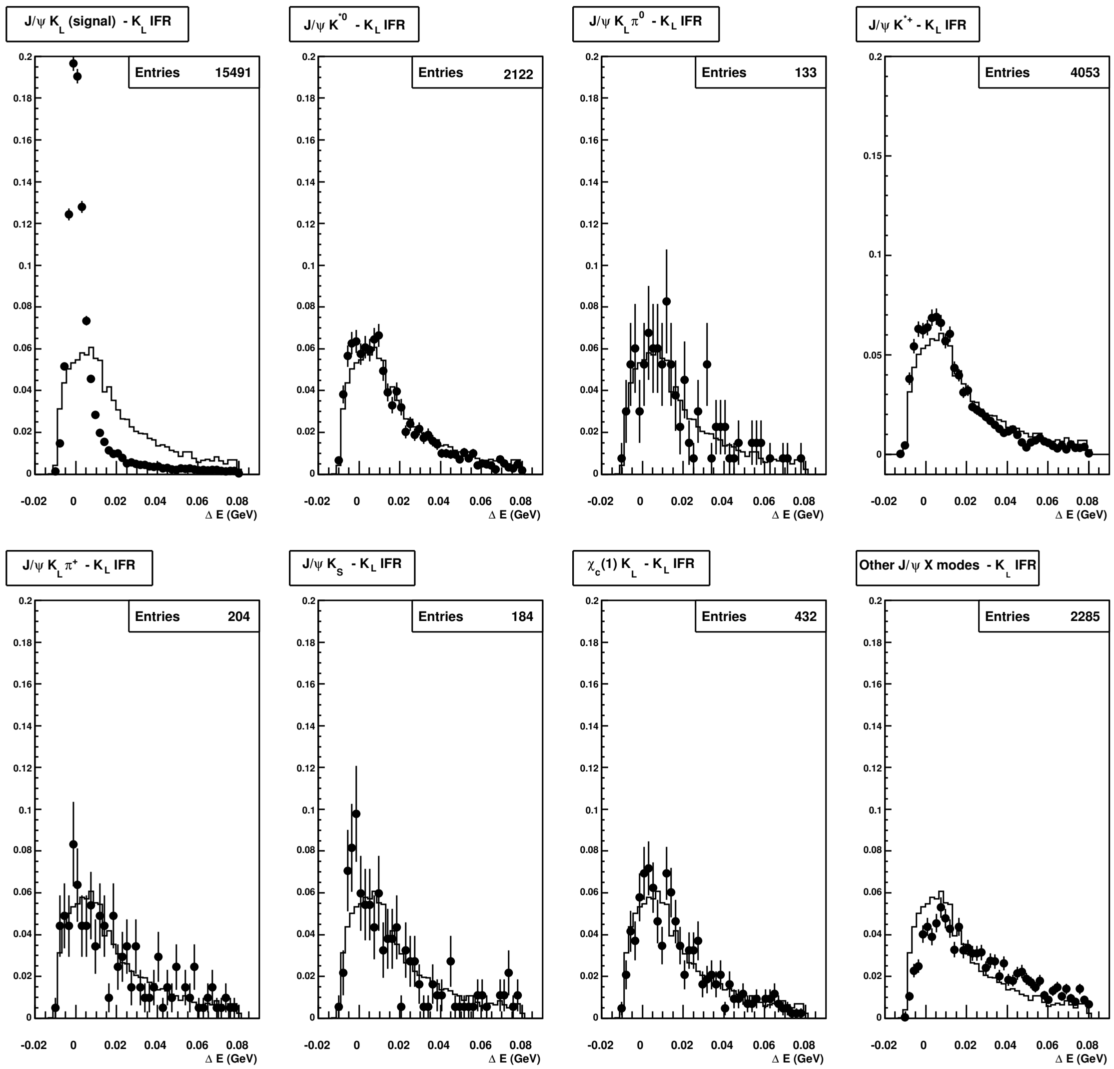

Figure 3.16: Monte Carlo ΔE distributions in the range $-0.02 < \Delta E < 0.08$ GeV for $J/\psi\, K_L^0$ events and the other background modes in IFR. Each distribution is normalized to unit area. The solid histogram in each plot corresponds to the sum of all inclusive J/ψ background modes.

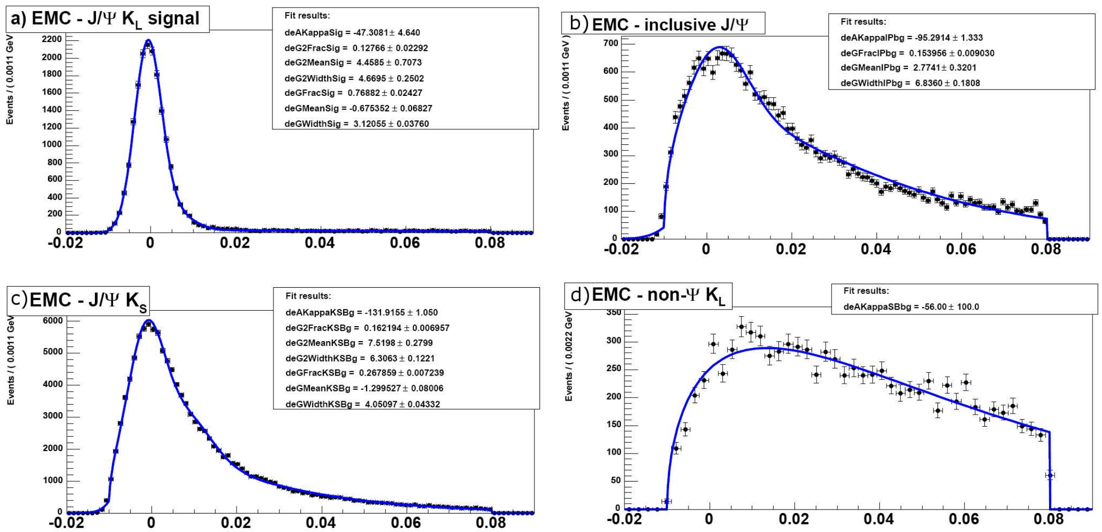

Figure 3.17: Fits of the EMC-K_L^0 ΔE distributions for the probability density functions used in the Δt fit. The Monte Carlo signal and $J/\psi\, K_S^0$ were fit to a double Gaussian + Argus function[-20,80] (a and c, respectively); The Monte Carlo inclusive J/ψ background distribution was fit to a Gaussian + Argus function [-20,80] (b); The non-J/ψ background was fit to an Argus function [-20,80] (d)

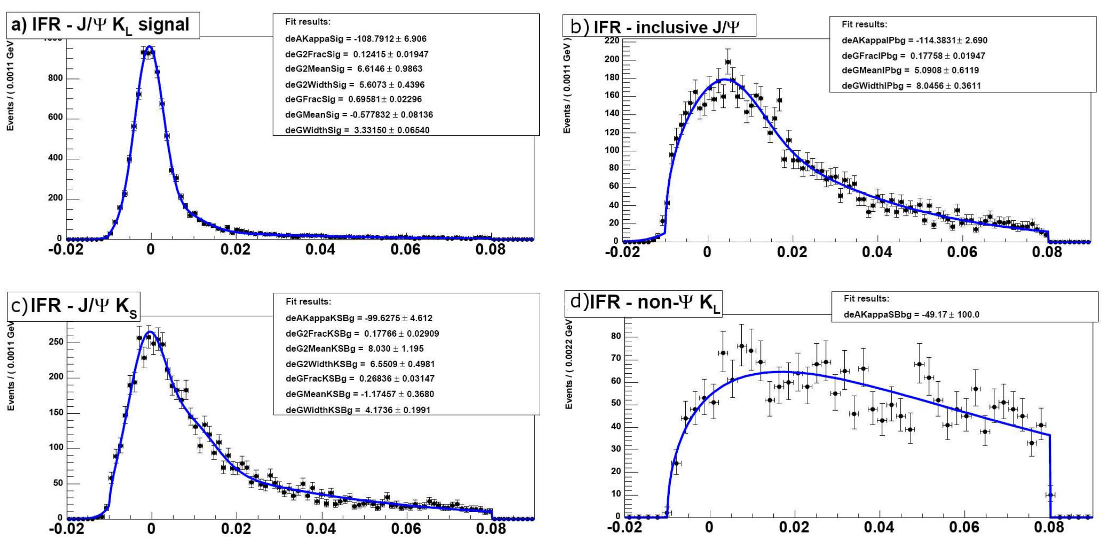

Figure 3.18: Fits of the IFR-$K_L^0 \Delta E$ distributions for the probability density functions used in the Δt fit. The Monte Carlo signal was fit to a double Gaussian + Argus function[-20,80] The Monte Carlo signal and $J/\psi\, K_S^0$ were fit to a double Gaussian + Argus function[-20,80] (a and c, respectively); The Monte Carlo inclusive J/ψ background distribution was fit to a Gaussian + Argus function [-20,80] (b); The non-J/ψ background was fit to an Argus function [-20,80] (d)

Chapter 4

Results and Conclusion

4.1 Fit Results

In this section, we present the Δt fit results from which we extract the CPV parameters S and C. The fits were performed on data and Monte Carlo, in order to perform different cross checks.

4.1.1 Blind Analysis

The fits to data were performed blind in order to avoid possible experimentalists' bias [45]. We used standard *BABAR* blinding tools: the fit results were hidden by an arbitrary offset determined by a user-specified keyword. We are able to proceed with the systematic studies (see Section 4.2), while keeping the values of S and C blinded, using this method. Once the analysis method for extracting S and C has been reviewed and finalized, we can proceed to unblind.

4.1.2 Fit of the Data

The results of the unblind signal $K_L^0 + B_{flav}$ fit with all floating parameters are :

$$S = -0.694 \pm 0.061, \tag{4.1}$$

$$C = -0.033 \pm 0.050. \tag{4.2}$$

The correlation between these two parameters is about +3%.

As a cross-check, we also performed the fit using $\sin 2\beta$ and $|\lambda|$ (recall Equations 1.47, 1.48 and 1.112) as fitted parameters, and found

$$\sin 2\beta = 0.694 \pm 0.061, \tag{4.3}$$

$$|\lambda| = 1.035 \pm 0.051. \tag{4.4}$$

The correlation between these two parameters is about −1%.

Table 4.1 shows the results of the fit in various subsets for S and C. Figures 4.1 and 4.2 show the likelihood fit results projection on the Δt distribution of the K_L events for each tagging category. Figure 4.3 shows the $B^0/\overline{B}^0$-tagged events asymmetry distributions and their PDF projections.

A comparison of the results of this iteration of the analysis (2008) and the results of the 2006 analysis [10] is available in Appendix C.

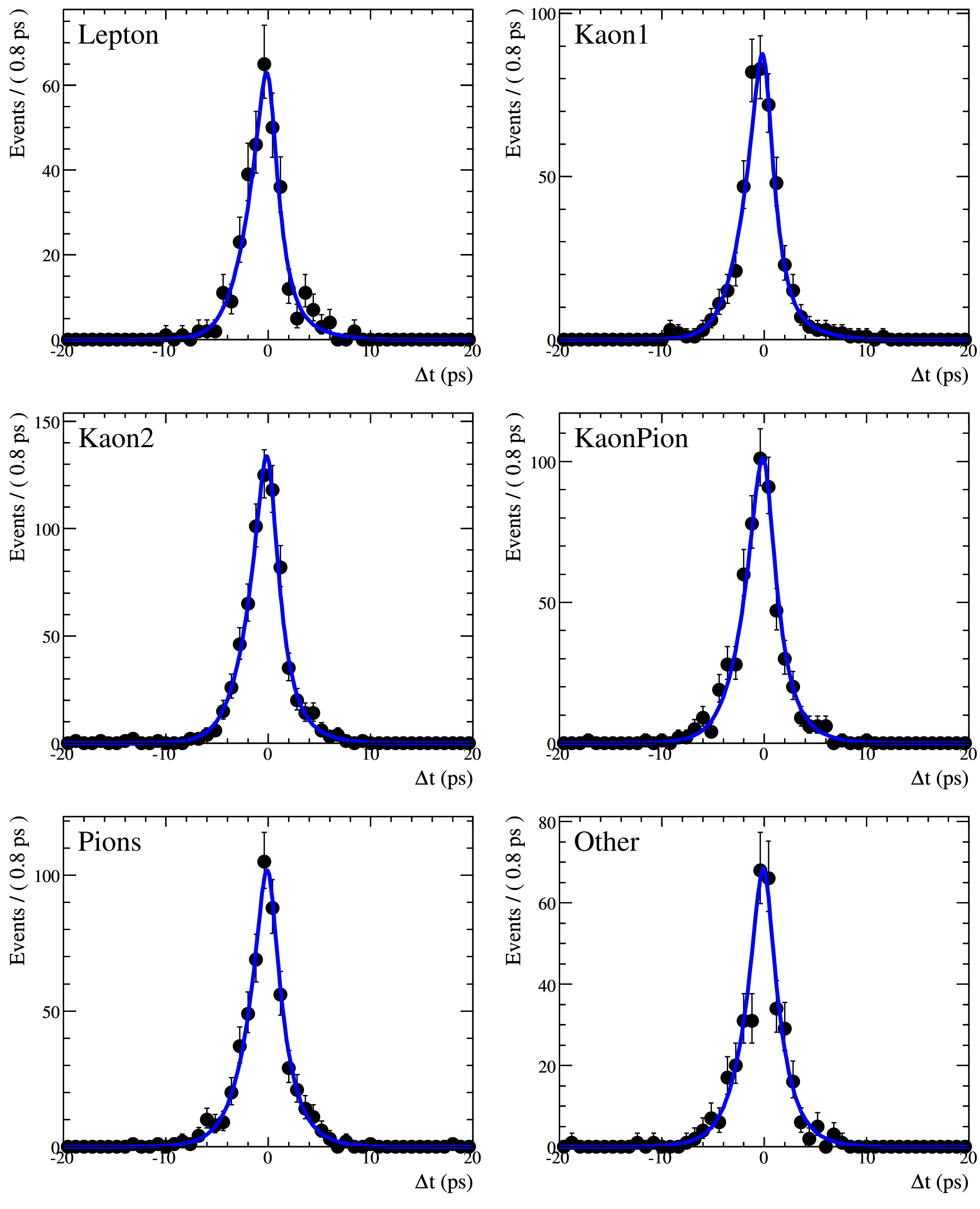

Figure 4.1: K_L^0 PDF projections on the Δt distributions for B^0-tagged events by tagging category.

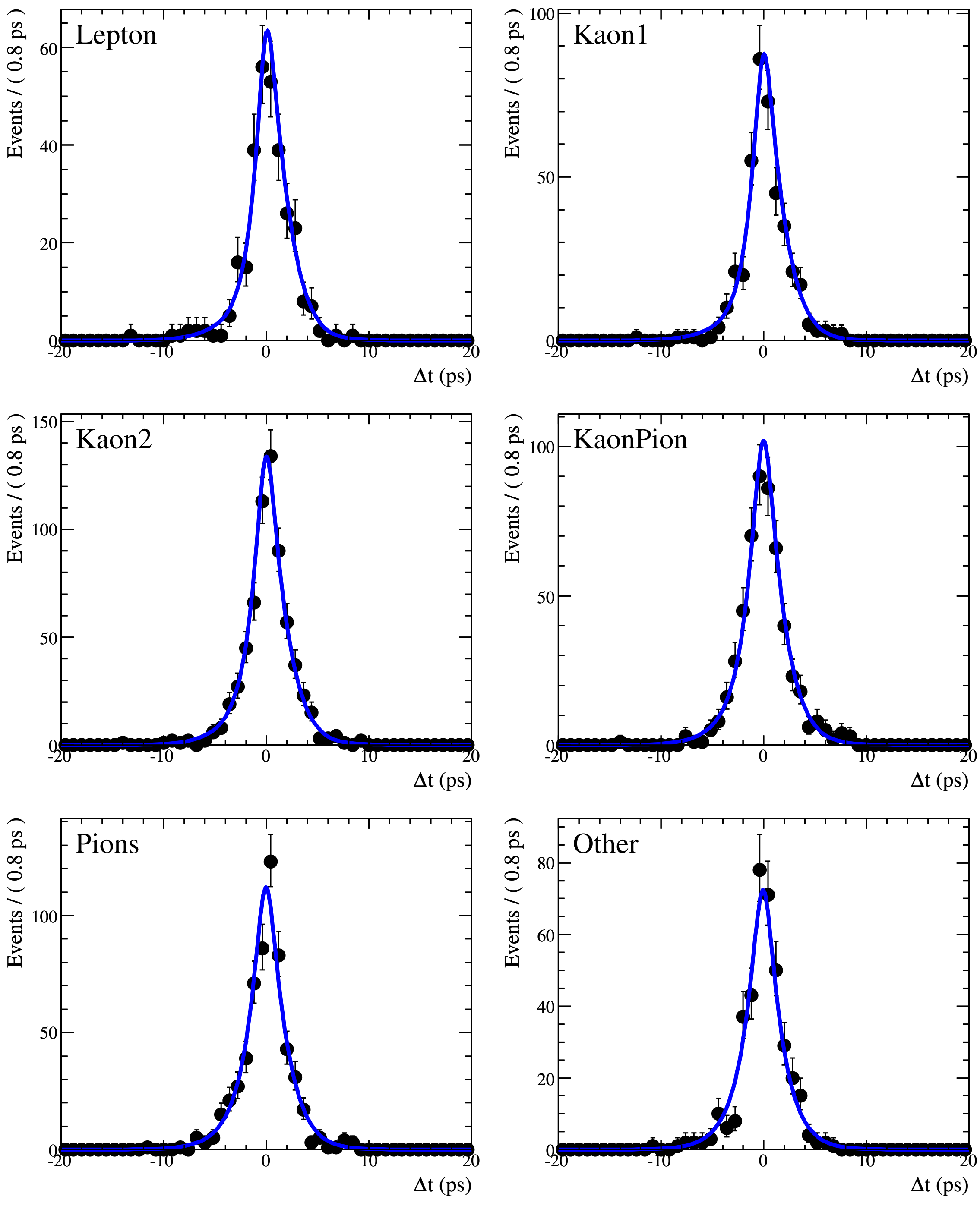

Figure 4.2: K_L^0 PDF projections on the Δt distributions for $\overline{B}^0$-tagged events by tagging category.

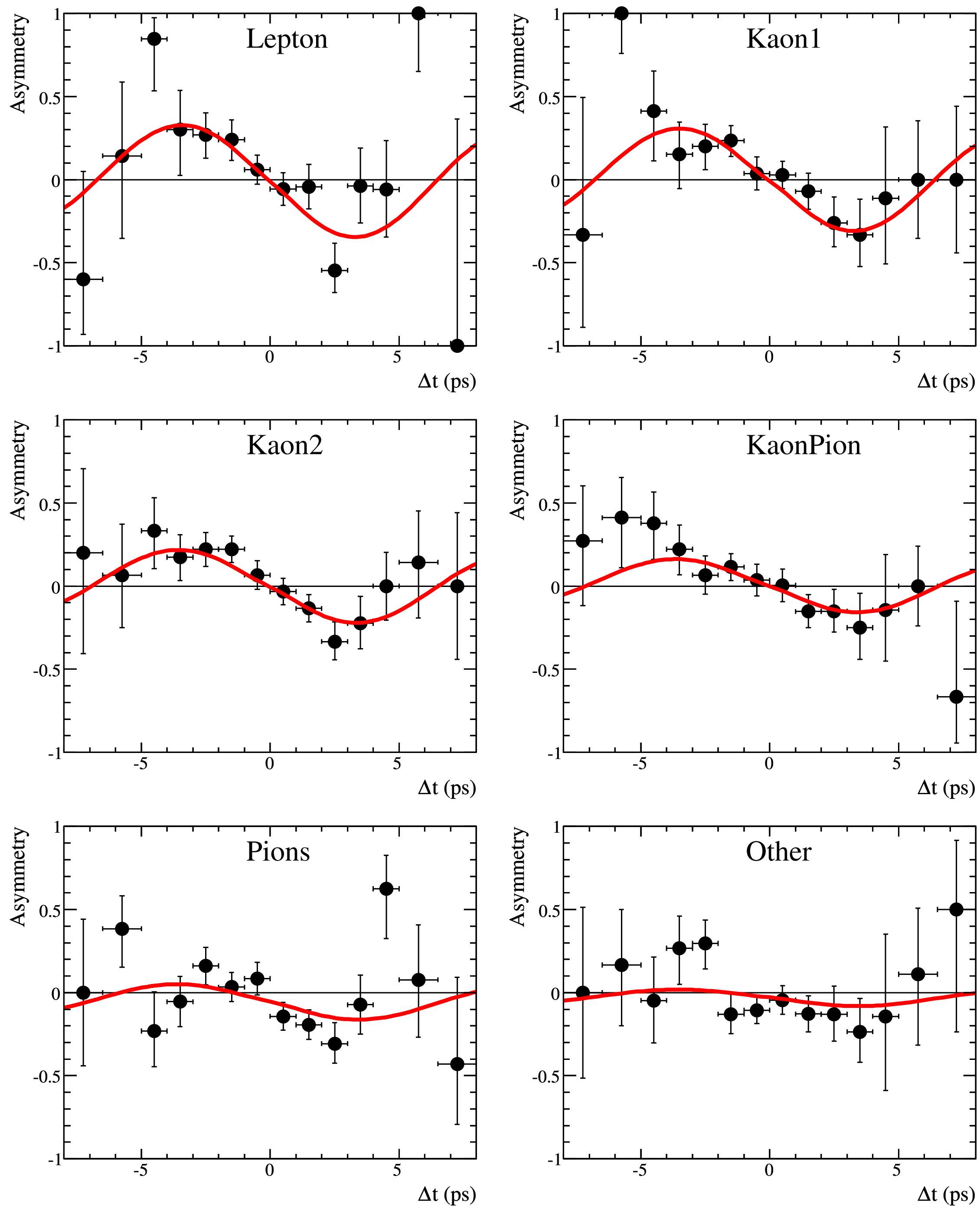

Figure 4.3: CP asymmetries (as defined in Equation 3.10) and PDF projections for K_L^0 mode separately by tagging category. The error bars are binomial.

Sample	S	C
$J/\psi K_L$	**0.694 ±0.061**	**-0.033±0.050**
Lepton	0.663 ± 0.116	-0.035 ± 0.084
Kaon1	0.556 ± 0.113	-0.096 ± 0.081
Kaon2	0.753 ± 0.124	-0.031 ± 0.089
KaonPion	0.896 ± 0.189	$+0.013 \pm 0.136$
Pion	0.840 ± 0.284	$+0.016 \pm 0.195$
Other	2.073 ± 0.755	$+0.299 \pm 0.515$
Run1+2 Kl-EMC $J/\psi \to e^+e^-$	1.540 ± 0.380	0.180 ± 0.253
Run1+2 Kl-IFR $J/\psi \to e^+e^-$	0.549 ± 0.262	-0.229 ± 0.202
Run1+2 Kl-EMC $J/\psi \to \mu^+\mu^-$	0.920 ± 0.215	-0.098 ± 0.188
Run1+2 Kl-IFR $J/\psi \to \mu^+\mu^-$	0.924 ± 0.268	0.084 ± 0.195
Run3+4 Kl-EMC $J/\psi \to e^+e^-$	0.772 ± 0.228	-0.154 ± 0.173
Run3+4 Kl-IFR $J/\psi \to e^+e^-$	0.632 ± 0.224	-0.032 ± 0.174
Run3+4 Kl-EMC $J/\psi \to \mu^+\mu^-$	0.446 ± 0.206	-0.012 ± 0.158
Run3+4 Kl-IFR $J/\psi \to \mu^+\mu^-$	0.472 ± 0.245	-0.068 ± 0.169
Run5 Kl-EMC $J/\psi \to e^+e^-$	0.654 ± 0.212	-0.233 ± 0.167
Run5 Kl-IFR $J/\psi \to e^+e^-$	0.492 ± 0.268	-0.025 ± 0.173
Run5 Kl-EMC $J/\psi \to \mu^+\mu^-$	0.994 ± 0.194	0.139 ± 0.154
Run5 Kl-IFR $J/\psi \to \mu^+\mu^-$	0.516 ± 0.216	0.046 ± 0.166
Run1-5 Kl-EMC $J/\psi \to e^+e^-$	0.863 ± 0.136	-0.090 ± 0.109
Run1-5 Kl-IFR $J/\psi \to e^+e^-$	0.571 ± 0.148	-0.102 ± 0.128
Run1-5 Kl-EMC $J/\psi \to \mu^+\mu^-$	0.760 ± 0.122	0.015 ± 0.100
Run1-5 Kl-IFR $J/\psi \to \mu^+\mu^-$	0.595 ± 0.141	0.083 ± 0.107
Run6 Kl-EMC $J/\psi \to e^+e^-$	0.365 ± 0.328	0.090 ± 0.231
Run6 Kl-IFR $J/\psi \to e^+e^-$	0.707 ± 0.264	-0.033 ± 0.209
Run6 Kl-EMC $J/\psi \to \mu^+\mu^-$	0.509 ± 0.297	-0.018 ± 0.235
Run6 Kl-IFR $J/\psi \to \mu^+\mu^-$	0.932 ± 0.239	-0.406 ± 0.186
Run1-6 Kl-EMC $J/\psi \to e^+e^-$	0.779 ± 0.126	-0.049 ± 0.099
Run1-6 Kl-IFR $J/\psi \to e^+e^-$	0.601 ± 0.128	-0.140 ± 0.099
Run1-6 Kl-EMC $J/\psi \to \mu^+\mu^-$	0.721 ± 0.113	0.009 ± 0.092
Run1-6 Kl-IFR $J/\psi \to \mu^+\mu^-$	0.668 ± 0.124	0.007 ± 0.094

Table 4.1: Result of fitting for CP asymmetries in the $J/\psi K_L$ only configuration split by K_L^0 reconstruction mode.

4.2 Systematic Errors

In this section, we describe the procedure and results of the systematic error evaluation. They are calculated for S and C, and for the five fit configurations : $J/\psi K^0$ only (K_S^0+ K_L^0), $J/\psi K_L^0$ only, $J/\psi K_S^0$ only, all the modes together and for each of the

7 charmonium modes separately.

Some systematic uncertainties are specific to the $J/\psi\, K_L^0$, while some affect all modes.

4.2.1 Systematic Uncertainties Specific to the $J/\psi\, K_L^0$ Mode

The following does not affect the fits to $J/\psi\, K_L^0$ only, but does affect all fits that include the $J/\psi\, K_L^0$ sample.

Measured Sample Composition from ΔE Fit

The relative amount of signal, inclusive J/ψ background and non-J/ψ background is determined from a binned likelihood fit of the ΔE spectrum, which is described in Section 3.4. There are two statistical sources of uncertainty associated with the sample fractions from the ΔE fit that must be taken into account: the statistical error reported by the fit (data statistics) and the statistical error from the finite size of the Monte Carlo sample used to make the signal and inclusive J/ψ background templates (MC statistics).

The uncertainty from the MC statistics was evaluated by performing the ΔE fit 100 times where, for each fit, the height of each template bin was chosen randomly from a Poisson distribution with a mean equal to the nominal bin height for the template histogram before renormalization. The covariance matrix for the ΔE fit fractions was computed from the results of these 100 fits and then combined with the MINUIT [46] covariance matrix from the nominal ΔE fit describing uncertainty from the data statistics. This procedure was done for each flavor tagging category separately. The systematic errors on S and C were evaluated by varying the fractions with correlated Gaussian random numbers using the total covariance matrix (combining data and

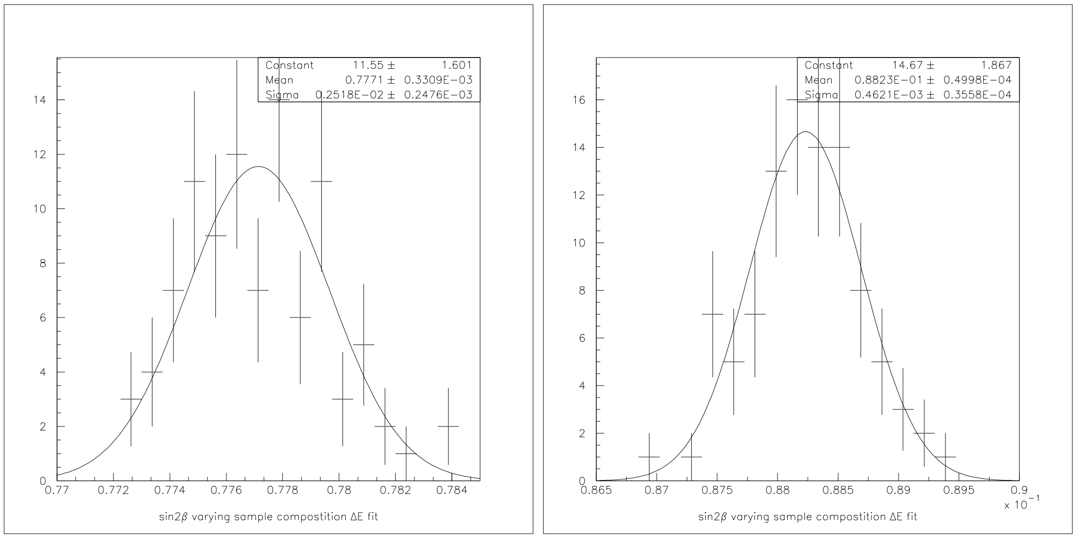

Figure 4.4: S(left) and C(right) distributions obtained while evaluating the sample composition systematic error.

MC statistics) for each tagging category. The gaussian widths of the resultant S and C distributions are taken as systematic errors. The corresponding distributions are shown in Figure 4.4 for S and C in the global fit.

Branching Fractions

The branching fractions for the relevant $J/\psi X$ modes were all varied by either their measured error or conservative estimates. The ΔE fit for the sample composition was redone for each variation.

Assumed CP Content of Background

The effective CP eigenvalue of most of the components in the fit is known. The cases where it is not are:

- $\boldsymbol{B^0 \to J/\psi\, K^{*0}; K^{*0} \to K_L^0 \pi^0}$: We use an effective CP derived from Ref. [44], which is -0.504 ± 0.033.

- **Non-itemized $\boldsymbol{J/\psi}$ X background**: Of the decay modes in this category, roughly 15% have known CP violation properties. This gives a net CP of +0.036 in the EMC and −0.003 in the IFR. If we assume that the branching fractions of the rest of the modes in the inclusive J/ψ background have an uncertainty of 50%, we get a variation of 0.018 to 0.054 for the effective CP eigenvalue of the $J/\psi\, X$ background in the EMC, and -0.0045 to -0.0015 in the IFR.

- **Non-$\boldsymbol{J/\psi}$ background**: We assume the net CP to be 0 and vary it by ±0.25.

Shape of ΔE Distributions

To evaluate our sensitivity to the shape of the ΔE PDFs (see Section 3.4), we performed the following variations:

- Change the additional ΔE smearing by ±0.45 MeV with respect to the nominal 1.1 MeV.

- Change the ΔE shift by ±0.25 MeV with respect to the nominal 0.5 MeV.

Reweighting of Monte Carlo Events

We do not believe that the Monte Carlo gives an accurate measure of the absolute K_L reconstruction efficiency. If the efficiency in the Monte Carlo is not correct, the composition of the inclusive J/ψ will be incorrect, since it is a mixture of backgrounds that do and do not contain K_Ls in the final state. We estimate the K_L reconstruction efficiency in data, relative to the Monte Carlo, by comparing the fitted $J/\psi\, K_L$ signal yield to the expected yield based on the total branching fraction, sample luminosity, and the Monte Carlo efficiency. The results of this comparison are shown in Table 4.2. To evaluate the systematic error on the data vs MC K_L efficiency in the background, we rescale the background events from B decays with a K_L in the final state by 0.82 and 1.11 for EMC and IFR samples, respectively. The ΔE sample composition fit and the resulting itemization of the inclusive J/ψ background is redone with new templates that include this adjustment.

K_L^0 type, J/ψ type	MC eff.	$N_{MCexpected}$	$N_{dataobs.}$	$R(dat/MC)$
EMC K_L^0, $J/\psi \to e^+e^-$	13.2	1596 ± 61	1353 ± 49	0.85$\pm$ 0.04
EMC K_L^0, $J/\psi \to \mu^+\mu^-$	15.5	1874 ± 72	1499 ± 50	0.80$\pm$ 0.04
IFR K_L^0, $J/\psi \to e^+e^-$	7.5	907 ± 35	1025 ± 43	1.13$\pm$ 0.06
IFR K_L^0, $J/\psi \to \mu^+\mu^-$	8.7	1052 ± 40	1149 ± 44	1.09$\pm$ 0.06

Table 4.2: The number of signal events expected, based on the MC efficiency, and the number observed in data. The number of expected events was calculated assuming a signal branching fraction of $(26 \pm 1.0) \times 10^{-6}$ per J/ψ mode and a sample of 465 million $B\bar{B}$ events.

Non-J/ψ Background in $J/\psi K_L^0$

We assume there is no CPV effects in the non-J/ψ background in the nominal fit. We evaluate the systematic error related to this assumption by doing the fit of the non-J/ψ background on the J/ψ mass sideband. We then fix the CPV parameter to the value obtained in that fit $\pm$ its statistical error.

Summary of the $J/\psi K_L^0$ Specific Systematics

Table 4.3 and 4.4 show the results for the $J/\psi K_L^0$ specific systematics for S and C, respectively. For most variations, two numbers are given. The first (second) is the shift in S or C for increasing (decreasing) the parameter in question.

Parameter	Variation	K_L^0 fit δS
Sample Composition (ΔE fit)		
Sample Composition	Total ΔE cov matrix	$\pm$ 0.0121
$J/\psi X$ branching fractions		
$B \to J/\psi K^*$	BF $\pm$ BF $\times 0.10$	-0.0012, -0.0036
$B^0 \to J/\psi K^0$	BF $\pm$ BF $\times 0.10$	-0.0022, -0.0045
$B \to J/\psi K_L^0 \pi$	BF $\pm$ BF $\times 0.50$	-0.0009, -0.0007
$B^0 \to \chi_c K_L^0$	BF $\pm$ BF $\times 0.50$	-0.0024, $+0.0004$
$B \to J/\psi X$ other	BF $\pm$ BF $\times 0.50$	$+0.0090$, $+0.0152$
Assumed CP for background		
$B \to J/\psi K^*$	-0.504 ± 0.033	-0.0022, $+0.0022$
$B \to J/\psi X$	0.018 EMC,-0.0045 IFR	-0.0023, $+0.0023$
	0.054 EMC, -0.0015 IFR	
non-J/ψ BG	0.00 ± 0.25	-0.0164, $+0.0164$
	direct CP	$+0.0011$, -0.0013
Shape of ΔE PDFs		
ΔE smearing	1.1 $\pm$ 0.45 MeV	-0.0100, $+0.0072$
ΔE shift	0.5 $\pm$ 0.25 MeV	-0.0065, $+$ 0.0102
MC K_L^0 reweighting	0.82 EMC, 1.11 IFR	-0.0008
Total	-	$\pm$ 0.0272

Table 4.3: Results of systematic error evaluation for S. The K_L^0 fit variations were done with S and C floating.

4.2.2 Systematic Uncertainties Affecting All the Modes

These errors affect all modes, including $J/\psi K_L^0$. Some effects, which affect the other modes but are not significant for $J/\psi K_L^0$, are described elsewhere [10, 38].

Mistag Differences

To determine the systematic error due to the possible mis-measuring of the signal dilutions of the CP sample, we use high statistics $B_{\rm flav}$ and $J/\psi K_s$ signal Monte Carlo samples. We fit the $B_{\rm flav}$ sample for the resolution function and tagging parameters. and then determine S and C on the $J/\psi K_s$ sample using these values. We also

Parameter	Variation	K_L^0 fit δC
Sample Composition (ΔE fit)		
Sample Composition	Total ΔE cov matrix	$\pm$ 0.00228
$J/\psi X$ branching fractions		
$B \to J/\psi K^*$	BF $\pm$ BF $\times 0.10$	+0.00024,+0.00016
$B^0 \to J/\psi K^0$	BF $\pm$ BF $\times 0.10$	+0.00008, +0.00034
$B \to J/\psi K_L^0 \pi$	BF $\pm$ BF $\times 0.50$	+0.00017,+0.00010
$B^0 \to \chi_c K_L^0$	BF $\pm$ BF $\times 0.50$	+0.00016, +0.00014
$B \to J/\psi X$ other	BF $\pm$ BF $\times 0.50$	-0.00090, -0.00115
Assumed CP for background		
$B \to J/\psi K^*$	-0.504 ± 0.033	-0.00003, +0.00003
$B \to J/\psi X$	0.018 EMC,-0.0045 IFR	-0.00007, +0.00010
	0.054 EMC, -0.0015 IFR	
non-J/ψ BG	0.00 ± 0.25	-0.00134, +0.00140
	direct CP	-0.00255, +0.00290
Shape of ΔE PDFs		
ΔE smearing	1.1 $\pm$ 0.45 MeV	+0.00116, -0.00016
ΔE shift	0.5 $\pm$ 0.25 MeV	-0.00296, + 0.00310
MC K_L^0 reweighting	0.82 EMC, 1.11 IFR	+0.00021
Total	-	$\pm$ 0.00442

Table 4.4: Results of systematic error evaluation for C. The K_L^0 fit variations were done with S and C floating.

determine the "true" mistag parameters using the Monte Carlo truth information, and then fit for S and C using those values. The difference between these fits is assigned as the systematic error due to incorrectly determined dilutions using the $B_{\rm flav}$ sample.

The Δt Resolution Function

We take into account the resolution function related systematics, in parameters that are fixed in the nominal fit. We also use alternative models and compare the fit results.

CP content of the background

Similarly to what was already discussed in the systematic error section specific to $J/\psi K^0_L$, we vary the CP content of the background components of the other modes over a wide range, in order to compensate for our limited knowledge of the background properties.

Uncertainty on Fit Bias from Monte Carlo

We check for potential bias in the fit using signal MC samples for each CP mode. The dilutions and resolution function parameters are obtained from high statistics B_{flav} Monte Carlo sample and are fixed in fits to signal MC. A very small bias in the large signal samples can be seen. We take the mean bias in the ensemble fits as the systematic uncertainty.

Tag-side Interference Effects from Doubly-CKM-Suppressed Amplitudes

The B decays that are used for flavor tagging are dominated by amplitudes containing a $b \to c\bar{u}d$ transition. However, the suppressed $\bar{b} \to \bar{u}c\bar{d}$ amplitudes can also contribute to the final states used for tagging and interfere with the $b \to c\bar{u}d$ amplitude. These two amplitudes will interfere with relative weak and strong phases from final-state interactions [47]. We include these effects as a function of these phases and conservatively use the maximum variation in S and C as our systematic error.

4.2.3 Physical Constants

We varied τ_B and Δm_d by their reported errors in [43] (see Section 3.8.3).

4.2.4 Total Systematic Error

Table 4.5 shows the values of the systematic errors on the values of S and C for the $B^0 \to J/\psi K_L^0$ decay mode. It includes all contributions described above ($J/\psi K_L^0$ specific or not). The total systematic error is obtained by adding in quadrature all

Source		$J/\psi K_L^0$
Mistag differences	S_f	0.0055
	C_f	0.0016
Δt resolution	S_f	0.0071
	C_f	0.0070
CP content	S_f	0.0044
of background	C_f	0.0107
$\Delta m_d, \tau_B, \Delta\Gamma_d/\Gamma_d$	S_f	0.0040
	C_f	0.0013
Tag-side interference	S_f	0.0014
	C_f	0.0143
Fit bias	S_f	0.0063
(MC statistics)	C_f	0.0060
$J/\psi K_L^0$ specific	S_f	0.0272
	C_f	0.0044
Total	S_f	0.0305
	C_f	0.0266

Table 4.5: Main systematic uncertainties on S_f and C_f for the $J/\psi K_L^0$ sample. For each source of systematic uncertainty, the first line gives the error on S and the second line the error on C. The total systematic error (last row) also includes smaller effects not explicitly mentioned in the table.

the numbers calculated previously. If we also include smaller effects not explicity mentioned, we find the total systematic error on the $B^0 \to J/\psi K_L^0$ mode fit only is

- 0.0305 for S,
- 0.0266 for C.

The results for all other configurations are available in Appendix D.

4.3 Conclusion

We used the full 425.7 fb^{-1} of data collected by the *BABAR* detector at the SLAC PEP-II asymmetric-energy B Factory between 1999 and 2007 and reported improved measurements of the time-dependent CP asymmetry parameters that supercede our previous results [10]. These measurements are given in terms of S and C for the first time with our data sample.

When reconstructing $B^0 \rightarrow J/\psi K^0_L$ events in this sample, we measure

$$C = -0.033 \pm 0.050(\mathrm{stat}) \pm 0.027(\mathrm{syst}), \tag{4.5}$$

$$S = -0.694 \pm 0.061(\mathrm{stat}) \pm 0.031(\mathrm{syst}). \tag{4.6}$$

We also report measurements of S and C for each of the decay modes within our CP sample, $J/\psi K^0(K^0_S + K^0_L)$ and the full CP sample. Our previous measurement [10] was the first to report the direct CP parameter for each of the seven modes, including $B^0 \rightarrow J/\psi K^0_L$. The CP violation in the $\eta_c K^0_S$ mode is established at the 5.4σ confidence level. These results are shown in Table 4.7 and summarized in Figures 4.5 and 4.6.

Figure 4.7 shows the Δt distributions and CP asymmetries in event yields between events with B^0 and $\overline{B}^0$ tags for $\eta_f = -1$ ($J/\psi K^0_S$, $\psi(2S)K^0_S$, $\chi_{c1}K^0_S$ and $\eta_c K^0_S$) and for $\eta_f = +1$ ($J/\psi K^0_L$) samples as a function of Δt, overlaid with the projection of the likelihood fit result.

This analysis was very important since it reported the last measurement of CP violation in the "Golden modes" at *BABAR*. The results provide a model independent constraint on the position of the apex of the Unitarity Triangle. They agree with pre-

Sample	$-\eta_f S$
$J/\psi\, K^0_L$ (η_f = +1)	$0.694 \pm 0.061(\text{stat}) \pm 0.031(\text{syst})$
$J/\psi\, K^0_S(\pi^+\pi^-)$	$0.662 \pm 0.039(\text{stat}) \pm 0.012(\text{syst})$
$J/\psi\, K^0_S(\pi^0\pi^0)$	$0.625 \pm 0.091(\text{stat}) \pm 0.017(\text{syst})$
$\psi(2S)K^0_S$	$0.897 \pm 0.100(\text{stat}) \pm 0.036(\text{syst})$
$\chi_{c1}K^0_S$	$0.614 \pm 0.160(\text{stat}) \pm 0.040(\text{syst})$
$\eta_c K^0_S$	$0.925 \pm 0.160(\text{stat}) \pm 0.057(\text{syst})$
$J/\psi\, K^{*0}$	$0.601 \pm 0.239(\text{stat}) \pm 0.087(\text{syst})$
$J/\psi\, K^0_S$	$0.657 \pm 0.036(\text{stat}) \pm 0.012(\text{syst})$
$J/\psi\, K^0$	$0.666 \pm 0.031(\text{stat}) \pm 0.013(\text{syst})$
Full *CP* sample	$0.687 \pm 0.028(\text{stat}) \pm 0.012(\text{syst})$

Table 4.6: Results for S obtained from fits where S and C are measured simultaneously for all seven decay modes, for $J/\psi\, K^0_S$, for $J/\psi\, K^0$ and for the full *CP* sample.

Sample	C
$J/\psi\, K^0_L$ (η_f = +1)	$-0.033 \pm 0.050(\text{stat}) \pm 0.027(\text{syst})$
$J/\psi\, K^0_S(\pi^+\pi^-)$	$0.017 \pm 0.028(\text{stat}) \pm 0.016(\text{syst})$
$J/\psi\, K^0_S(\pi^0\pi^0)$	$0.091 \pm 0.063(\text{stat}) \pm 0.018(\text{syst})$
$\psi(2S)K^0_S$	$0.089 \pm 0.076(\text{stat}) \pm 0.020(\text{syst})$
$\chi_{c1}K^0_S$	$0.129 \pm 0.109(\text{stat}) \pm 0.025(\text{syst})$
$\eta_c K^0_S$	$0.080 \pm 0.124(\text{stat}) \pm 0.029(\text{syst})$
$J/\psi\, K^{*0}$	$0.025 \pm 0.083(\text{stat}) \pm 0.054(\text{syst})$
$J/\psi\, K^0_S$	$0.026 \pm 0.025(\text{stat}) \pm 0.016(\text{syst})$
$J/\psi\, K^0$	$0.016 \pm 0.023(\text{stat}) \pm 0.018(\text{syst})$
Full *CP* sample	$0.024 \pm 0.020(\text{stat}) \pm 0.016(\text{syst})$

Table 4.7: Results for C obtained from fits where S and C are measured simultaneously for all seven decay modes, for $J/\psi\, K^0_S$, for $J/\psi\, K^0$ and for the full *CP* sample.

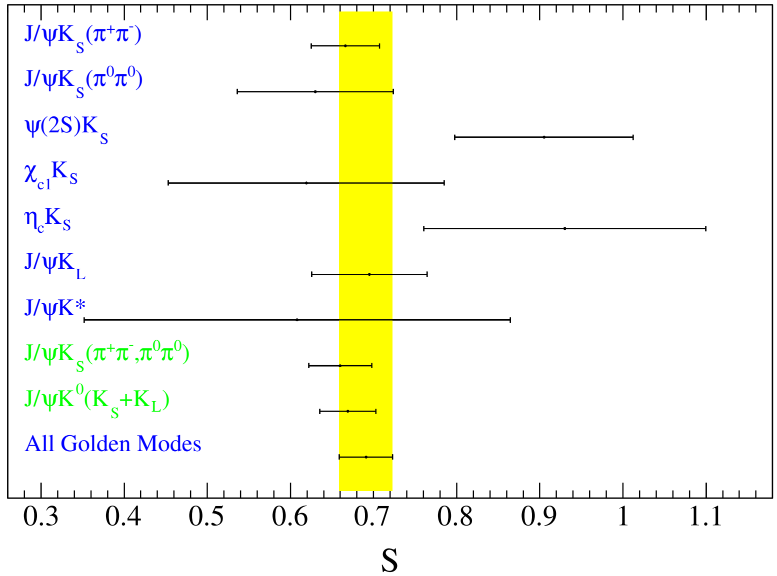

Figure 4.5: Results of the fits for S (the error bars represent the sum in quadrature of the statistical and systematic errors).

vious published results [10, 48] and with the theoretical estimates of the magnitudes of CKM matrix elements within the context of the SM [49].

The evolution of the measurement is shown in Figure 4.8 in terms of $\sin 2\beta$. The current averages of $\sin 2\beta$ and C is available from the HFAG group [50] and are shown in Figures 4.9 and 4.10. The resulting constraints on the Unitarity Triangle are compiled by the CKMFitter Group [51], using measured parameters such as $\sin 2\beta$ as input in their fit. They find

$$\bar{\rho} = 0.145^{+0.024}_{-0.034}, \tag{4.7}$$

$$\bar{\eta} = 0.339^{+0.019}_{-0.015}. \tag{4.8}$$

The updated Unitarity Triangle is shown in Figure 4.11.

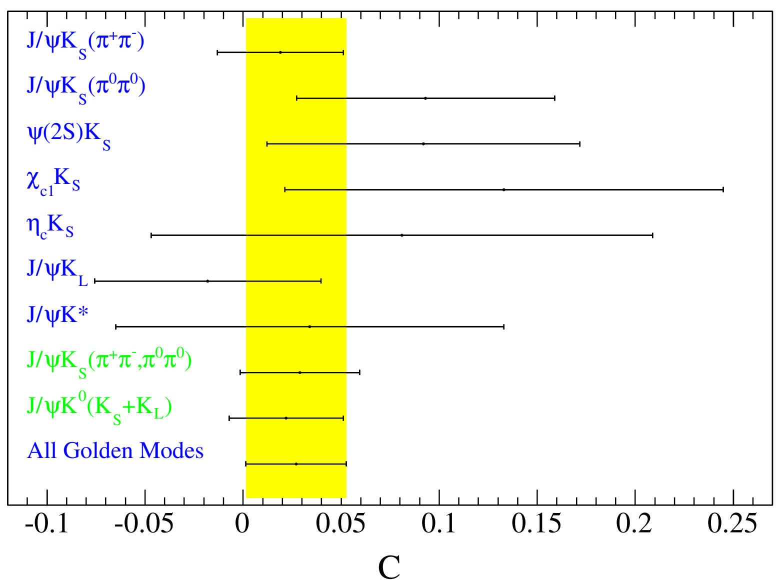

Figure 4.6: Results of the fits for C (the error bars represent the sum in quadrature of the statistical and systematic errors).

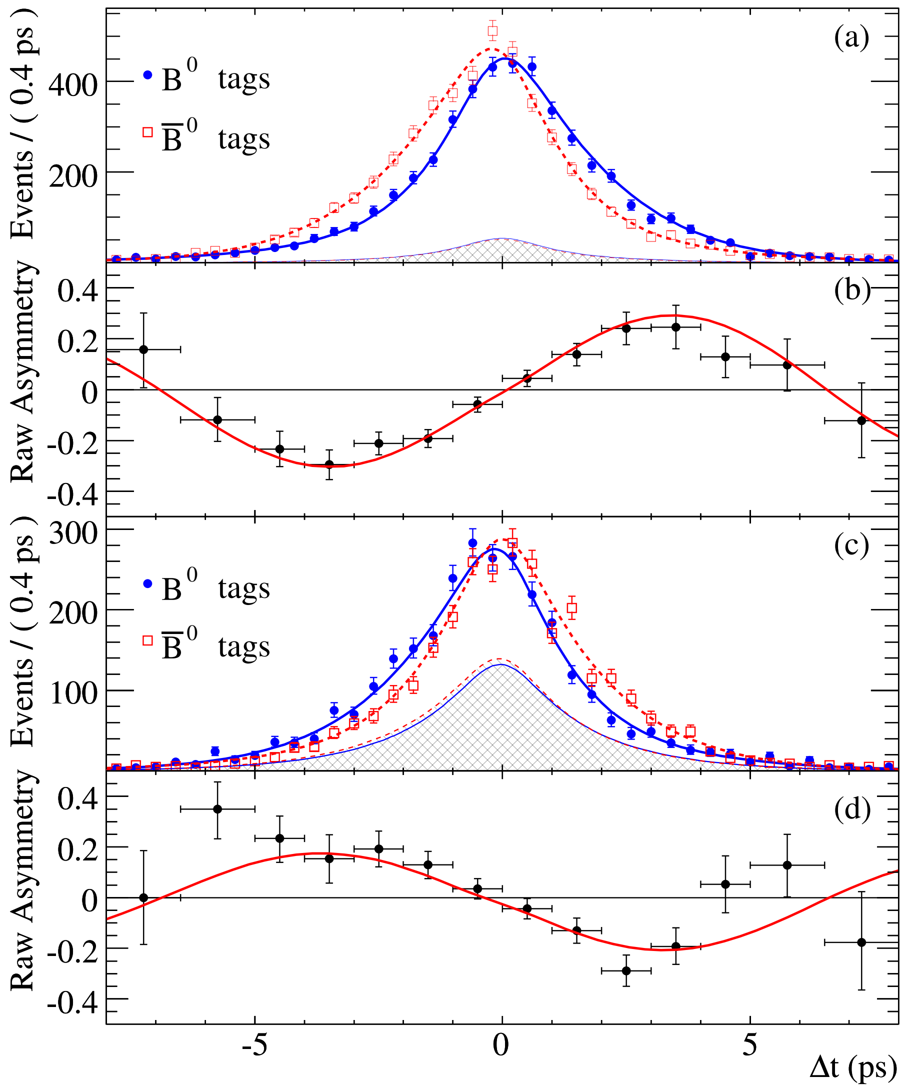

Figure 4.7: a) Number of $\eta_f = -1$ candidates ($J/\psi\, K_S^0$, $\psi(2S)K_S^0$, $\chi_{c1}K_S^0$, and $\eta_c K_S^0$) in the signal region with a B^0 tag (N_{B^0}) and with a $\overline{B}^0$ tag ($N_{\overline{B}^0}$), and b) the raw asymmetry, $(N_{B^0} - N_{\overline{B}^0})/(N_{B^0} + N_{\overline{B}^0})$, as functions of Δt; c) and d) are the corresponding distributions for the $\eta_f = +1$ mode $J/\psi\, K_L^0$. The solid (dashed) curves represent the fit projections in Δt for B^0 ($\overline{B}^0$) tags. The shaded regions represent the estimated background contributions to (a) and (c).

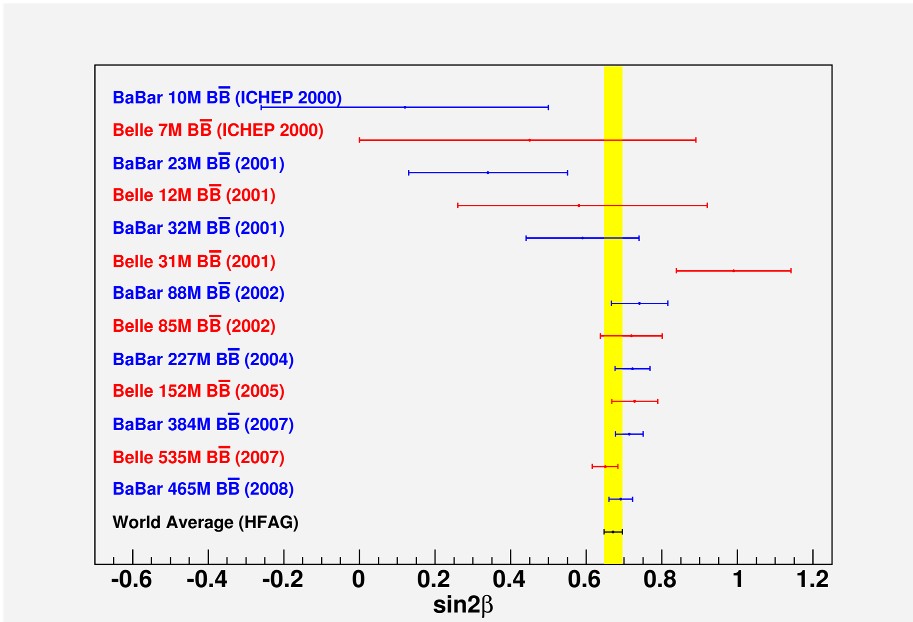

Figure 4.8: Results of the different iterations of the analysis at Belle and *BABAR*. The world average as of Summer 2008 is shown in yellow. It was calculated including the results we presented at ICHEP 2008 [11].

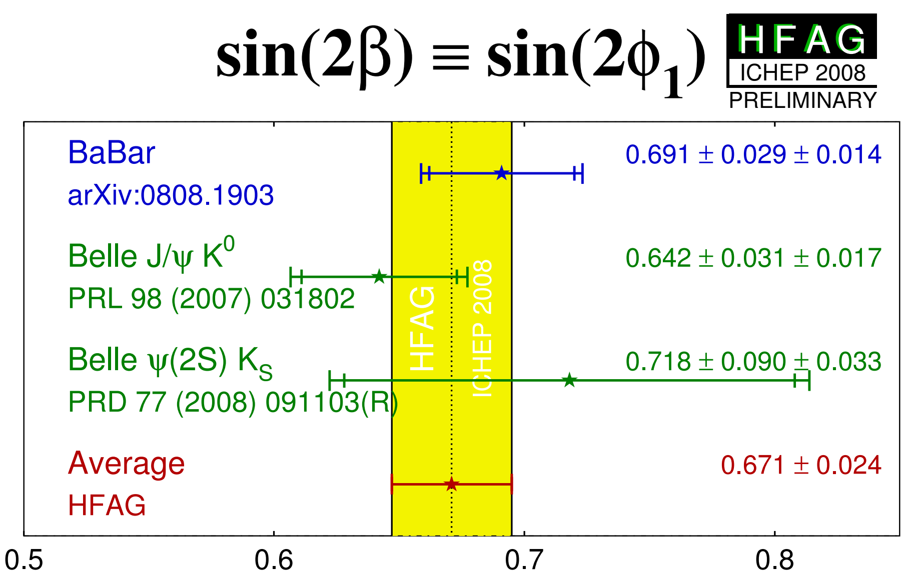

Figure 4.9: $\sin 2\beta$ average from the B factories.

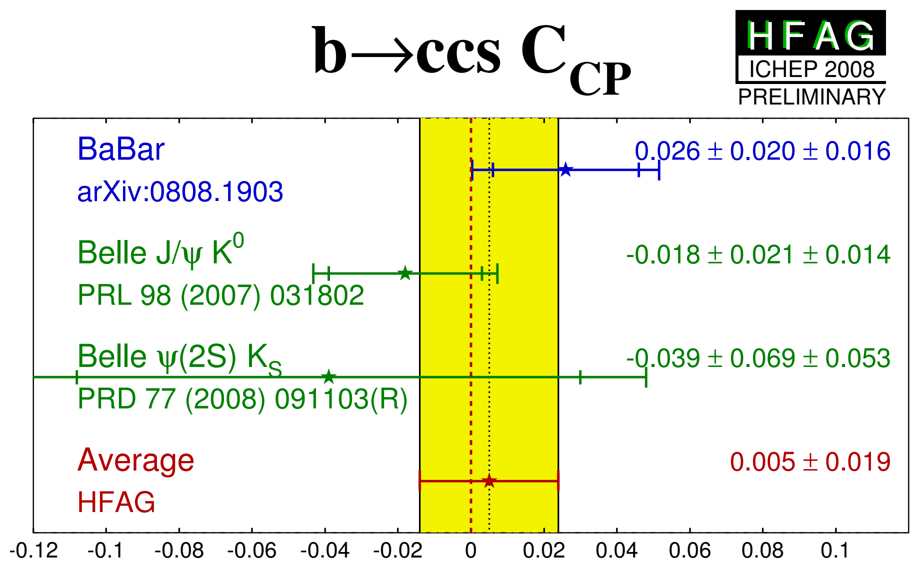

Figure 4.10: C average from the B factories.

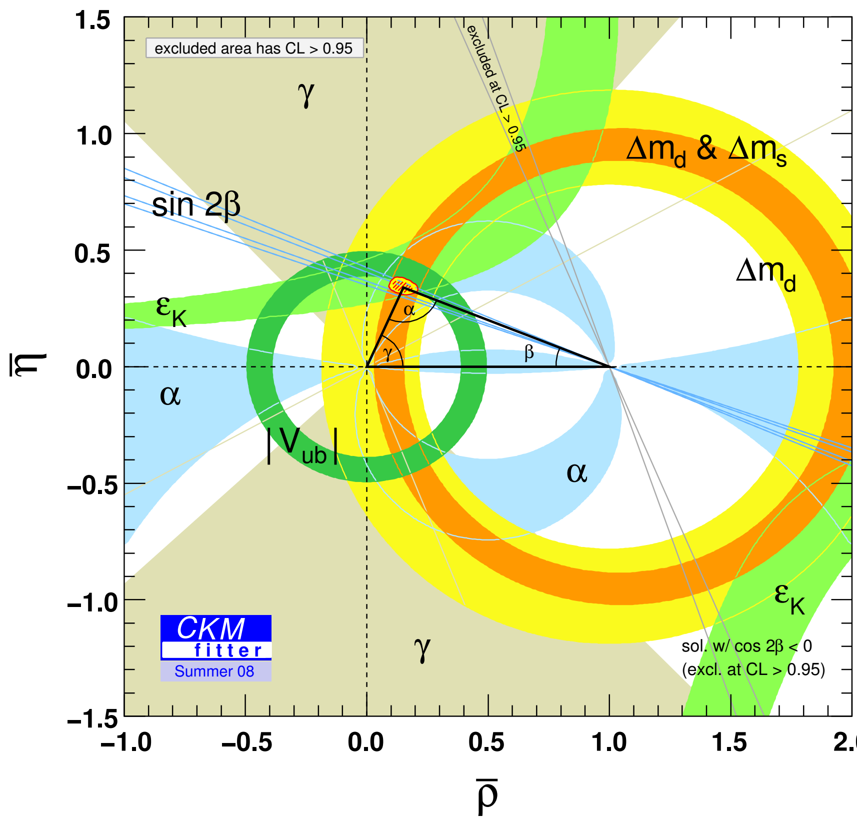

Figure 4.11: Status of the Unitarity Triangle from the CKMfitter Group.

Chapter 5

Supplement: Measurement of the $B^0 \to \bar{\Lambda} p \pi^-$ Branching Fraction

Charmless three-body baryonic B decays have recently been observed by both the BABAR and Belle collaborations [52, 53, 54]. Baryonic systems tend to be produced with a low invariant mass in a three-body decay. They all feature a peak of the baryon-antibaryon mass spectrum towards the threshold, which is believed to be a key element in the understanding of the unexpectedly high branching ratios for these decays [55, 56].

Here we are interested in the B decay to the $\bar{\Lambda} p \pi^-$ final state.[1] In the standard model this decay proceeds through the interference of tree $b \to u$ and penguin $b \to s$ amplitudes (Figure 5.1).

I worked on this analysis while in Irvine, under the supervision of Mario Bondioli, David Kirkby, Mark Mandelkern and Jonas Schultz. I contributed mostly to the selection, efficiency and ${}_s\mathcal{P}$lot studies.

[1] Charged conjugate mode is implied.

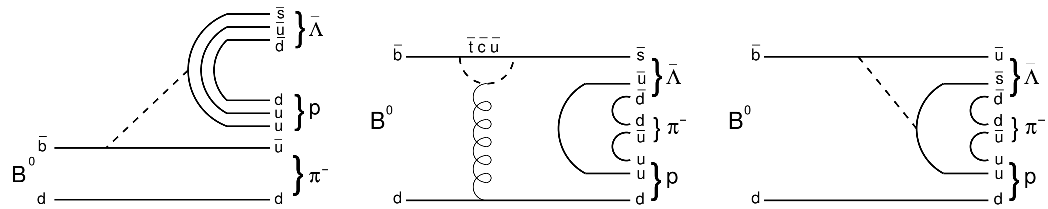

Figure 5.1: Lowest order Standard Model diagrams that contribute to the decay amplitude of the $B^0 \to \bar{\Lambda} p \pi^-$ channel.

5.1 Dataset and Selection

We used the Run 1 to 4 data sample collected by the *BABAR* detector. It consists of 210.3 fb^{-1} collected at the $\Upsilon(4S)$ resonance, which corresponds to 231.5 million $B\bar{B}$ pairs. Our Monte Carlo sample consists of 174k signal Monte Carlo events, 331 million generic $B^0\bar{B}^0$ events, 330 million generic B^+B^- events, 197 million $c\bar{c}$ events and 394 million uds events.

5.1.1 Candidate Selection

Λ Selection

Λ candidates are reconstructed from $\bar{\Lambda} \to \bar{p}\pi$ decays, which consist of a pair of charged tracks. Daughter tracks assumed to be antiprotons are required to pass a very loose particle identification (PID) selector based on a likelihood fit cut, which takes into account information from the SVT, DCH, and DIRC detectors[37]. $\bar{p}\pi$ pairs with an invariant mass in the range 1.111 – 1.121 GeV/c^2 are refit, requiring them to originate from the same vertex and constraining their combined Λ mass to the world average [43].

Proton Candidate

The proton candidates that are assumed to be daughters of the B are required to pass the same PID criteria as the proton originating from the Λ.

Pion Candidate

We require that the pion candidates that are assumed to be daughters of the B pass a loose PID selector also based on a likelihood fit cut.

5.1.2 Event Shape Discrimination

The main background arises from light quark continuum events $e^+e^- \rightarrow q\bar{q}$ ($q = u, d, s, c$). These events are typically more "jet-like" compared to their more spherical $B\bar{B}$ counterparts. Therefore, we make use of topological variables to reduce this background.

Sphericity

The sphericity can be defined as [57]

$$Spher = \frac{3 \min \sum_{i=1}^{N} \vec{p}^2_{\perp i}}{2 \sum_{i=1}^{N} \vec{p_i}^2}, \tag{5.1}$$

where $\vec{p}_{\perp i}$ is the momentum of the i-th particle perpendicular to the sphericity axis and the sphericity axis is defined to minimize the sum of the squares of the transverse momenta. For isotropic events, $Spher = 1$ and for jet-like events, $Spher = 0$. The distributions of $Spher$ for Monte Carlo and data are shown in Figure 5.2.

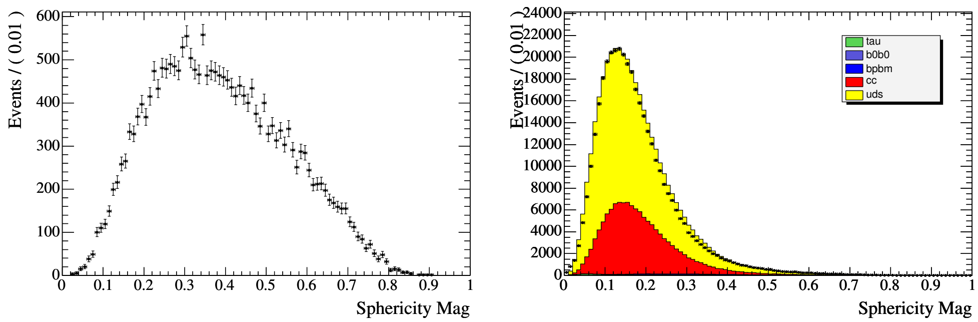

Figure 5.2: Distribution of sphericity magnitude computed on all events tracks (left), for correctly Monte Carlo matched signal candidates that pass PID cuts and for candidates on data sample (points) and cross-section weighted Monte Carlo background samples (histogram).

Legendre Moments

One can define Legendre moments as [58]

$$\mathcal{L}_n = \sum_{i=1}^{N} p_i.P_n(\theta_i), \tag{5.2}$$

where θ_i is the angle between the thrust axis and the momentum of the i-th particle, and P_n is the n^{th}- order Legendre polynomial. In the analysis, we use

$$\begin{aligned} P_0(x) &= 1 \\ P_2(x) &= \frac{1}{2}\left(3x^2 - 1\right) \end{aligned}$$

Figure 5.3 shows the distributions of 0^{th} order Legendre moment and the ratio of 2^{nd} and 0^{th} Legendre moments for Monte Carlo signal candidates that pass the PID cuts, and on data.

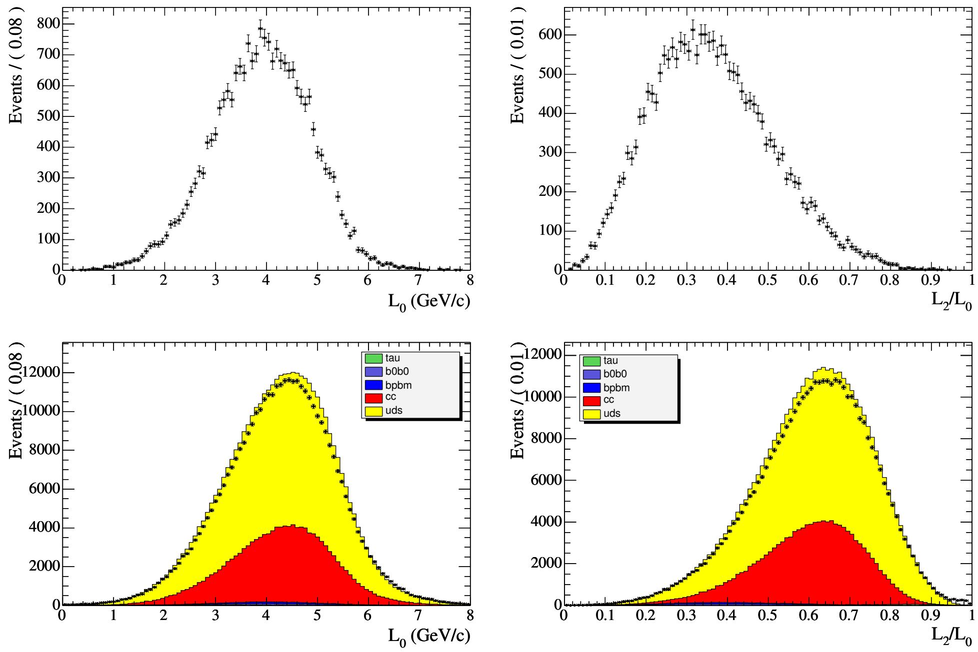

Figure 5.3: Upper plots: distribution of 0^{th} order Legendre moment (left) and the ratio of 2^{nd} to the 0^{th} (right) Legendre moments, for correctly Monte Carlo matched signal candidates that pass the proton PID cut. Lower plots: distributions for candidates on data sample (points) and cross-section weighted Monte Carlo background samples (histogram).

Event Thrust

We define the event thrust T as

$$T = \max \frac{\sum_{i=1}^{N} \vec{p_i}.\vec{n}}{\sum_{i=1}^{N} |\vec{p_i}|}, \tag{5.3}$$

where the sum is taken over the momenta $\vec{p_i}$ of the N particles and where $\vec{n}$ is a unit vector. The $\vec{n}$, for which the scalar product is maximum, is called the thrust axis of the event. The thrust axis corresponds to the direction for which the sum of the longitudinal momentum components along this axis is maximal. We define θ_{BThr} as the angle between the thrust axis of the B daughters, and the z axis. Figure 5.4 shows the distribution of $\cos\Theta_{BThr}$.

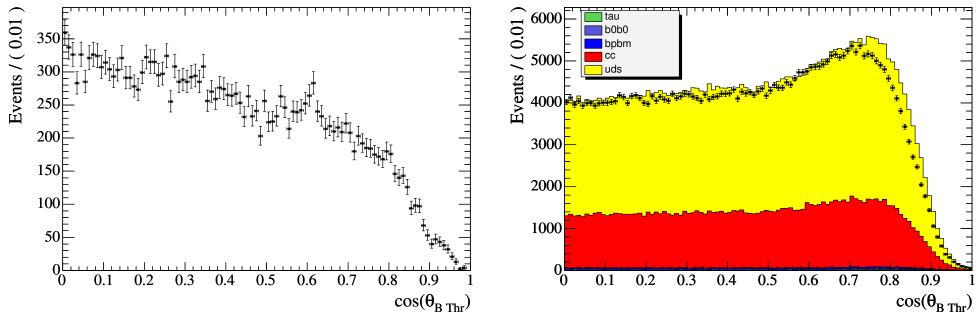

Figure 5.4: Distribution of the cosine of the angle between the thrust axis computed on B daughters and z axis, for correctly Monte Carlo matched signal candidates that survive PID cuts (left) and for candidates on data sample (points) and cross-section weighted Monte Carlo background samples (histogram) (right).

Fisher Discriminant

For each event, we linearly combine these variables in a so-called *Fisher discriminant* [59], defined as follows:

$$\mathrm{FD} = \frac{1}{6.25}\left[4.4 + 2.929 \cdot \mathrm{Spher} - 0.134 \cdot L_0 - 4.713 \cdot \frac{L_2}{L_0} - 0.857 \cdot cos(\theta_{BThr})\right],$$

where the Fisher coefficients are chosen to optimize the separation of signal and background Monte Carlo samples.

The left plot in Figure 5.5 shows Fisher discriminant distributions for signal, data and luminosity weighted background MC.

We optimize the signal selection using the significance $\frac{\mathrm{S}}{\sqrt{\mathrm{S+B}}}$ and find that it is maximized for the cut FD > 0.39.

We also use the long mean lifetime of the Λ and require that the separation of the Λ and B vertices exceeds 35 times the measurement error. The right plot of Figure 5.5 shows distributions of Λ flight length significance for signal, data and luminosity weighted background MC.

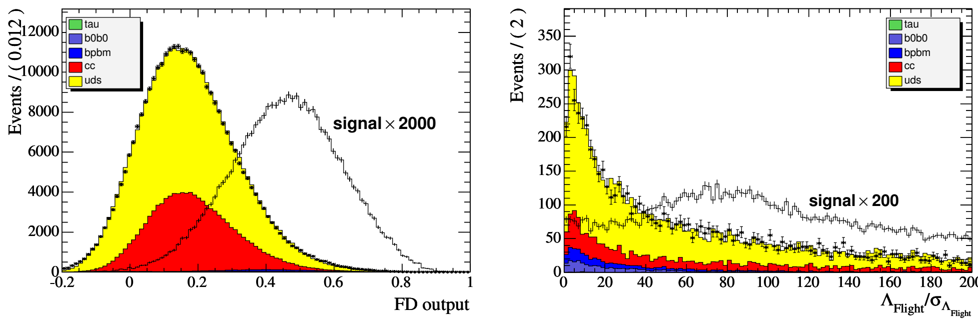

Figure 5.5: Left: Fisher discriminant distributions for candidates which pass the PID selection on data (points), rescaled MC background (colored stack) and signal (histogram) samples. Right: flight significance of Λ candidates that survive all selection cuts, for data (points), rescaled MC background (colored stack) and signal (histogram).

The kinematic constraints of B mesons produced at the $\Upsilon(4S)$ allow further separation from backgrounds using the variables m_{ES} and ΔE. As a reminder, we define

$$m_{\text{ES}} = \sqrt{\left(\frac{s}{2} + \vec{p}_i \cdot \vec{p}_B\right)^2 / E_i^2 - \vec{p}_B^{\,2}}$$

where $(E_i, \vec{p}_i)$ is the four momentum of the initial e^+e^- system and $\vec{p}_B$ the momentum of the reconstructed B candidate, both measured in the laboratory frame, and s is the square of the total available energy in the $\Upsilon(4S)$ center of mass frame. And

$$\Delta E = E_B^* - \frac{\sqrt{s}}{2}$$

where E_B^* is the B energy in the $\Upsilon(4S)$ center of mass frame. Candidates that belong to the region $|\Delta E| < 200\,\text{MeV}$, $m_{\text{ES}} > 5.2\,\text{GeV}/c^2$ are used in the fitting process.

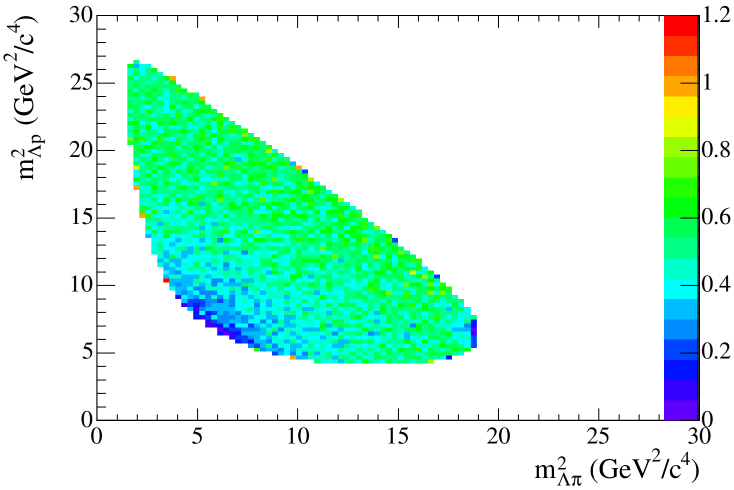

Figure 5.6: Fraction of truth matched signal candidates that pass all analysis cuts.

5.1.3 Veto on $B \to \bar{\Lambda}_c p$

The decay of $B^0 \to \bar{\Lambda}_c^- \left(\to \bar{\Lambda}\pi^-\right) p$ has the same final state as the decay we are studying, and represents the only sizable B background. The $\Lambda\pi$ system invariant mass is used to veto such background. Candidates whose reconstructed $m(\Lambda\pi)$ lies within $20\,\mathrm{MeV}/c^2$ from the nominal Λ_c mass [43] are eliminated.

5.2 Efficiency Measurement

To measure the branching ratio, we need to measure our selection efficiency as a function of position on the Dalitz plane. The distribution of MC signal reconstructed B candidates that pass all the selection cuts is shown on the Dalitz plane in Figure 5.6.

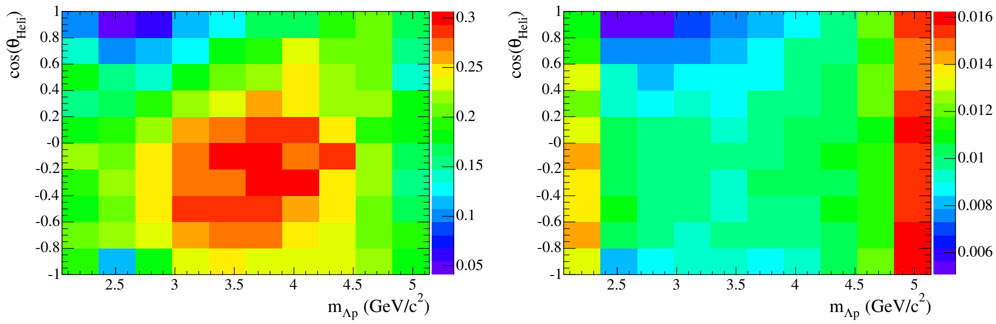

Figure 5.7: fraction of truth matched Monte Carlo reconstructed signal candidates that pass all analysis cuts as a function of square Dalitz position (left) and error on the fraction (right)

5.2.1 Efficiency on Square Dalitz Plane

In order to simplify the mapping of the reconstruction efficiency, the efficiency is parametrized with respect to $m_{\Lambda p}$ and $\cos(\theta_{\mathrm{Heli}})$, instead of the traditional $m^2_{\Lambda p}$ and $m^2_{\Lambda\pi}$. This allows us to have a rectangular kinematically allowed Dalitz region, instead of the usual oval shape. We will therefore refer to it from now on as the *square Dalitz* plane. It is divided into 10×10 rectangular boxes, where the efficiency of each box is defined as the number of reconstructed candidates divided by the number of truth ones, and is shown in Figure 5.7.

5.3 Branching Fraction Measurement

We perform a maximum-likelihood fit on m_{ES} and ΔE and use an ${}_s\mathcal{P}$lot technique [60] to determine the $m(\bar{\Lambda}p)$ distribution of events. After correcting for the non-uniform efficiency distribution, we can evaluate the $m(\bar{\Lambda}p)$-dependent differential rate, as well as the total branching fraction.

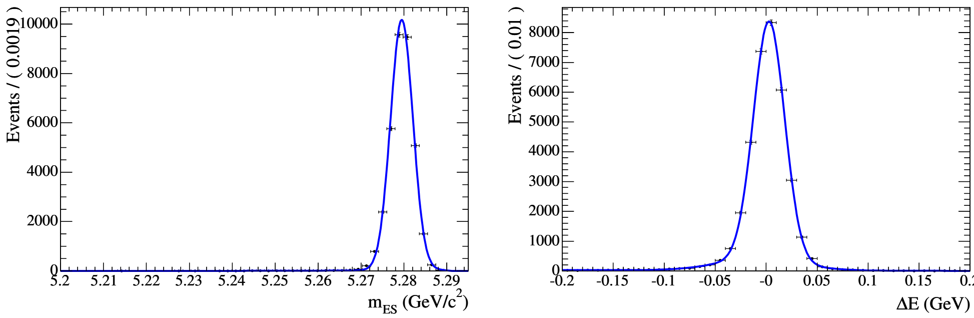

Figure 5.8: m_{ES} (left) and ΔE (right) distributions of correctly MC matched reconstructed signal candidates that pass all selection criteria, along with their respective one-dimensional PDFs.

5.3.1 Maximum Likelihood Fit

The total PDF in the ΔE-m_{ES} plane is defined as the sum of signal, background and self cross-feed components:

$$\mathcal{L} = \frac{1}{N!} e^{-(N_S + N_B + N_{Scf})} \prod_{\alpha=1}^{N} \left[N_S \mathcal{P}_S \left(\Delta E_\alpha, m_{\mathrm{ES}\alpha}\right) + N_B \mathcal{P}_B \left(\Delta E_\alpha, m_{\mathrm{ES}\alpha}\right) \right. \\ \left. + N_{Scf} \mathcal{P}_{Scf} \left(\Delta E_\alpha, m_{\mathrm{ES}\alpha}\right) \right]$$

where the product is over the N fitted events with N_S, N_B and N_{Scf} representing the number of signal, background and self cross-feed events respectively.

Self cross-feed candidates are reconstructed candidates in a signal event, which show incorrect assignment of one or more of the daughters. They can be combinations in which one of the daughter tracks is taken from the other B decay, or combinations in which two tracks, such as the B and Λ protons, are interchanged.

The PDF's can be written as the product of one-dimensional m_{ES} and ΔE PDF's:

$$\mathcal{P}_i \left(\Delta E, m_{\mathrm{ES}}\right) = \mathcal{P}_i \left(\Delta E\right) \cdot \mathcal{P}_i \left(m_{\mathrm{ES}}\right) \tag{5.4}$$

since the correlations between these two variables are small. The m_{ES} PDF is a double Gaussian for the signal component and a threshold Argus function [41] for the background. The ΔE PDF corresponds to a double Gaussian for the signal and a first degree polynomial for the background component. The self cross-feed has a peaking and a non-peaking contribution. The former is modeled by the product of a double Gaussian in ΔE and a single Gaussian in m_{ES}, while the latter is the product of a first order polynomial in ΔE and a threshold Argus function [41] in m_{ES}.

5.3.2 Event Yield Determination with ${}_s\mathcal{P}$lot Method

The so-called ${}_s\mathcal{P}$lot technique [60] is used to determine the efficiency-corrected $m(\Lambda p)$ event rate distribution necessary to measure the branching fraction. After determining all the unknown paramaters of the PDF described above using a maximum likelihood fit method, we compute the per-event s-weights:

$$ {}_s\mathcal{P}_n = \frac{\mathbf{V}_{n,S}\mathcal{P}_S + \mathbf{V}_{n,B}\mathcal{P}_B + \mathbf{V}_{n,Scf}\mathcal{P}_{Scf}}{N_S\mathcal{P}_S + N_B\mathcal{P}_B + N_{Scf}\mathcal{P}_{Scf}}, \tag{5.5} $$

where $\mathbf{V}_{nj}$ is the covariance matrix of the event yields as measured from the fit of the PDF to the data sample. An important property of ${}_s\mathcal{P}$lots is that the sum of s-weights for the signal (background) component equals the number of fitted signal (background) candidates. This method is therefore optimal to estimate the $m(\Lambda p)$ distribution, while preserving the total signal yield, given by the maximum likelihood fit. In order to retrieve the efficiency-corrected number of data sample events in a given $m(\Lambda p)$ bin m_I we use the s-weight sum:

$$ N_{m_I} = \sum_{\alpha \subset m_I} \frac{{}_s\mathcal{P}_n(\Delta E_\alpha, m_{\mathrm{ES}\alpha})}{\epsilon(m_{\Lambda p}, \cos(\theta_{\mathrm{Heli}}))}, \tag{5.6} $$

where the function $\epsilon(m_{\Lambda p}, \cos(\theta_{\mathrm{Heli}}))$ is the per-event reconstruction efficiency as measured on signal Monte Carlo events that pass all selection criteria. The error on N_{m_I} is then given by:

$$\sigma^2\left[N_{m_I}\right] = \sum_{\alpha \subset m_I} \left(\frac{{}_s\mathcal{P}_n(\Delta E_\alpha, m_{\mathrm{ES}\alpha})}{\epsilon(m_{\Lambda p}, \cos(\theta_{\mathrm{Heli}}))} \right)^2. \tag{5.7}$$

An estimate of the efficiency-corrected number of events in the sample is given by an ${}_s\mathcal{P}$lot with only a single $m(\Lambda p)$ bin or, equivalently:

$$N = \sum_{m_I} N_{m_I}, \tag{5.8}$$

and the total branching ratio is defined as:

$$\mathcal{B}\left(B \to \Lambda p \pi\right) = \frac{N}{2N_{B^0\bar{B}^0} \cdot \mathcal{B}\left(\Lambda \to p\pi\right)} \tag{5.9}$$

5.3.3 Toy Monte Carlo Validation

The validation of the maximum likelihood fit and of the ${}_s\mathcal{P}$lot method to measure the event yield is performed using a sample of Monte Carlo experiments with fully reconstructed signal events mixed with toy-generated background events. A total of 400 experiments were generated, each containing signal and background candidates Poisson distributed, with means chosen to be close to the ones expected in the Run 1 to 4 data sample.

Maximum Likelihood Fit Validation

We plot in Figures 5.9, 5.10 and 5.11 the distributions for fitted parameters as obtained by accumulating the results of all the mixed MC experiments. The right-hand plots in the same figures report pull distributions whose center and width confirm the

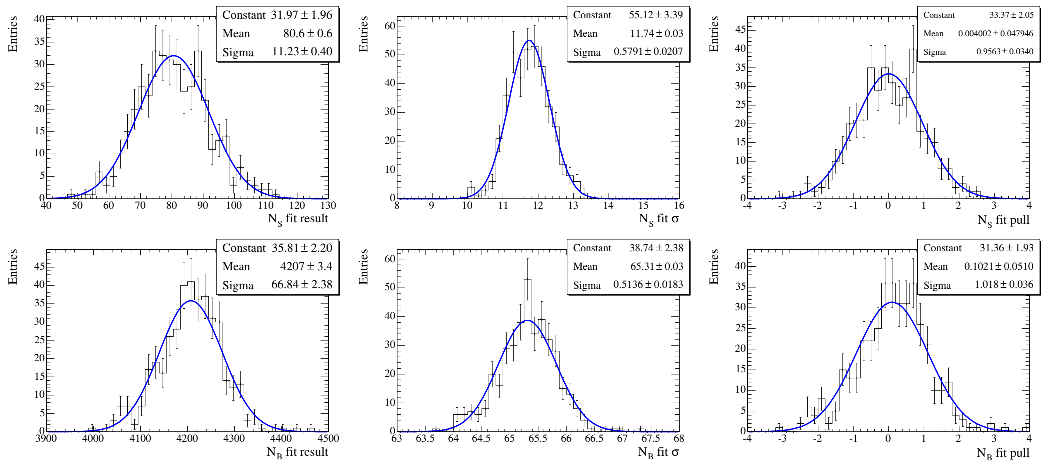

Figure 5.9: Upper: Distributions of fitted N_S (left), fitted N_S error (center) and N_S pull (right) obtained from a sample of 400 mixed Monte Carlo experiments. Lower: Distributions of fitted N_B (left), fitted N_B error (center) and N_B pull right.The number of signal and background events in each experiment are Poisson distributed with means of 80 and 4200 respectively.

correctness of the fit in the estimation of all parameters.

${}_s\mathcal{P}$lot Method Validation

Using a $m(\Lambda p)$ dependent quadratic function to model the efficiency, we can validate the ${}_s\mathcal{P}$lot method for determining the efficiency-corrected number of events.

Figure 5.13 and 5.14 shows the distributions of the measured values, errors and pulls for the $m(\Lambda p)$ bins of Figure 5.12 as fitted over the entire sample of 400 mixed MC generated experiments. The ${}_s\mathcal{P}$lot technique is able to accurately estimate the efficiency-corrected number of events with negligible bias, except for the lowest $m(\Lambda p)$ bins. This effect is included in the calculation of the systematic error.

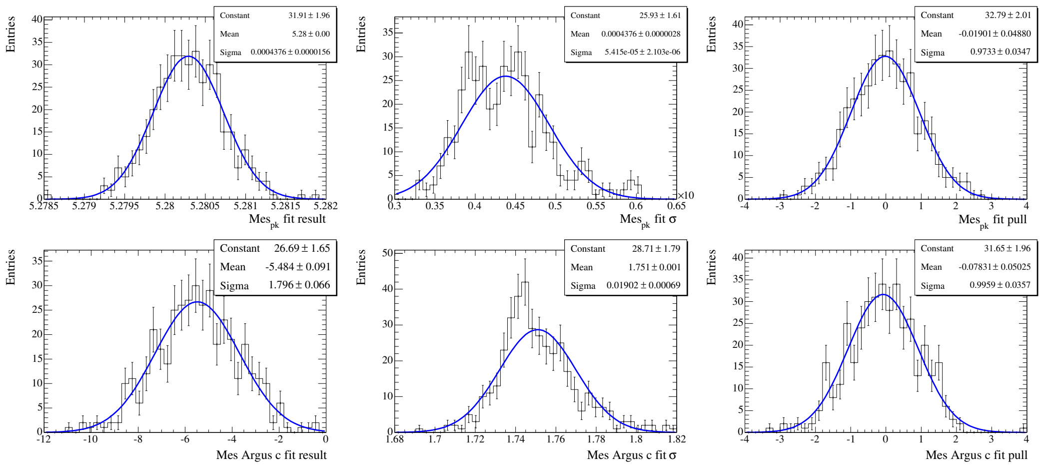

Figure 5.10: Upper plots: distributions of fitted m_{ES} μ parameter (left), its fitted error (center) and pull (right) obtained from a sample of 400 mixed Monte Carlo experiments. Lower plots: distributions for fitted m_{ES} Argus c parameter (left), its error (center) and pull (right). The expected mean values are $5.280\,\mathrm{GeV}/c^2$ for m_{ES} μ and -5.419 for the Argus c parameter.

5.4 Systematic Errors

The systematic uncertainties that affect our measurement can be organized in different categories, described in the following paragraphs.

5.4.1 Systematics Associated with Reconstruction

- **B counting**: Using the `BbkLumi` script [30], we find that the Run1-4 data sample contains a total of 231.5 ± 2.5M $B\bar{B}$ meson pairs, corresponding to a 1.1% systematic error in the luminosity measurement.

- **Tracking efficiency**: We assign the corresponding systematic errors given by the task force group dedicated to the Tracking Efficiency to each of the tracks in our decay.

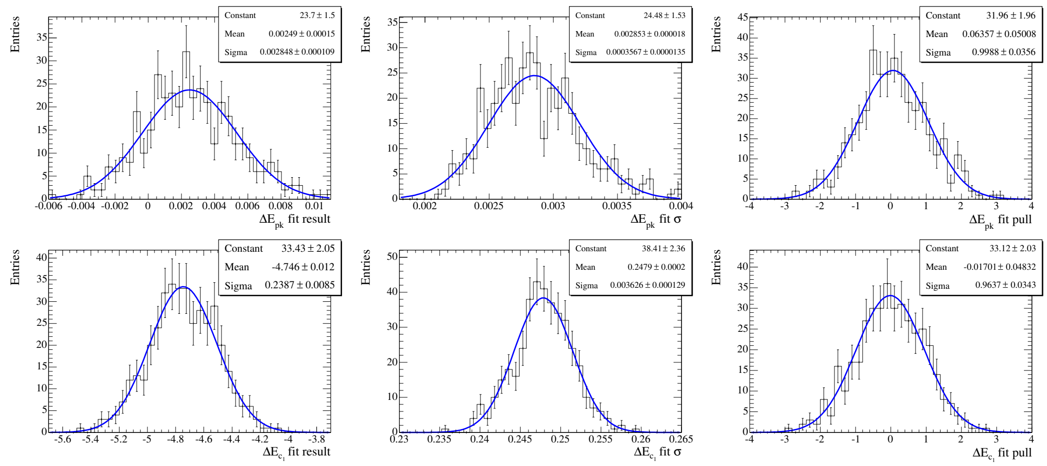

Figure 5.11: Upper plots: distributions of fitted $\mu_{\Delta E}$ parameter (left), its fitted error (center) and pull (right) obtained from a sample of 400 mixed Monte Carlo experiments. Lower plots: distributions for fitted ΔE slope c_1. The expected mean values are 2.293 MeV for $\mu_{\Delta E}$ and -4.743 for ΔE c_1.

- **Particle identification**: Likewise, the PID selector efficiencies are provided by the PID Working Group [37].

- **Monte Carlo statistics**: The determination of the efficiency across the square Dalitz plot is affected by the limited Monte Carlo sample available. The sum in quadrature of the statistical errors in the various bins is taken as a conservative total 2.0% systematic error in the reconstruction efficiency due to Monte Carlo statistics.

5.4.2 Systematic Errors Associated with Selection Cuts

A sample of $B^0 \to J/\psi K^0_S$ candidates, which has similar Fisher discriminant and B vertex probability distributions, is used to evaluate the systematic errors associated with the determination of the Fisher, B vertex probability and flight significance cut efficiencies, whereas an inclusive sample of $\Lambda \to p\pi$ is used for the Λ specific cuts. The systematic uncertainties are determined by comparing the efficiency of each cut

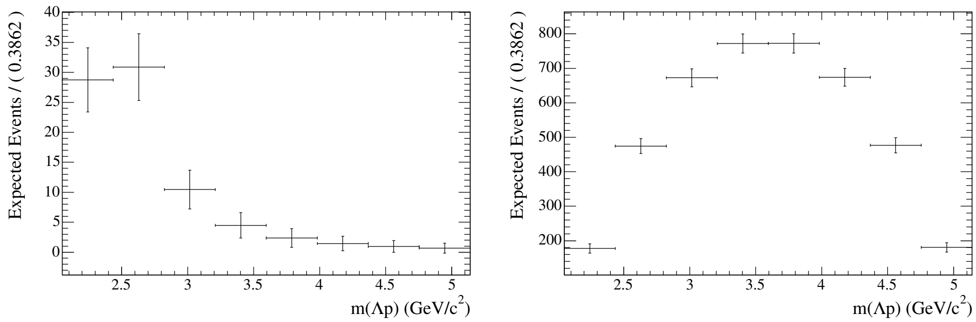

Figure 5.12: Left, mean number of signal candidates in the mixed MC experiments used to validate the ${}_s\mathcal{P}$lot method. Right, mean number of background candidates in each $m(\Lambda p)$ bin.

on data and MC.

5.4.3 Systematic Errors Associated with the Fit

- **Likelihood fixed parameters**: We vary the parameters that are kept fixed in the likelihood fit by their errors and measure the variation of the ${}_s\mathcal{P}$lot fit result.

- **Self cross-feed fraction**: We vary the self cross-feed fraction and the PDF parameters within their errors, and the variation of the ${}_s\mathcal{P}$lot fit result gives a systematic error of 0.8%.

- **Energy scale**: We vary the width of ΔE within its uncertainty and find a variation of the ${}_s\mathcal{P}$lot result of 1.7%, which is taken as systematic error.

- **${}_s\mathcal{P}$lot bias correction**: We correct the measured yields by a small bias associated with the ${}_s\mathcal{P}$lot fit found in the toy mixed MC. This bias of 0.6% is taken as contribution to the systematic.

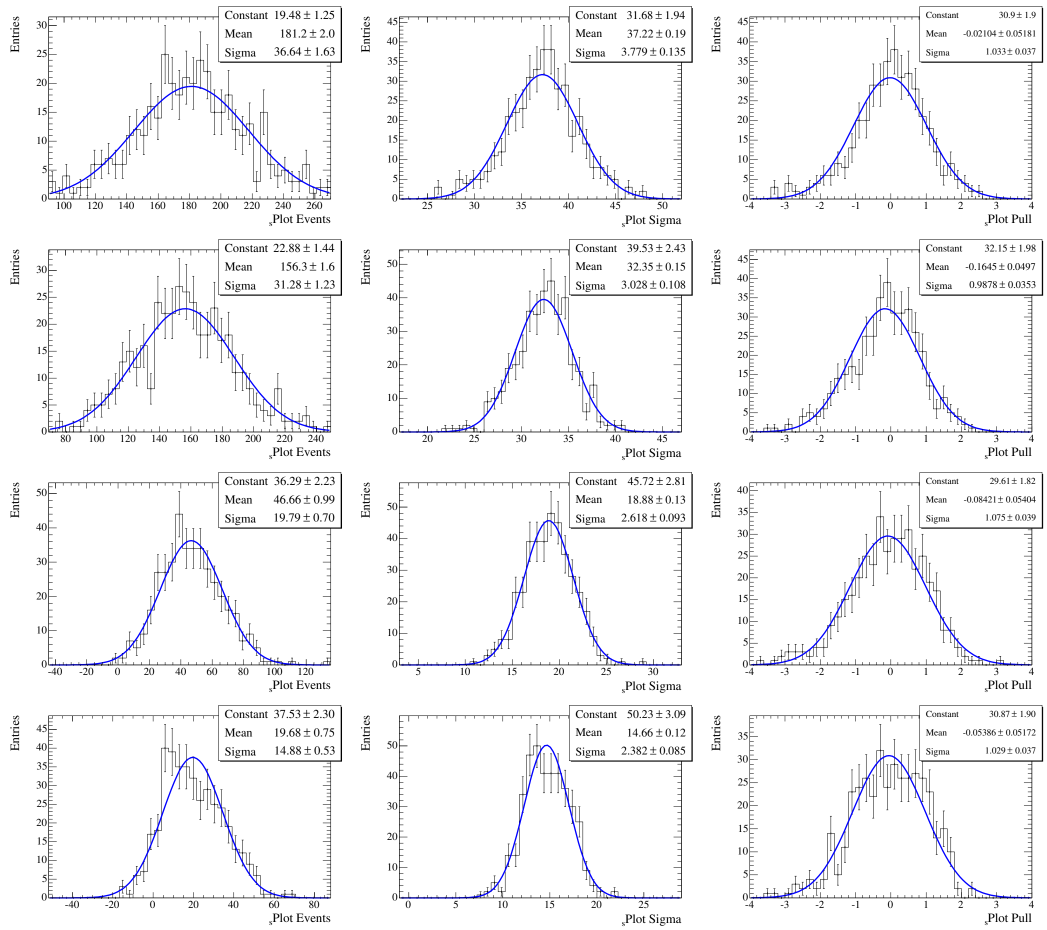

Figure 5.13: Distributions of ${}_s\mathcal{P}$lot measured, efficiency corrected events on mixed MC experiments (left), measured error (center) and pull (right) for the first four bins of Figure 5.12. The expected mean values are 159.2, 18.1, and 4.84 respectively.

5.4.4 Other Systematics

- $B^0\bar{B}^0$ **over** $B\bar{B}$ **fraction**: We assume a 50% fraction of $B^0\bar{B}^0$ over $B\bar{B}$ and quote the difference with respect to the measured value at the $\Upsilon(4S)$ [43] as a 1.4% contribution to the systematic error.

- $\Lambda \to p\pi$ **branching fraction**: We also take the uncertainty on the value of $\mathcal{B}(\Lambda \to p\pi) = 63.9 \pm 0.5\%$ [43], as a 0.8% systematic error.

A summary of all the systematic error contributions can be found in Table 5.4.4.

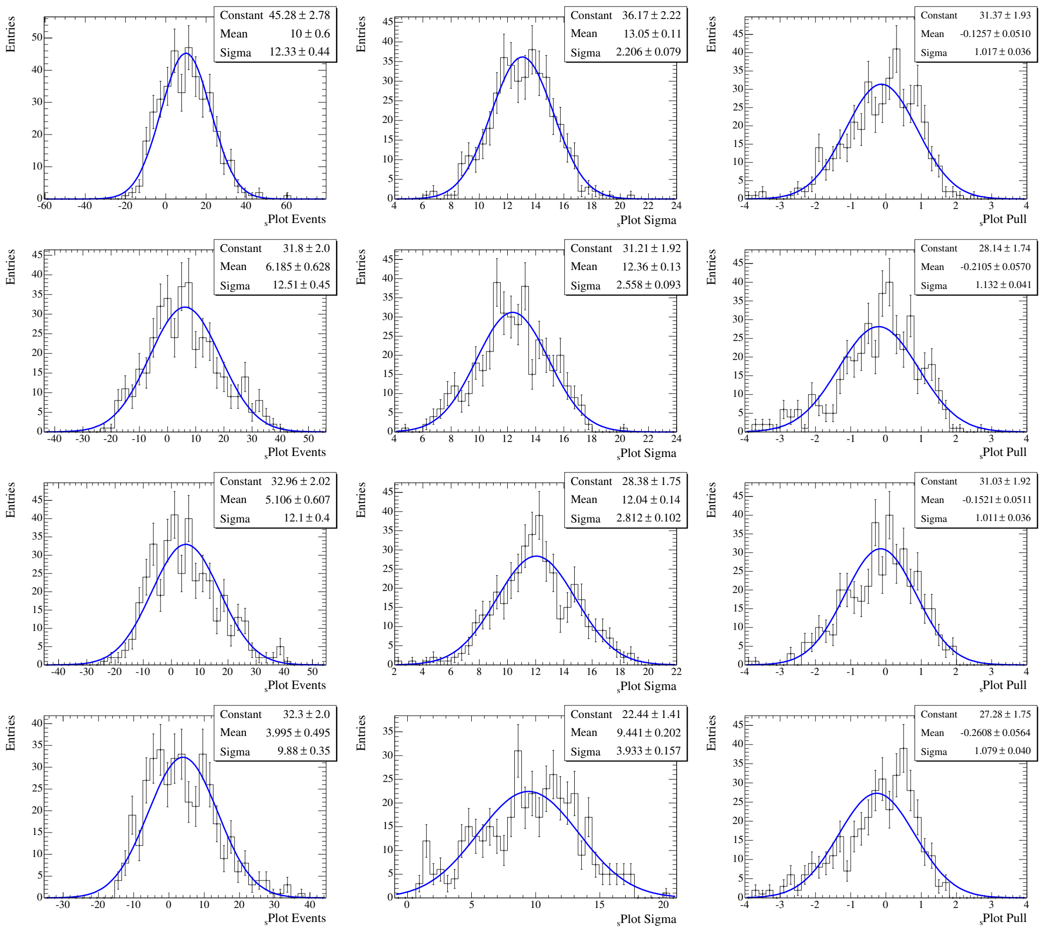

Figure 5.14: Distributions of ${}_s\mathcal{P}$lot measured, efficiency corrected events on mixed MC experiments (left), measured error (center) and pull (right) for the last four bins of Figure 5.12. The expected mean values are 159.2, 18.1, and 4.84 respectively.

5.5 Results and Conclusion

A total of 4260 candidates in the region $|\Delta E| < 200\,\mathrm{MeV}$, $m_{\mathrm{ES}} > 5.2\,\mathrm{GeV}/c^2$, $|m(\Lambda\pi) - m(\Lambda_c)| > 20\,\mathrm{MeV}/c^2$ were selected from the Runs 1 to 4 data sample and fit to the 2-dimensional m_{ES}-ΔE PDF. Figure 5.15 shows the projections of the fitted PDF on the m_{ES} and ΔE axes. Figure 5.16 shows the ${}_s\mathcal{P}$lot distributions with respect to the $m(\Lambda p)$ coordinate and, summing over the bins of the right plot, we obtain an

	source	error
Reconstruction systematics	B counting	1.1%
	Tracking efficiency	3.9%
	PID efficiency	1.4%
	MC statistics	2.0%
Selection cut systematics	Event shape cut efficiency	2.4%
	B vertex prob. cut efficiency	5.0%
	Λ flight length cut efficiency	2.8%
	Λ mass cut efficiency	2.4%
	Λ_c veto cut	0.5%
Fit systematics	Likelihood parameters	3.9%
	Energy scale	1.7%
	Self cross-feed fraction	0.8%
	${}_s\mathcal{P}$lot bias correction	0.6%
Other systematics	$\Lambda \to p\pi$ branching fraction	0.8%
	$B^0\bar{B}^0/B\bar{B}$ fraction	1.4%
Total		9.4%

Table 5.1: Breakdown of systematic uncertainties.

estimate of the total efficiency-corrected number of events:

$$N_{\text{cands.}} = 488 \pm 79$$

in the Run1-4 data sample. This corresponds to a decay branching ratio of:

$$\mathcal{B}(B^0 \to \bar{\Lambda} p \pi^-) = [3.30 \pm 0.53(\text{stat.}) \pm 0.31(\text{syst.})] \times 10^{-6}.$$

This is compatible with previous measurements made by the Belle collaboration, who found, using a $140\,\text{fb}^{-1}$ data sample [53]:

$$\mathcal{B}\left(B \to \Lambda \bar{p} \pi\right) = [3.27^{+0.62}_{-0.51}(\text{stat.}) \pm 0.39(\text{syst.})] \times 10^{-6}.$$

The efficiency corrected ${}_s\mathcal{P}$lot distribution as a function of the di-baryon invariant

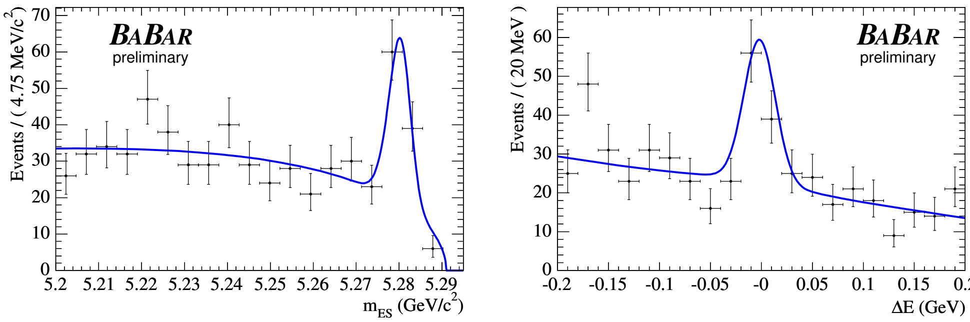

Figure 5.15: Left, m_{ES} distribution of candidates with $|\Delta E| < 27\,\text{MeV}$. Right, ΔE distribution of candidates with $m_{\text{ES}} > 5.274\,\text{GeV}/c^2$. Superimposed are projections of the 2-dimensional fit PDF onto the respective axes.

mass $m(\Lambda p)$ shows the near-threshold enhancement already seen in several baryonic B decays.

These results were reported at the 33^{rd} International Conference on High Energy Physics 2006 (ICHEP 2006) [61]. They have since been improved using 467 million $B\bar{B}$ pairs from Runs 1 through 6 along with a study of the $\bar{\Lambda}$ polarization and will soon be submitted to Physical Review D.

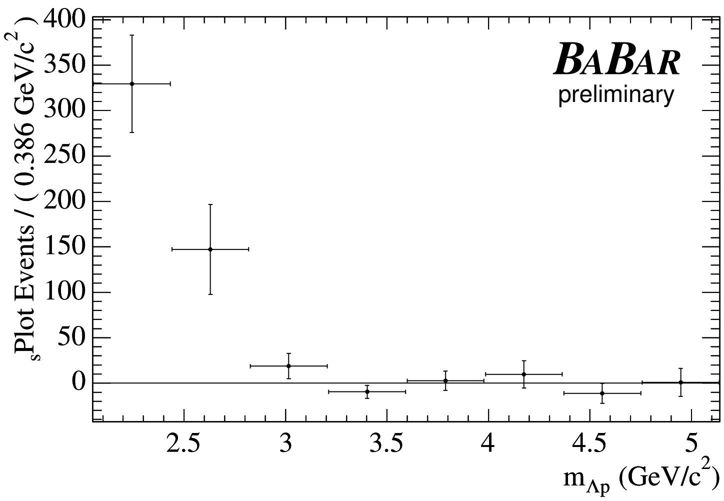

Figure 5.16: ${}_s\mathcal{P}$lot of the $m(\Lambda p)$ event distribution for the Run1-4 data sample after efficiency correction.

Appendices

A Notations and Conventions

Units

We work in natural units, i.e. defining:

$$c = 1,$$

$$\hbar = 1.$$

In this system, we have

$$[M] = [L]^{-1} = [T]^{-1}.$$

Dirac Matrices

We work in the Lorentz metric, where

$$g_{\mu\nu} = \begin{pmatrix} 1 & 0 & 0 & 0 \\ 0 & -1 & 0 & 0 \\ 0 & 0 & -1 & 0 \\ 0 & 0 & 0 & -1 \end{pmatrix}.$$

In the standard representation, the Dirac matrices are given by

$$\begin{aligned} \gamma^0 &= \begin{pmatrix} 1 & 0 \\ 0 & -1 \end{pmatrix}, \gamma^i = \begin{pmatrix} 0 & \sigma^i \\ -\sigma^i & 0 \end{pmatrix}, i = 1, 2, 3; \\ \gamma^5 &= \gamma_5 = \begin{pmatrix} 0 & 1 \\ 1 & 0 \end{pmatrix}, \sigma_{\mu\nu} = \frac{i}{2}[\gamma_\mu, \gamma_\nu]. \end{aligned}$$

σ^μs are the Pauli matrices:

$$\sigma^1 = \begin{pmatrix} 0 & 1 \\ 1 & 0 \end{pmatrix}, \sigma^2 = \begin{pmatrix} 0 & -i \\ i & 0 \end{pmatrix}, \sigma^3 = \begin{pmatrix} 1 & 0 \\ 0 & -1 \end{pmatrix}.$$

These matrices obey the following relations: $\sigma^\mu = \sigma_\mu$, $[\sigma_\mu, \sigma_\nu] = 2i\epsilon_{\mu\nu\rho}\sigma_\rho$, $\{\sigma_\mu, \sigma_\nu\} = 2\delta_{\mu\nu}$, $\sigma_\mu\sigma_\nu = \delta_{\mu\nu} + i\epsilon_{\mu\nu\rho}\sigma_\rho$.

Dirac spinors

The spinors u and v correspond to the positive and negatice solutions of the Dirac equation, respectively. For free spinors,

$$(\not{p} - m)u_s(p) = (\not{p} + m)v_s(p) = 0\,,$$

where $\not{p} = \gamma_\mu p^\mu$.

We can write them explicitly as

$$u_s(p) = \left(\frac{E+m}{2m}\right)^{1/2} \begin{pmatrix} \chi_s \\ \frac{\vec{\sigma}.\vec{p}}{E+m}\,\chi_s \end{pmatrix}$$

et

$$v_s(p) = \left(\frac{E+m}{2m}\right)^{1/2} \begin{pmatrix} \frac{\vec{\sigma}.\vec{p}}{E+m}\,\chi_s \\ \chi_s \end{pmatrix},$$

où χ_s sont les spineurs de Pauli.

They are normalized such that $\bar{u}_s(p)u_s(p) = 1$ and $\bar{v}_s(p)v_s(p) = -1$.

B ΔE yields fit

As explained in Sec 3.4, in order to determine the relative amounts of signal, inclusive-J/ψ and non-J/ψ backfround in the data sample, a binned maximum likelihood fit of the ΔE spectrum was preformed for each tagging category. Here, we present all the plots resulting from the fits. In each figure below, the upper plots correspond to the data for EMC K_L events, and the bottom plots for the IFR K_L events, respectively. The blue (dark) distribution is the non-J/ψ, which was fit to an Argus function. The red (medium) component is inclusive-J/ψ background from the Monte Carlo and the green (light) component is signal, also from Monte Carlo.

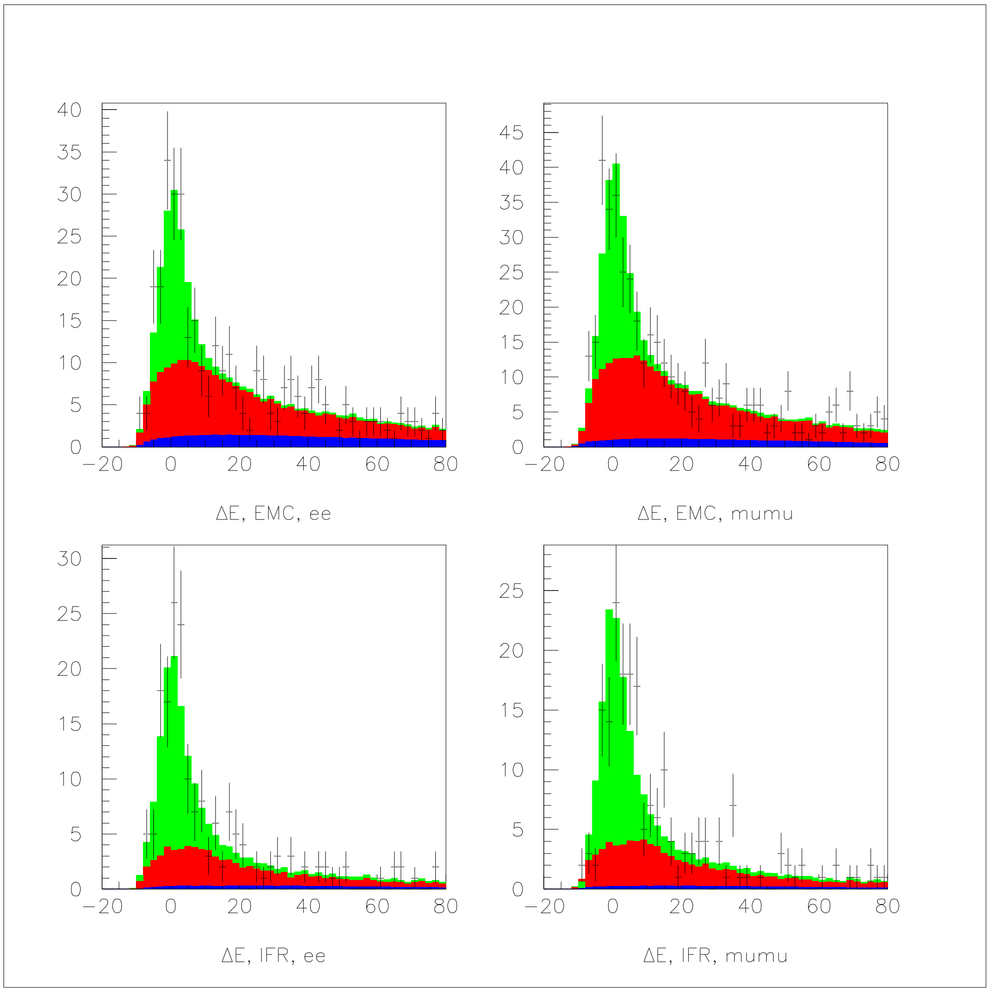

Figure B.17: Fit of the ΔE spectrum for the Lepton tagged events.

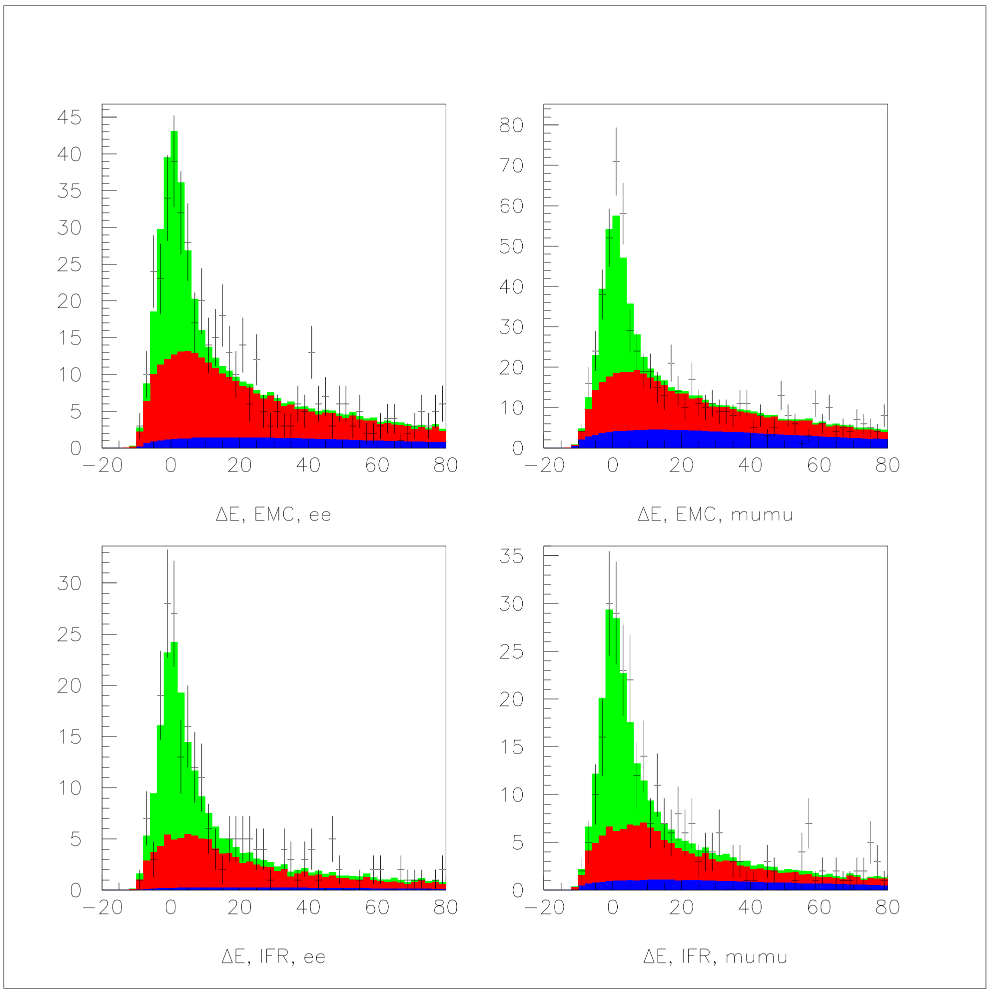

Figure B.18: Fit of the ΔE spectrum for the Kaon1 tagged events.

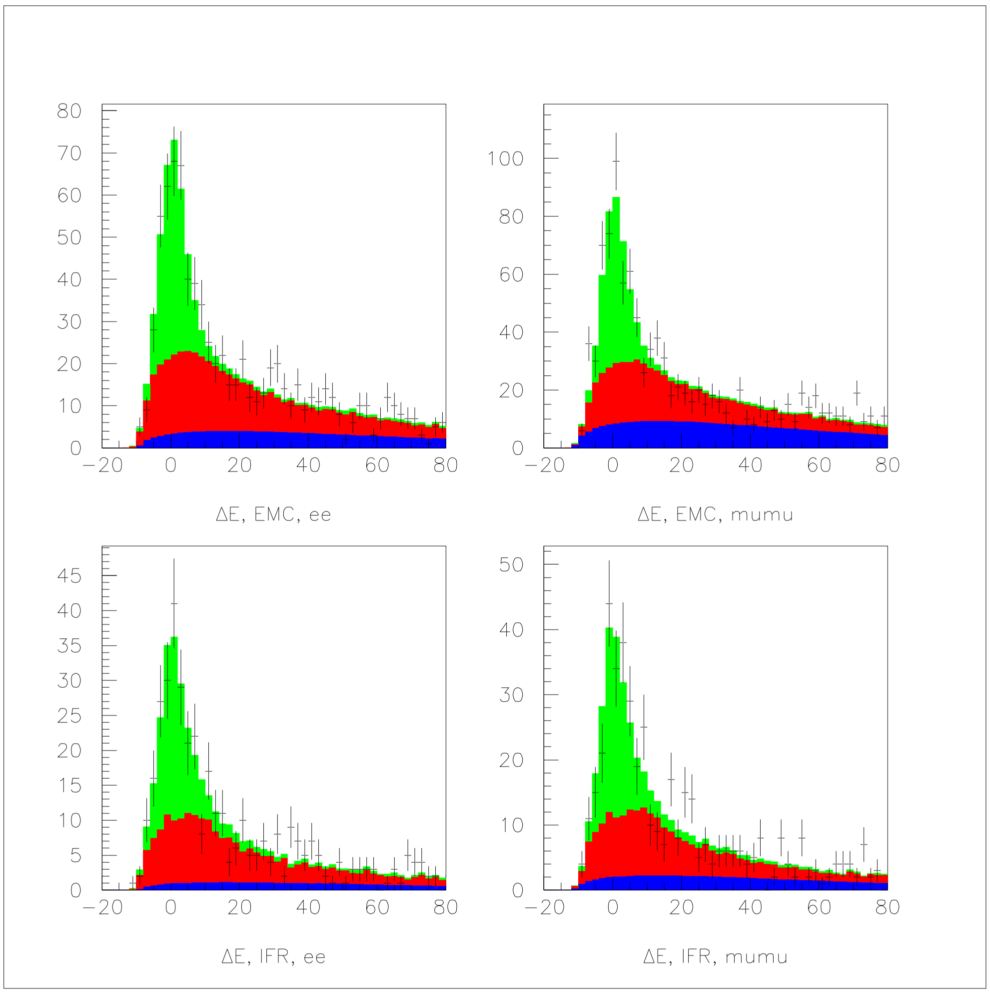

Figure B.19: Fit of the ΔE spectrum for the Kaon2 tagged events.

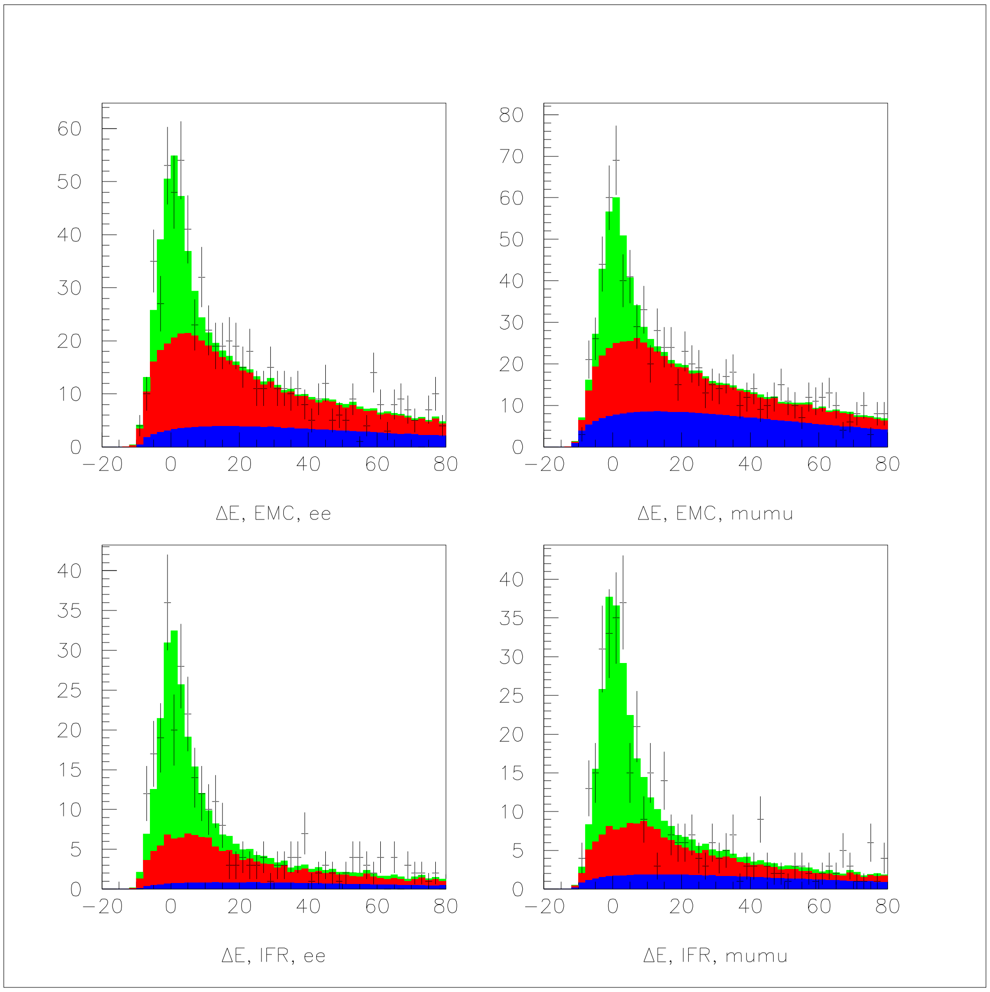

Figure B.20: Fit of the ΔE spectrum for the KaonPion tagged events.

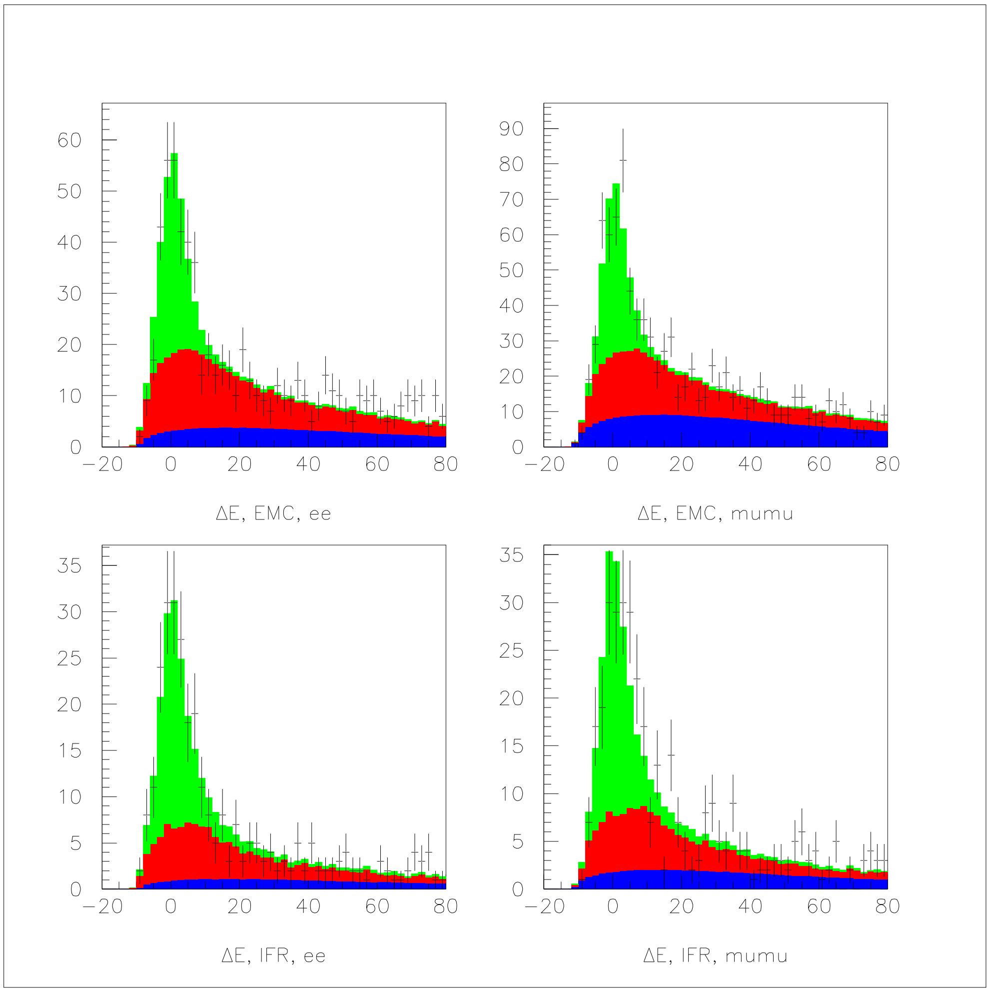

Figure B.21: Fit of the ΔE spectrum for the Pion tagged events.

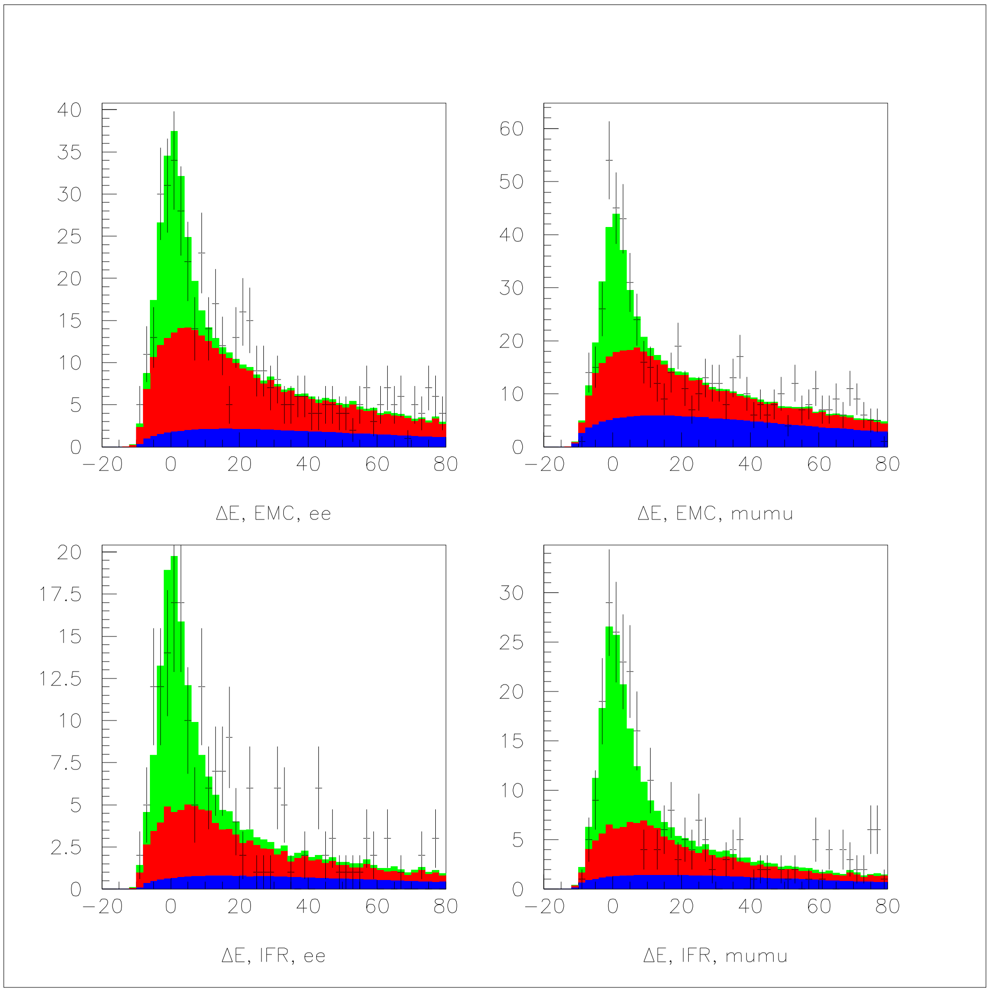

Figure B.22: Fit of the ΔE spectrum for the Other tagged events.

C Comparison of the 2006 and 2008 results

As a cross-check, we compare the fit results obtained in 2006 [10] and 2008. They are shown by run period in Tables C.2 and C.3 for 2006 and 2008, respectively. They are expressed in terms of sin2β and $|\lambda|$ since they were the variables used express CPV in [10]. We switched to S and C in order to better compare our results to the ones of other collaborations, such as Belle [14].

Sample	sin2β+$\lvert\lambda\rvert$ fits 2006	
	sin2β	$\lvert\lambda\rvert$
$J/\psi K_L$	**0.735±0.074**	**1.063±0.063**
Run1+2 Kl-EMC $J/\psi \rightarrow e^+e^-$	1.282 ± 0.410	1.040 ± 0.263
Run1+2 Kl-IFR $J/\psi \rightarrow e^+e^-$	1.194 ± 0.716	1.499 ± 0.640
Run1+2 Kl-EMC $J/\psi \rightarrow \mu^+\mu^-$	0.919 ± 0.251	1.219 ± 0.265
Run1+2 Kl-IFR $J/\psi \rightarrow \mu^+\mu^-$	0.949 ± 0.352	0.852 ± 0.215
Run3+4 Kl-EMC $J/\psi \rightarrow e^+e^-$	0.813 ± 0.244	1.183 ± 0.215
Run3+4 Kl-IFR $J/\psi \rightarrow e^+e^-$	0.391 ± 0.321	1.166 ± 0.250
Run3+4 Kl-EMC $J/\psi \rightarrow \mu^+\mu^-$	0.624 ± 0.216	1.006 ± 0.168
Run3+4 Kl-IFR $J/\psi \rightarrow \mu^+\mu^-$	0.703 ± 0.271	1.176 ± 0.252
Run5 Kl-EMC $J/\psi \rightarrow e^+e^-$	0.797 ± 0.250	1.184 ± 0.211
Run5 Kl-IFR $J/\psi \rightarrow e^+e^-$	0.576 ± 1.612	1.442 ± 0.203
Run5 Kl-EMC $J/\psi \rightarrow \mu^+\mu^-$	0.956 ± 1.478	0.881 ± 0.409
Run5 Kl-IFR $J/\psi \rightarrow \mu^+\mu^-$	0.573 ± 1.612	0.801 ± 0.386
Run1-5 Kl-EMC $J/\psi \rightarrow e^+e^-$	0.896 ± 0.152	1.131 ± 0.133
Run1-5 Kl-IFR $J/\psi \rightarrow e^+e^-$	0.645 ± 0.212	1.438 ± 0.194
Run1-5 Kl-EMC $J/\psi \rightarrow \mu^+\mu^-$	0.810 ± 0.132	0.997 ± 0.107
Run1-5 Kl-IFR $J/\psi \rightarrow \mu^+\mu^-$	0.696 ± 0.169	0.874 ± 0.123

Table C.2: Unblind result of combined fitting for CP asymmetries in the $J/\psi K_L$ CP 2006 data sample (Run 1 through 5) and in various subsamples for sin2β and $|\lambda|$.

Sample	$\sin2\beta$+$\lvert\lambda\rvert$ fits 2008	
	$\sin2\beta$	$\lvert\lambda\rvert$
$J/\psi K_L$	**0.694±0.061**	**1.034±0.051**
Run1+2 Kl-EMC $J/\psi \to e^+e^-$	1.499 ± 0.281	0.828 ± 0.166
Run1+2 Kl-IFR $J/\psi \to e^+e^-$	0.564 ± 0.276	1.266 ± 0.256
Run1+2 Kl-EMC $J/\psi \to \mu^+\mu^-$	0.925 ± 0.214	1.108 ± 0.201
Run1+2 Kl-IFR $J/\psi \to \mu^+\mu^-$	0.927 ± 0.269	0.921 ± 0.178
Run3+4 Kl-EMC $J/\psi \to e^+e^-$	0.781 ± 0.229	1.178 ± 0.200
Run3+4 Kl-IFR $J/\psi \to e^+e^-$	0.632 ± 0.224	1.037 ± 0.177
Run3+4 Kl-EMC $J/\psi \to \mu^+\mu^-$	0.446 ± 0.206	1.016 ± 0.157
Run3+4 Kl-IFR $J/\psi \to \mu^+\mu^-$	0.473 ± 0.245	1.076 ± 0.180
Run5 Kl-EMC $J/\psi \to e^+e^-$	0.675 ± 0.221	1.287 ± 0.217
Run5 Kl-IFR $J/\psi \to e^+e^-$	0.491 ± 0.268	1.031 ± 0.174
Run5 Kl-EMC $J/\psi \to \mu^+\mu^-$	1.000 ± 0.208	0.871 ± 0.143
Run5 Kl-IFR $J/\psi \to \mu^+\mu^-$	0.516 ± 0.218	0.957 ± 0.159
Run1-5 Kl-EMC $J/\psi \to e^+e^-$	0.867 ± 0.136	1.101 ± 0.119
Run1-5 Kl-IFR $J/\psi \to e^+e^-$	0.575 ± 0.150	1.119 ± 0.140
Run1-5 Kl-EMC $J/\psi \to \mu^+\mu^-$	0.759 ± 0.122	0.988 ± 0.097
Run1-5 Kl-IFR $J/\psi \to \mu^+\mu^-$	0.597 ± 0.142	0.922 ± 0.099
Run6 Kl-EMC $J/\psi \to e^+e^-$	0.366 ± 0.331	0.915 ± 0.209
Run6 Kl-IFR $J/\psi \to e^+e^-$	0.707 ± 0.264	1.038 ± 0.212
Run6 Kl-EMC $J/\psi \to \mu^+\mu^-$	0.509 ± 0.297	1.023 ± 0.230
Run6 Kl-IFR $J/\psi \to \mu^+\mu^-$	1.011 ± 0.355	1.500 ± 0.507

Table C.3: Unblind result of combined fitting for CP asymmetries in the $J/\psi K_L$ CP 2008 data sample (Run1 through 6) and in various subsamples for $\sin2\beta$ and $\lvert\lambda\rvert$.

D Systematic errors related to the other Charmonium modes

Here we show the result of the results of the calculation of the systematic errors on the global fit and $J/\psi K^0$ fit configurations, for the systematics specific to $J/\psi K^0_L$. The systematic errors were also calculated for the fit split by mode, but are negligible for all modes except $J/\psi K^0_L$. We also show the summary of the total systematic errors for all configurations.

E Systematic Errors specific to the $J/\psi K^0_L$ mode

E.1 All modes together

Table E.4 shows the results for the global fit configuration (all modes fitted together).

E.2 $J/\psi K^0$ only

Table E.5 shows the results for the K^0 configuration.

F Total Systematic Errors

The summary of systematic uncertainties are shown in Table 5.4.4 for the nominal configuration with all CP modes combined. For the 7-parameter configuration, and for $J/\psi K^0$ ($= K^0_S + K^0_L$), and $J/\psi K^0_S$ ($= \pi^+\pi^- + \pi^0\pi^0$) configurations, the summary

Parameter	Global fit δS	Global fit δC
Sample Composition (ΔE fit)		
Sample Composition	$\pm$ 0.002518	$\pm$ 0.00046
$J/\psi X$ branching fractions		
$B \to J/\psi K^*$	-0.000229, -0.000771	-0.000091,-0.000032
$B^0 \to J/\psi K^0$	$+$ 0.000464, $-$ 0.000961	$-$ 0.000032, $+$ 0.000006
$B \to J/\psi K_L^0 \pi$	$-$ 0.000194, $-$ 0.000142	$-$ 0.000001,$-$ 0.000009
$B^0 \to \chi_c K_L^0$	$-$ 0.000479, $+$ 0.000090	$+$ 0.000138, $-$ 0.000012
$B \to J/\psi X$ other	$+$ 0.001803, $+$ 0.003114	$+$ 0.000295, $+$0.000225
Assumed CP for background		
$B \to J/\psi K^*$	$-$ 0.000477, $+$ 0.000469	$+$ 0.000013, $-$0.000007
$B \to J/\psi X$	$-$ 0.000504, $+$ 0.000491	-0.000001, +0.000012
non-J/ψ BG	$-$ 0.003556, $+$0.003546	$-$ 0.000086, $+$0.000087
Shape of ΔE PDFs		
ΔE smearing	$-$ 0.00211, $+$ 0.001418	$-$0.000049, $+$ 0.000183
ΔE shift	$-$ 0.001432, $+$ 0.002120	$-$0.000580, $+$ 0.000732
MC K_L^0 reweighting	$-$ 0.000152	$+$ 0.000004
Total systematic error	$\pm$ 0.005712	$\pm$ 0.000679
Total statistical error	$\pm$ 0.02844	$\pm$ 0.02184

Table E.4: Results of systematic error evaluation for the global fit.

for S and C are shown in Table F and F.

Parameter	K^0 fit δS	K^0 fit δC
Sample Composition (ΔE fit)		
Sample Composition	$\pm$ 0.002748	$\pm$ 0.000560
$J/\psi X$ branching fractions		
$B \to J/\psi K^*$	$-$ 0.00029, $-$ 0.000836	$-$ 0.000093,+ 0.000007
$B^0 \to J/\psi K^0$	+0.000550, $-$ 0.001081	$-$0.000048, +0.000019
$B \to J/\psi K_L^0 \pi$	$-$ 0.000211, $-$ 0.000283	+ 0.000005,$-$ 0.000155
$B^0 \to \chi_c K_L^0$	$-$ 0.000576, + 0.000126	+ 0.000004, $-$ 0.000016
$B \to J/\psi X$ other	+ 0.001942, + 0.003347	+ 0.000303, + 0.000173
Assumed CP for background		
$B \to J/\psi K^*$	$-$ 0.000555, + 0.000549	+ 0.000015, $-$ 0.000014
$B \to J/\psi X$	$-$ 0.000576, + 0.000581	$-$ 0.000005, + 0.000003
non-J/ψ BG	$-$ 0.004074, + 0.004065	$-$ 0.000107, + 0.000099
Shape of ΔE PDFs		
ΔE smearing	$-$ 0.002294, + 0.001502	$-$ 0.000007, + 0.000181
ΔE shift	$-$ 0.001563, + 0.002284	$-$ 0.000691, + 0.000844
MC K_L^0 reweighting	$-$ 0.000216	$-$ 0.000171
Total systematic error	$\pm$ 0.006345	$\pm$ 0.000788
Total statistical error	$\pm$ 0.03076	$\pm$ 0.02464

Table E.5: Results of systematic error evaluation for the K^0 fit.

Source/sample		Full	$J/\psi\, K^0$	$J/\psi\, K^0_S$	$J/\psi\, K^{*0}$
Mistag differences	S_f	0.0055	0.0055	0.0055	0.0055
	C_f	0.0016	0.0016	0.0016	0.0016
Δt resolution	S_f	0.0067	0.0068	0.0069	0.0259
	C_f	0.0027	0.0029	0.0034	0.0062
$J/\psi\, K^0_L$ background	S_f	0.0057	0.0063	0.0000	0.0002
	C_f	0.0009	0.0009	0.0000	0.0003
CP content	S_f	0.0046	0.0034	0.0036	0.0564
of Background	C_f	0.0029	0.0021	0.0009	0.0256
$m_{\rm ES}$ parameterization	S_f	0.0022	0.0020	0.0026	0.0372
	C_f	0.0004	0.0005	0.0008	0.0080
$\Delta m_d, \tau_B, \Delta\Gamma_d/\Gamma_d$	S_f	0.0030	0.0033	0.0036	0.0140
	C_f	0.0013	0.0012	0.0011	0.0013
Tag-side interference	S_f	0.0014	0.0014	0.0014	0.0014
	C_f	0.0143	0.0143	0.0143	0.0143
Fit bias	S_f	0.0023	0.0044	0.0041	0.0271
(MC statistics)	C_f	0.0026	0.0044	0.0041	0.0389
Total	S_f	0.0124	0.0130	0.0118	0.0870
	C_f	0.0158	0.0175	0.0158	0.0540

Table F.6: Main systematic uncertainties on S_f and C_f for the full CP sample, and for the $J/\psi\, K^0$, $J/\psi\, K^0_S$, and $J/\psi\, K^{*0}(K^{*0} \rightarrow K^0_S\pi^0)$ samples. For each source of systematic uncertainty, the first line gives the error on S_f and the second line the error on C_f. The total systematic error (last row) also includes smaller effects not explicitly mentioned in the table.

Source/sample		$J/\psi K_S^0(\pi^+\pi^-)$	$J/\psi K_S^0(\pi^0\pi^0)$	$\psi(2S)K_S^0$	$\chi_{c1}K_S^0$	$\eta_c K_S^0$
Mistag	S_f	0.0055	0.0055	0.0055	0.0055	0.0055
differences	C_f	0.0016	0.0016	0.0016	0.0016	0.0016
Δt resolution	S_f	0.0072	0.0074	0.0072	0.0099	0.0163
	C_f	0.0030	0.0043	0.0070	0.0039	0.0036
$J/\psi K_L^0$	S_f	0.0002	0.0002	0.0004	0.0002	0.0002
	C_f	0.0003	0.0001	0.0001	0.0005	0.0001
Background and	S_f	0.0032	0.0073	0.0156	0.0174	0.0506
CP content	C_f	0.0012	0.0034	0.0056	0.0098	0.0187
m_{ES}	S_f	0.0021	0.0089	0.0238	0.0061	0.0023
parameterization	C_f	0.0007	0.0063	0.0008	0.0017	0.0005
$\Delta m_d, \tau_B, \Delta\Gamma_d/\Gamma_d$	S_f	0.0031	0.0073	0.0157	0.0025	0.0158
	C_f	0.0014	0.0013	0.0010	0.0009	0.0020
Tag-side	S_f	0.0014	0.0014	0.0014	0.0014	0.0014
interference	C_f	0.0143	0.0143	0.0143	0.0143	0.0143
Fit bias	S_f	0.0048	0.0040	0.0079	0.0072	0.0073
(MC statistics)	C_f	0.0042	0.0030	0.0019	0.0042	0.0070
Total	S_f	0.0118	0.0172	0.0359	0.0396	0.0566
	C_f	0.0156	0.0182	0.0203	0.0249	0.0288

Table F.7: Main systematic uncertainties on S_f and C_f for the $J/\psi K_S^0(\pi^+\pi^-)$, $J/\psi K_S^0(\pi^0\pi^0)$, $\psi(2S)K_S^0$, $\chi_{c1}K_S^0$ and $\eta_c K_S^0$ decay modes ($J/\psi K_L^0$ were already discussed in the main text). For each source of systematic uncertainty, the first line gives the error on S_f and the second line the error on C_f. The total systematic error (last row) also includes smaller effects not explicitly mentioned in the table.

Bibliography

[1] J. H. Christenson *et al.*, Phys. Rev. Lett. **13**, 138 (1964).

[2] A. D. Sakharov , Pisma Zh. Eksp. Teor. Fiz. **5**, 32 (1967) [Sov. Phys. JETP Lett. **5**, 24 (1967)].

[3] M. Kobayashi and T. Maskawa, Prog. Th. Phys. **49**, 652 (1973).

[4] N. Cabibbo, Phys. Rev. Lett. **10**, 531 (1963).

[5] Fermilab E288 Collaboration, S. W. Herb *et al.*, Phys. Rev. Lett. **39**, 252 (1977); W. R. Innes *et al.*, Phys. Rev. Lett. **39**, 1240 (1977).

[6] CDF Collaboration, F. Abe *et al.*, Phys. Rev. D **50**, 2966 (1994); **51**, 4623 (1994); **52**, 2605 (1995); Phys. Rev. Lett. **73**, 225 (1994);**74**, 2626 (1995); D0 Collaboration, S. Abachi *et al.*, Phys. Rev. Lett. **72**, 2138 (1994); **74**, 2422 (1995); **74**, 2632 (1995); Phys. Rev. D **52**, 4877 (1995).

[7] *BABAR* Collaboration, B. Aubert *et al.*, Phys. Rev. Lett. **86**, 2515 (2001).

[8] Belle Collaboration, A. Abashian *et al.*, Phys. Rev. Lett. **86**, 2509 (2001).

[9] *BABAR* Collaboration, B. Aubert *et al.*, Phys. Rev. Lett. **86**, 091801 (2001); Belle Collaboration, K. Abe *et al.*, Phys. Rev. Lett. **87**, 091802 (2001).

[10] *BABAR* Collaboration, B. Aubert *et al.*, Phys. Rev. Lett. **99**, 171803 (2007).

[11] 33^{rd} International Conference on High Energy Physics 2006 (ICHEP 2006), **hep-ex/0607107**; 34^{th} International Conference on High Energy Physics 2008 (ICHEP 2008), **arXiv:0808.1903[hep-ex]**.

[12] **arXiv:0902.1708v1[hep-ex]**.

[13] A. Carter, A. Sanda, Phys. Rev. Lett. **45**, 952 (1980); A. Carter, A. Sanda, Phys. Rev. D **23**, 1567 (1981); I. I. Bigi. A. Sanda, Nucl. Phys. B **193**, 85 (1981).

[14] C. Amsler *et al.*, (Particle Data Group), Phys. Lett. B **667**, 1 (2008).

[15] G. Lüders, Math. Phys. Medd. Kgl. Danske Akad.**28**, 5 (1954); W.Pauli, in Niels Bohr and the Development of Physics, ed. W. Pauli, Mc Fraw-Hill (1955); J. S. Bell, Proc. Roy. Soc. A **231**, 479 (1955).

[16] M. Gell-Mann and A. Pais, Phys. Rev. **97**, 1387 (1955).

[17] A. Einstein, B. Podolsky and N. Rosen, Phys. Rev. **47**, 777 (1935).

[18] S. L. Glashow, Nucl. Phys. **22**, 579 (1961); A. Salam, Proc. 8th NOBEL Symposium, p. 367 (N. Svartholm, Ed., Stockholm 1968); S. Weinberg, Phys. Rev. Lett. **19**, 1264 (1967).

[19] P. Higgs, Phys. Rev. Lett. **13**, 508 (1964).

[20] lhc.web.cern.ch/lhc

[21] C. Jarlskog, Phys. Rev. Lett. **55**, 1039 (1985).

[22] L. Wolfenstein, Phys. Rev. Lett. **51**, 1945 (1983).

[23] CKMFitter Group (J. Charles *et al.*), Eur. Phys. J. **C41**,1-131 (2005), [hep-ph/0406184], updated results and plots available at: http://ckmfitter.in2p3.fr

[24] P.J. Oddone, Proceedings of UCLA Workshop: Linear Collider $B\bar{B}$ Factory Conceptual Design, 1987, p. 243.

[25] *BABAR* Collaboration, B. Aubert *et al.*, Nucl. Instrum. Methods A **479**, 1 (2002).

[26] V. Re *et al.*, IEEE Trans. Nucl. Sci.**49**, 3284 (2002).

[27] S. Curry *et al.*, Nucl. Instrum. and Methods A **583**, 162 (2007).

[28] W. T. Meyer and R. L. McKay, *BABAR* Note 365.

[29] P. Stanley, J. Anderson, M. Kraimer, EPICS Record Reference Manual, smallhttp://www.aps.anl.gov/epics/EpicsDocumentation/AppDevManuals/RecordRef/Recordref-1.html.

[30] C. Hearty, "Measurement of the Number of $\Upsilon(4S)$ Mesons Produced in Run 1 (B Counting)", *BABAR* Analysis Document 134; http://www.slac.stanford.edu/BFROOT/www/Physics/Analysis/AWG/Luminosity/lumiScriptHelp.html.

[31] A. Ryd *et al.*, "EvtGen - A Monte Carlo Generator for B-Physics", *BABAR* Analysis Document **522**.

[32] T. Sjostrand, Comput. Phys. Commun. **82**, 74 (1994).

[33] GEANT4 Collaboration, S. Agostinelli *et al.*, Nucl. Instrum. and Methods A **506**, 250 (2003).

[34] P. Billoir, Nucl. Instrum. and Methods A **225**, 225 (1984).

[35] T. Brandt, "Likelihood Based Electron Identification", *BABAR* Analysis Document **396**.

[36] S. Mclachlin (For the *BABAR* PID group), "PID Control Samples at *BABAR*", *BABAR* Analysis Document **1056**.

[37] *BABAR* PID Group,

http://www.slac.stanford.edu/BFROOT/www/Physics/Tools/Pid/pid.html

[38] *BABAR* Collaboraton, B. Aubert *et al.*, Phys. Rev. D **66**, 032003 (2002).

[39] `http://www.slac.stanford.edu/~perl/HepRApp`.

[40] D. Lange, "Study of K_L^0 identification efficiency using the EMC", *BABAR* Analysis Document **59**.

[41] ARGUS Collaboration, H. Albrecht *et al.*, Z. Phys. **C48**, 543 (1990).

[42] W. Verkerke and D. Kirkby, "The Roofit toolkit for data modeling", physics/0306116.

[43] W.-M. Yao *et al.*, (Particle Data Group), J. Phys. **G33**, 1 (2006).

[44] B. Aubert *et al.*, (*BABAR* Collaboration), Phys. Rev. D **76**, 031102(R) (2007).

[45] A. Roodman,

`http://www-conf.slac.stanford.edu/phystat2003/talks/roodman/`

`roodman-blind-stat2003.pdf`,

Talk given at PHYSTAT2003 (2003).

[46] F. James, "Minuit, Function Minimization and Error Analysis", CERN long writeup D506.

[47] O. Long, M. Baak, R. N. Cahn, and D. Kirkby, Phys. Rev. D **68**, 034010 (2003).

[48] K. F. Chen, *et al.*, (Belle Collaboration), Phys. Rev. Lett. **98**, 031802 (2007).

[49] M. Ciuchini *et al.*, Z. Phys. C **68**, 239 (1995).

[50] http://www.slac.stanford.edu/xorg/hfag,

E. Barberio *et al.*, arXiv:0808.1297.

[51] CKMfitter Group (L. Charles *et al.*), Eur. Phys. J.**C41**, 1-131 (2005) [hep-ph/0406184], updates results and plots available at:

http://ckmfitter.in2p3.fr.

[52] M. Z. Wang *et al.* (Belle Collaboration), Observation of $B^0 \to p\bar{\Lambda}\pi^-$, Phys. Rev. Lett. **90**, 201802 (2003).

[53] M. Z. Wang *et al.* (Belle Collaboration), Study of the baryon-antibaryon low-mass enhancements in charmless three-body baryonic B decays, Phys. Lett. B **617**, 141-149 (2005).

[54] B. Aubert *et al.*(*BABAR* Collaboration), Phys. Rev. D **72**, 051101 (2005).

[55] W. S. Hou and A. Soni, Pathways to Rare Baryonic B Decays, Phys. Rev. Lett. **86**, 4247 (2001).

[56] C. K. Chua and W. S. Hou, Three-body baryonic $\bar{B} \to \Lambda\bar{p}\pi$ decays and such, Eur. Phys. J. C **29**, 27-35 (2003).

[57] G. Hanson *et al.*, Phys. Rev. Lett. **35**, 1609 (1975).

[58] M. R. Teague, Journal of the Optical Society of America, **70**, 920 (1979).

[59] R. A. Fisher, The Use of Multiple Measurements in Taxonomic Problems, Annals of Eugenics, 7 Part II: 179-188 (1936).

[60] F. R. Le Diberder and M. Pivk, Nucl. Instrum. Methods A**555**,356 (2005).

[61] 33^{rd} International Conference on High Energy Physics 2006 (ICHEP 2006), **arXiv:hep-ex/0608020v1**.